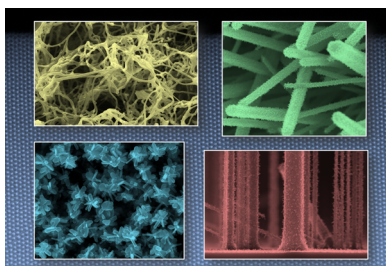


One-Dimensional Titanium Dioxide Nanomaterials: Nanowires, Nanorods, and Nanobelts

 Xudong Wang,* Zhaodong Li, Jian Shi,[†] and Yanhao Yu

Department of Materials Science and Engineering, University of Wisconsin—Madison, Madison, Wisconsin 53706, United States



CONTENTS

1. Introduction	A
2. Crystal Structure of TiO ₂	B
3. Growth Mechanisms of 1D TiO ₂ Nanostructure	C
3.1. Vapor–Liquid–Solid Mechanism	C
3.2. Oriented Attachment (Surfactants Free)	D
3.3. Surfactant-Controlled Growth	D
3.4. Surface Reaction-Limited Growth	E
4. Synthesis of 1D TiO ₂ Nanomaterials	G
4.1. Solution-Based Synthetic Approaches	G
4.1.1. Hydrothermal/Solvothermal Methods	G
4.1.2. Sol–Gel Methods	H
4.1.3. Surfactant-Assisted Methods	I
4.1.4. Microwave Assisted Methods	J
4.1.5. Sonochemical Synthesis	K
4.1.6. High Temperature Pyrolysis	K
4.1.7. Electrospinning Methods	L
4.2. Vapor-Based Approaches	M
4.2.1. Chemical/Physical Vapor Deposition	M
4.2.2. Atomic Layer Deposition-Related Methods	N
4.2.3. Pulsed Laser Deposition	O
4.3. Templated Growth	O
4.3.1. Sol–Gel Template Methods	P
4.3.2. Suspended Molecular Template Methods	P
4.3.3. Electrochemical Deposition Methods	P
4.4. Top-down Fabrication Techniques	Q
4.4.1. Direct Oxidation of Titanium Sheets	Q
4.4.2. Electrochemical Etching Methods	Q
4.4.3. Photoelectrochemical Etching methods	R
5. Properties and Applications of 1D TiO ₂ Nanomaterials	R
5.1. Electronic Property and Photocatalytic Applications of 1D TiO ₂ Nanomaterials	R
5.1.1. Size-Related Electronic Property of TiO ₂ NWs	R
5.1.2. Foreign Element Doped TiO ₂ NWs	S
5.1.3. TiO ₂ NW Heterostructures	V
5.2. 1D TiO ₂ Nanostructures in Photovoltaics	X

5.2.1. Dye-Sensitized Solar Cells	X
5.2.2. Polymer-Based Solar Cells	AB
5.2.3. Quantum Dot Solar Cells	AC
5.3. 1D TiO ₂ Nanostructures for Energy Storage	AD
5.3.1. Lithium Ion Batteries	AD
5.3.2. Supercapacitors	AE
5.4. Electrochromism and Electrochromic Devices	AE
5.5. Solid State Sensors	AE
5.6. Mechanical Properties	AF
6. Conclusion	AF
Author Information	AG
Corresponding Author	AG
Present Address	AG
Notes	AG
Biographies	AG
Acknowledgments	AH
References	AH

1. INTRODUCTION

Titanium dioxide (TiO₂) is a widely used multifunctional ceramic material due to its excellent stability and physical-chemical properties as well as its great accessibility and moderate cost. Its commercial products can be commonly found in pigments, paints, coatings, and sunscreens.^{1–4} Led by the pioneering discovery of the photocatalytic water splitting phenomenon on a TiO₂ electrode in early 1970s,⁵ TiO₂ quickly attracted numerous research interests for its catalytic and energy-related applications. The appropriate electronic band structure and excellent surface activity endowed TiO₂ with very promising potentials in hydrogen production, photovoltaic, photocatalysts, lithium-ion batteries, fuel cells, gas sensors, detoxification, and supercapacitors.^{6–16} For example, dye-sensitized, polymer-based, and quantum dot (QD) solar cells have all been built on TiO₂-based electrodes, which offered the most stable performance and the highest efficiency compared to those of other oxide materials.^{13,17–20} TiO₂-based nanoparticles (NPs) recently demonstrated the highest efficiency of photocatalyzed water splitting by narrowing its bandgap to enable visible light photoactivities.²¹ The structure, processing, property, and application of TiO₂-related materials have been covered in a number of excellent reviews and articles.^{22–28} Nevertheless, although TiO₂ possessed such promising potentials, its relatively poor charge transport property and wide bandgap (~3.2 eV) are two main limitations for its

Special Issue: 2014 Titanium Dioxide Nanomaterials

Received: November 3, 2013

contemporary applications in catalysis and energy harvesting/storage.

In fact, most TiO₂ applications were based on its nanoscale morphologies, particularly the NP forms. In the nanometer scale, due to the appearance of the quantum confinement effects, the electron and hole transport behaviors could be changed, and the electronic band structure could be shifted.²⁹ The extremely large surface-to-volume ratio of nanomaterials can significantly increase the surface reaction sites and might even modulate the catalytic activity of the surface atoms.³⁰ Certain high energy surfaces may also become stable in the nanoscale structures and improve their catalytic properties.⁶ Therefore, further improvement on the performance of TiO₂-based devices and systems may heavily rely on the development of appropriate nanostructures with well-engineered composition, geometry, crystallography, and integration. The synthesis, properties, and applications of TiO₂ nanomaterials were recently covered in a comprehensive review article.³¹

1D-nanostructures, such as nanowires (NWs), are an important member in the nanomaterial family. They share certain common characteristics with NPs and 2D nanosheets or thin films, such as large surface area and quantum confinement effects. However, geometrically they offer unique properties that are difficult to achieve using the other two categories, e.g., 1D confined transport of electrons or photons and excellent mechanical properties. For example, single-crystalline NW electrodes were introduced to batteries,³² solar cells,³³ and photoelectrochemical cells³⁴ for effective charge separation and collection. Quantum confinement in semiconductor NWs by tuning the characteristic dimension allows the realization of photonic and optoelectronic devices that differ dramatically from conventional thin film-based ones.³⁵ High flexibility and excellent fatigue resistance make NWs advantageous building blocks for nanogenerators that scavenge mechanical energies from ambient environment.^{36–38} In addition, the capability of integrating NWs in large area with controlled pattern created a new path toward NW-based flexible electronic and optoelectronic systems that might eventually realize roll-to-roll mass production.³⁹ For the same reasons, TiO₂ NW structures are also promising for achieving performance gain in their energy and environmental application areas.

Based on the geometry, 1D nanostructures typically consist of four categories: NW, nanorod (NR), nanobelt (NB), and nanotube.⁴⁰ The first three categories all possess a solid structure; while the nanotube has a hollow center. Due to the significantly different geometry, property, and synthesis strategies between the nanotube and other geometries, this review article only covers the 1D nanostructures in the first three categories, i.e., NW, NR, and NB. In general, NRs are NWs with a small aspect ratio (i.e., short NWs), which typically appear rigid and straight. NB is a special NW structure with a rectangular cross-section. Typical NB structures are single crystals with well-defined side crystal facets. Sometime, nanofibers were also used to describe the NW morphology, particularly when the NWs are very long and not single-crystalline. In this article, the crystal structure of TiO₂ will be summarized first. Then the growth mechanisms were reviewed with an emphasis on the oriented attachment and surface-reaction-limited growth, which are unique for 1D growth of TiO₂ crystals. Section 4 provides a comprehensive review of representative synthetic methods for making TiO₂ 1D nanomaterials, covering solution-based, vapor-based, template-based, and top-down four different strategies. The 1D morphology-

associated properties and application explorations are discussed at last.

2. CRYSTAL STRUCTURE OF TiO₂

TiO₂ naturally exhibits four different types of polymorphs, i.e., rutile, anatase, brookite, and TiO₂(B).⁴¹ In addition, several metastable polymorphs, such as TiO₂ (H), TiO₂ II, and perovskite, have been produced synthetically. Different phases have different properties and thus require different conditions to form desired morphologies and offer different performance. Generally, rutile is the most stable phase, while the anatase, brookite, and TiO₂ (B) are metastable and will transform into rutile under high temperature. This phase stability relationship also exists in TiO₂ nanomaterial formations. Anatase phased nanomaterials were commonly obtained but always found in solution-based or low-temperature vapor deposition systems. High temperature deposition or annealing would usually yield rutile TiO₂ nanostructures. Brookite and TiO₂ (B) phases were less common and typically obtained from solution-based growth systems. Other metastable phases have to be synthesized using particular types of precursors and under restrict conditions. They were very rarely observed as a stable nanomaterial phase, and thus will not be covered in this article.

Figure 1 shows the schematic crystal structure of the four common TiO₂ phases using Ti–O octahedrons as the

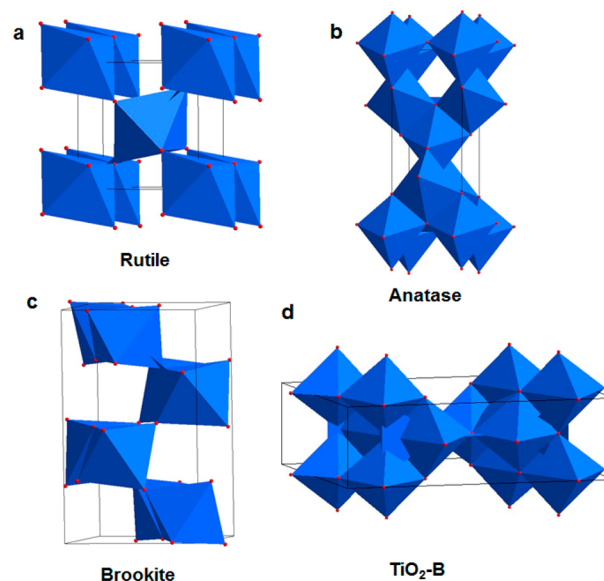


Figure 1. Schematic unit cell structure of four TiO₂ polymorphs. (a) Rutile. (b) Anatase. (c) Brookite. (d) TiO₂ (B).

fundamental building block. These four phases have different symmetry and their nanostructures always exhibit different growth behaviors and preferred morphologies. Rutile TiO₂ has a tetragonal structure with $a = 0.459$ nm and $c = 0.296$ nm (Figure 1a).⁴² {011} and {100} are the two surface families with the lowest energy and thus the thermodynamically equilibrium morphology of rutile TiO₂ is a trunked octahedron. This is also the mostly observed morphology from synthetic rutile TiO₂ powders. The anatase phase is tetragonal as well but has a significantly longer c -axis (0.951 nm) compared to the a -axis (0.379 nm; Figure 1b).⁴² Anatase TiO₂ also has the same lowest energy surfaces as rutile and prefers trunked octahedron morphology in its nanostructures. Brookite is orthorhombic

and has a large unit cell consisting of 8 TiO₂ groups (Figure 1c). TiO₂(B) also has a large unit cell with a more open crystal structure compared to other polymorphs (Figure 1d). It is monoclinic with a particularly long *a*-axis (1.216 nm).⁴³ However, both brookite and TiO₂(B) phases are much less often observed in synthetic TiO₂ nanostructures.

Understanding the crystal structure is the first step toward rational experimental design for synthesizing TiO₂ NWs with defined phase, shape, dimension, and crystallinity, which is of fundamental importance for achieving desired functionality and performance. Owing to the advanced electron microscopy techniques, researchers are now able to directly observe the atomic structures of different TiO₂ phases and understand the surface and interface properties. For example, Gong et al. used scanning tunneling microscopy (STM) on the (101) surface of anatase TiO₂ and acquired atomic-resolution image of the surface step-edge configurations.⁴⁴ Based on this observation, first principle calculation was performed to determine the step-edge formation energies and water absorption energies. Shibata et al. directly observed the atomic structure of reduced rutile TiO₂ (110) surfaces using high-voltage electron microscopy (HVEM), aberration-corrected high-angle annular dark-field (HAADF), and scanning transmission electron microscopy (STEM).⁴⁵ From the atomic-resolution images, they evidenced the (110) surface restructuring process, i.e. that is, upon the removal of oxygen, surface Ti atoms move to the interstitial sites that are on top of the Ti–O columns. The HAADF imaging in STEM now becomes a popular and powerful tool in obtaining atomic-level understandings of TiO₂ crystal structures and growth mechanisms.^{46,47} Recently, it has been showed by De Caro et al. that regular high resolution TEM is also able to achieve subangstrom resolution of TiO₂ lattices with the assistance of electron diffractive imaging.⁴⁸ This technique works for relatively low doses of electrons and may be an alternative approach to imaging the atomic structure of less-stable phases. In general, with these advanced imaging techniques, one can expect more clear and in-depth understandings of the growth mechanisms and the structure–property relationships of TiO₂ nanostructures and beyond.

3. GROWTH MECHANISMS OF 1D TiO₂ NANOSTRUCTURE

In order to achieve 1D morphologies, such as NWs and NRs, it is essential to obtain one rapid growth direction during the evolution of nanocrystals. For certain crystals, this requirement is naturally satisfied due to the strong anisotropic property of their crystal structures. For example, wurtzite ZnO crystals naturally have selective rapid growth along the [0001] direction, and thus NW is one of the preferred morphologies during self-assembly growth. However, for some other crystals, such as TiO₂, such anisotropy is less obvious, and they usually require additional kinetics to realize the 1D morphologies. Typical approaches include applying catalysts to induce a rapid precipitation interface, introducing dislocations (screw, twin, etc.) to accelerate the growth rate along the dislocation propagation direction, surface functionalization to exaggerating the deposition difference among different crystal facets, and increasing the building block concentrations to accentuate the assembly rate differences along different crystal facets. Details of these strategies for nanocrystal morphology control are well documented in previous review articles.^{49–52} Some of these approaches have been successfully applied to the growth of TiO₂ 1D

nanostructures.^{53–57} The growth generally follows the mechanisms that have been understood from other oxide materials. For example, catalyst-involved growth typically follows a vapor–liquid–solid (VLS) process. The surfactant-controlled growth is mostly implemented in liquid (aqueous and nonaqueous) systems.^{49–52} To our best knowledge, so far either explicit solution–liquid–solid (SLS) or dislocation-driven growth mechanism has not been reported on TiO₂ NWs growth. VLS and surfactant-controlled growth mechanisms have been well-documented in many articles, and we will briefly discuss them in this review.^{58–68} Meanwhile, our discussion will highlight another two 1D growth mechanisms, the oriented attachment (with the absence of surfactants)⁶⁹ and surface-reaction-limited growth,⁷⁰ which were found playing an important role in the growth of TiO₂ 1D nanostructures in solution and vapor systems, respectively.

3.1. Vapor–Liquid–Solid Mechanism

The VLS mechanism describes the growth of NWs as a result of solid precipitation from supersaturated catalyst alloy droplets. Vapor-phased precursors are usually directly absorbed by the liquid catalysts during the growth. TiO₂ NWs can be grown via the VLS mechanism using a variety of metal catalysts. Ha et al. reported that single-crystalline rutile TiO₂ NWs were synthesized on Ti foil substrates (served as Ti source as well) patterned with catalytic Sn nanoislands.⁵³ NWs grew along the (110) direction having a rectangular cross section and faceted with the (001) and (110) planes. After the growth, Sn residue was identified by the electron back scattering diffraction (EBSD) on the tip of the TiO₂ NWs, confirming the catalytic role of Sn droplet during the growth. Lee et al. claimed that Au was also an effective catalyst to guide the growth of high-quality rutile TiO₂ NWs on sapphire and silicon substrates.⁵⁴ Ti buffer layer and oxygen gas were used as the precursors. However, no explicit evidence was found to illustrate the catalyst–NW interface and the role of Au. Kim et al. reported the use of Ni as the VLS catalyst for TiO₂ NWs growth.⁷¹ They found that single-crystal TiO₂ NWs could be obtained when the growth temperature was well below the bulk Ni melting point after they intentionally introduced a small amount of phosphorus. Their analysis showed that a liquid Ni/P eutectic shell surrounding the solid Ni core was responsible for the catalytic effect. High-resolution electron energy loss spectroscopy (EELS) revealed that the active catalyst Ni/P shell has 3–8% phosphorus. Growth of NWs was implemented by the absorption of precursors onto the Ni/P eutectic liquid layer followed by the precipitation of solid TiO₂. Figure 2 shows a STEM image of Ni/TiO₂ interface with inset as the model of the droplet during VLS growth.

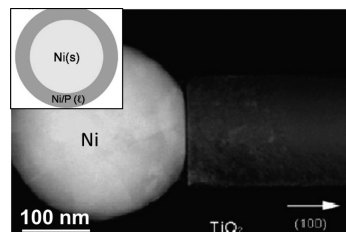


Figure 2. Scanning transmission electron microscopy image of Ni/TiO₂ interface. Inset is the model of the droplet during VLS growth. Reprinted with permission from ref 71. Copyright 2010, the American Chemical Society.

3.2. Oriented Attachment (Surfactants Free)

Traditionally, Ostwald ripening was proposed to be a major mechanism for the growth of large crystals from massive small particles in TiO₂ nutrient solution. Penn et al. revealed that the formation of some 1D TiO₂ nanostructures in solution followed the oriented attachment mechanism.⁶⁹ Oriented attachment is the organization of TiO₂ nanocrystals based on their crystallographic orientations and registration of these nanocrystals into a single crystalline 1D nanostructure. The driving force of an oriented attachment growth is the reduction of the surface energy contributed by the removal of certain crystal facets with a high surface energy. Predicted by density function theory (DFT) calculation by Barnard et al., a thermodynamically stable anatase (as it is the most observed early stage phase in hydrothermal growth) TiO₂ is shown in Figure 3, where the {101} facets are the dominant side facets

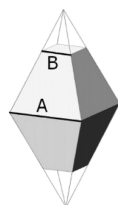


Figure 3. Anatase tetragonal {101} bipyramid truncated by (001) and (00 $\bar{1}$) facets. Reprinted with permission from ref 72. Copyright 2005, the American Chemical Society.

and the top and bottom facets are (001) and (00 $\bar{1}$), respectively.⁷² Such a structural configuration is consistent with what has been observed by Penn et al. and Shi et al. through transmission electron microscopy (TEM).^{73,74} According to DFT calculation, surface free energy of the (001) surface of anatase TiO₂ is 0.51 J/m²; 0.39 J/m² for the (100) surface and 0.35 J/m² for the (101) surface. Penn et al. proposed that in the nucleation stage, after the number of TiO₂ nanocrystals reaches a critical value, instead of coarsening via the Ostwald ripening process, TiO₂ nanocrystals diffuse, coalesce by joining together through the (001) facets and form a chain-like 1D necklace structure, as shown in Figure 4a.⁷⁵ It was often shown that the kinked region with a negative curvature was formed by the attachment of nanocrystals (Figure 4b). They can be easily

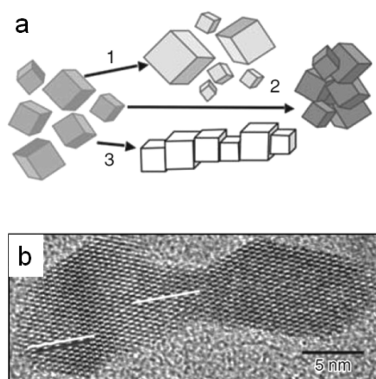


Figure 4. (a) Schematic model illustrating the oriented aggregation mechanism which is different from the Ostwald ripening and unidirectional aggregation. (b) TEM image of a crystal dimer formed by oriented attachment mechanism. Reprinted with permission from ref 78. Copyright 2010, Cambridge University Press.

filled during the growth stage directly from molecular TiO₂ deposition in the nutrient solution due to the large surface free energy gain. Therefore, such a necklace-like structure may not be observable to evidence the oriented attachment mechanism after a long growth time.

Varieties of models were proposed to elucidate and quantify the oriented attachment growth. Penn conceived a simple molecular dimer formation model to quantify the process, in which the primary crystals were treated as molecules and only allowed the formation of dimers.⁷⁶ A dimer in such case indicates an oriented aggregate composed of two primary TiO₂ crystals. They revealed a rate law for oriented attachment shown as

$$\frac{d[P - P]}{dt} = k[P]^2 \quad (1)$$

where k is a rate constant and P–P symbolizes two oriented attached particles. P–P dimerization requires the orientation rotation of individual particles and removal of the intermediate solvent substances. According to this model, the rate of oriented attachment process was second order-related to the concentration of primary particles, which was found to be relatively consistent with the Derjaguin–Landau–Verwey–Overbeek (DLVO) theory when the electrostatic repulsive and van der Waals attractive forces are considered. A drawback of this model was that it only predicted the presence of oriented aggregates with two primary particles. To solve this problem, Ribeiro et al. developed a stepwise polymerization kinetic model to explain the growth of chain-like TiO₂ architecture, where primary particles were regarded as monomer and oriented aggregates as multimer.⁷⁷ From this model, the kinetics of the oriented attachment growth was found directly dependent on the solution viscosity and temperature. It exhibited a good agreement with experimental observations. A good review of the oriented attachment kinetics quantification can be found in ref 78.

3.3. Surfactant-Controlled Growth

With the assistance of surfactants, controllable hydrolysis of metal alkoxides and correspondingly modified methods are popular ways for achieving anisotropic growth of TiO₂ nanostructures. By using facet-selective surfactants, morphology of the final structure of target materials can be manipulated. Since the growth rate of a certain crystal facet is an exponential function of its surface energy, anisotropic growth could be achieved and controlled by modifying the surface energy of desired facets by selective surfactant coverage. Jun et al. used lauric acid (LA) as the specific surfactant and trioctylphosphine oxide (TOPO) as the nonselective surfactant in the growth of TiO₂ NRs.⁷⁹ With a fixed amount of TOPO but increasing the amount of LA, longer TiO₂ NRs were obtained. Structural analysis showed that increased LA concentration led to NW elongation along the (001) direction and an escalation of relative (004)/(200) intensities. They concluded that at high LA concentrations, LA selectively bonded to the TiO₂ {001} facets through a bridge-bonding mode, which slowed down the growth rate along the (001) direction. Once the growth rate along the [001] direction reached ~ 2.7 times of that along the [101] direction, according to crystallographic symmetry, the TiO₂ {001} facets would preserve. Afterward, under certain kinetic perturbations, a step started to form after the (101) facet reached a critical value, resulting in the evolution of a necklace morphology. Figure 5 shows different morphologies in

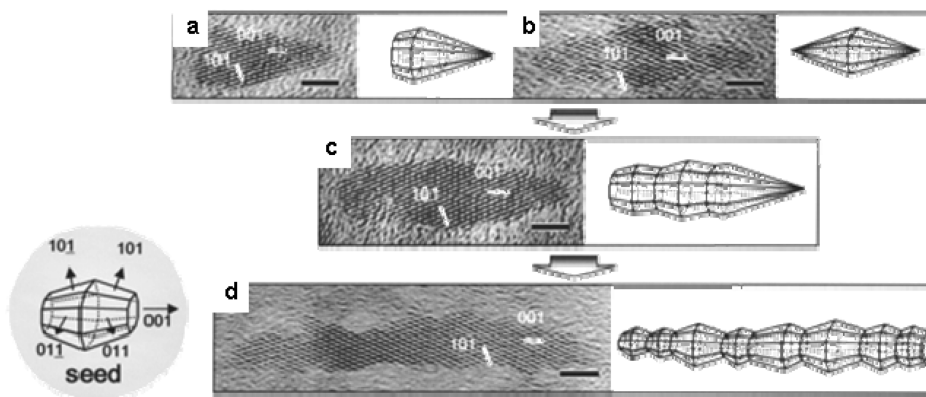


Figure 5. HRTEM images and schematic models of (a) a TiO₂ bullet, (b) a diamond, (c) a short rod, and (d) a long rod. Scale bars are 3 nm. Reprinted with permission from ref 79. Copyright 2003, the American Chemical Society.

correlation to the surfactant concentration, in which Figure 5d illustrates the case of long NRs growth. Li et al. found that LA served as both a hydrolysis reagent to react with Ti(OBu)₄ and a coordination surfactant to direct the anisotropic growth of TiO₂ NRs.⁸⁰ The LA reagent and cyclohexane solvent could slow down the reaction, condensation and nucleation rates, which were found to be the key parameters to achieve the anisotropic growth.

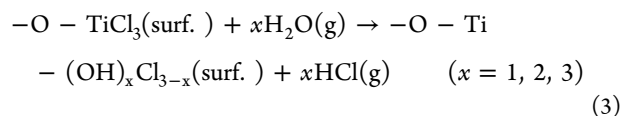
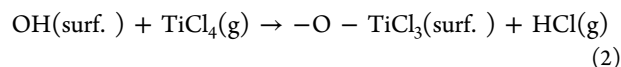
In addition, Cozzoli et al. demonstrated the growth of anatase TiO₂ NRs by hydrolysis of titanium tetraisopropoxide (TTIP) using oleic acid (OLEA) as the surfactant.⁸¹ It was argued that the unidirectional growth of TiO₂ NRs was a consequence of three factors: the TiO₂ precursor is titanium oxocarboxyalkoxide which owns certain anisotropic reactivity; the OLEA serves as absorbing-chelating ligand suppressing the growth of crystal along certain crystallographic orientations; proper control of hydrolysis by adjusting water supply. In addition, Zhang et al. reported a nonhydrolytic synthetic approach for the formation of length controllable TiO₂ NRs.⁸² It was claimed that the modified (001) face of anatase TiO₂ is easily aminolyzed under the attack of oleylamine, which is responsible for the formation of Ti–O–Ti network along the <001> direction. Joo et al. applied a nonhydrolytic sol–gel reaction between TTIP and OLEA (as surfactant) at 270 °C for the synthesis of anatase TiO₂ NRs, where cosurfactant 1-hexadecylamine was revealed to be able to control the diameter of the NRs.⁸³

3.4. Surface Reaction-Limited Growth

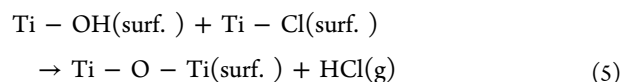
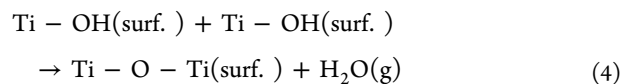
Many approaches have been explored to synthesize NWs from the vapor phase without using any foreign catalysts via the VS process. It offers a high lattice purity that is beneficial in many realms, such as eliminating unintentional doping and avoiding the poisonous effect of transition metals. However, the growth mechanisms are less defined compared to metal-catalyzed VLS NW growth. Typically, dislocation driven and excess metal adatoms self-catalyzing were used to explain certain 1D growth phenomena in VS processes. Recently, Shi et al. discovered a new 1D growth mechanism of 1D TiO₂ NRs, which was controlled by surface chemical reactions. It was named as surface reaction-limited pulsed chemical vapor deposition (SPCVD).⁷⁰ The growth was modified from an atomic layer deposition (ALD) process, where pulsed TiCl₄ and H₂O precursors were introduced into the growth chamber and separated by inert gas purging (the growth and structure details are reviewed in section 4). The application of high temperature

(600 °C) condition in the SPCVD process distinguishes this growth method from other general ALD thin film growth.

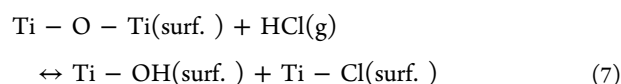
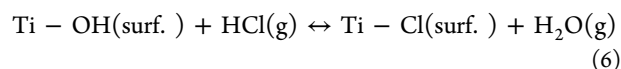
The elongated purging time (60 s) and highly confined submicrometer-sized spaces were critical for the morphology change from polycrystalline ALD thin films to NR arrays. This is the key to understanding the evolution of 1D nanostructures. The surface restructuring and surface (or gas phase) diffusion mechanisms that were responsible for the surface roughness of ALD films were adapted to explain the evolution of NR morphology in a SPCVD process. Ideally, TiCl₄ and H₂O are anchored onto the growing surface by reactions:



Meanwhile, the surface –OH and –Cl groups can also react with each other forming surface bridging groups:



Reactions 4 and 5 are responsible for the reduced growth rate in ALD. Furthermore, HCl byproducts also could make important contributions to the growth, particularly at high temperature, if they are not quickly removed from the growing surfaces:



Reactions 6 and 7 are the reversed reactions of 3 and 5, respectively. Thus, reaction 6 is a backward reaction and would reduce the growth rate; while reaction 7 could reactivate the bridging groups and facilitate the growth. Different combination of reactions 2–7, together with the diffusion of HCl byproduct, could induce different growth rate along different

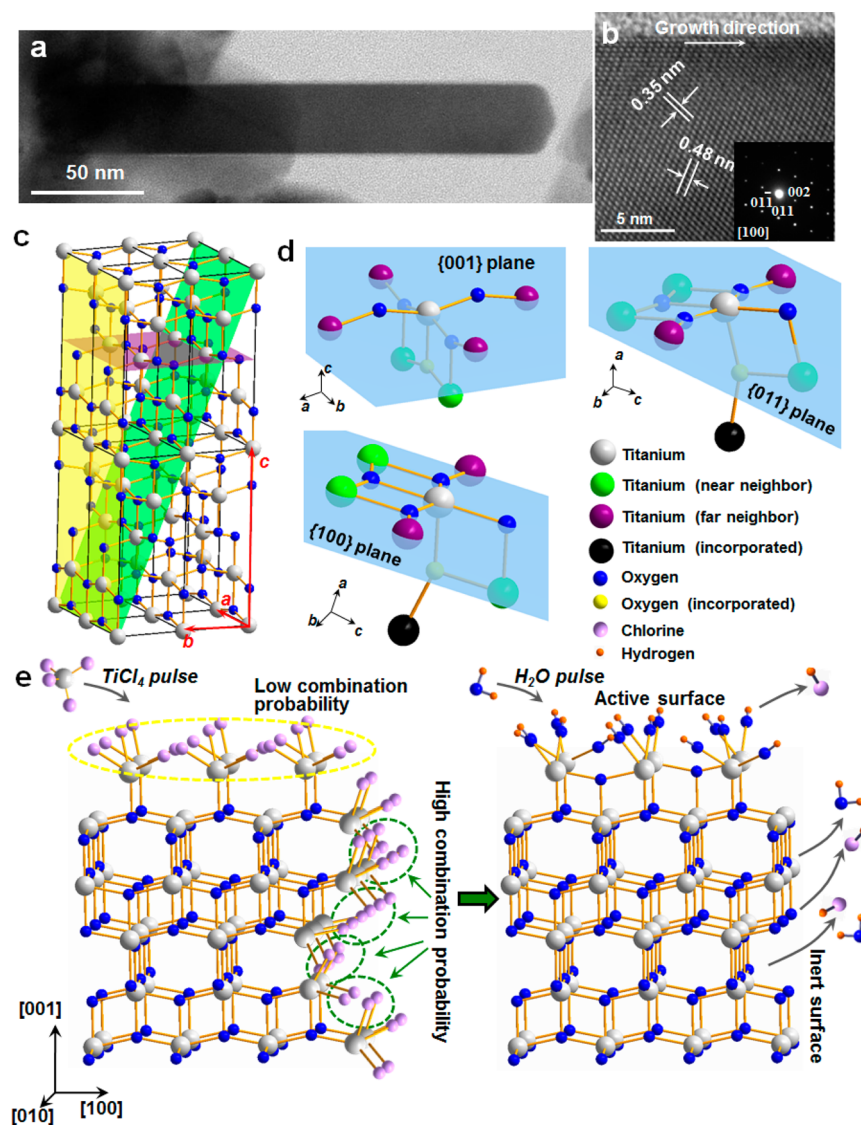


Figure 6. Understanding the surface-reaction-limited growth mechanism from anatase TiO_2 NRs. (a) A TEM image of an anatase TiO_2 NR. (b) High resolution TEM image showing the perfect lattice and facets orientation of the TiO_2 NR, inset is the corresponding SAED. (c) Crystal structure model of a $2 \times 2 \times 2$ supercell of anatase TiO_2 . (d) Ball-and-stick model of the $\{001\}$, $\{011\}$, and $\{100\}$ cleavage surfaces centered with a randomly selected Ti atom (gray). (e) Schematic illustration of one ideal pulsed CVD growth cycle. Reprinted with permission from ref 70. Copyright 2011, the American Chemical Society.

crystal surfaces, and thus faceted anisotropic growth might be possible.

TEM revealed that the NRs were single crystals and grown along the combination of the $[002]$ and $[011]$ directions and the $\{011\}$ and $\{100\}$ planes were the side surfaces (Figure 6a,b). Figure 6c shows the crystal structure of anatase TiO_2 represented by a $2 \times 2 \times 2$ supercell, where the $\{001\}$, $\{011\}$, and $\{100\}$ facets are highlighted in purple, green, and yellow, respectively. Cleavage surfaces along these planes are shown in Figure 6d, where three types of neighboring Ti atoms can be classified: (1) incorporated Ti atom (black); (2) far-neighbor (purple) which is a Ti atom that is 3.78 \AA away from the center Ti atom; (3) near-neighbor (green) which is a Ti atom that is 3.04 \AA away from the center Ti atom. Based on this crystal structure, two possible mechanisms were suggested – surface recombination [reactions 4 and 5] and HCl restructuring [reactions 6 and 7]. Due to the larger Ti–Ti distance on the (001) surface, larger strain is likely possessed by the Ti–O–Ti

bridges, which make this “inert” bridge more reactive to HCl, thus reactivate the growing surface [reaction 7]. These two mechanisms do not conflict with each other and may take effect simultaneously. For example, combination of reactions 5 and 7 could cause the active groups to move on crystal surfaces and reach more stable sites where recombination rate is low. Therefore, TiO_2 NRs were grown by rapid surface chemical reaction on the active (001) planes but growth-limited to an equal degree on the inert $\{100\}$ and $\{011\}$ facets. Figure 6e schematically illustrates the growth fronts at the (001) and (100) surfaces in such an ideal process proposed above. Overall, it was believed that it was the high temperature condition which makes such self-termination or recombination reactions on side walls and propagation of $\{001\}$ facet growth possible, as it helped to slow the surface reaction rate of TiCl_4 with H_2O in an ALD chamber. This growth mechanism may potentially allow creation of uniform 1D nanostructures inside

highly confined spaces from the rich material pool of ALD deposition.

4. SYNTHESIS OF 1D TiO₂ NANOMATERIALS

Numerous routes have been explored to the synthesis of 1D TiO₂ nanostructures from both bottom up and top down. Representative bottom-up approaches include a large variety of solution- and vapor-based growth strategies.^{54,84,85} Although bottom-up approaches remains as the major synthesis efforts, several top-down procedures have also been explored for 1D TiO₂ growth, such as direct oxidation and electrochemical etching techniques.^{86–89} A comprehensive overview of the synthetic methods is presented in this section.

4.1. Solution-Based Synthetic Approaches

Solution-based growth techniques offer several major advantages for mass production of nanomaterials including low-cost, simple processing, and good scalability.^{90–94} Many advanced nanomaterial systems that are currently commercially available are made via solution-based approaches, including colloidal NPs and QDs. Solution-based syntheses were also the most widely used approaches for growing TiO₂ nanostructures over decades. Recent years, with better understandings of the growth kinetics in the solution systems, TiO₂ NWs were obtained with good 1D morphology and single crystallinity. Nevertheless, morphology and physical property control and optimization still remain as the main challenges for applications of the 1D TiO₂ nanostructures directly from solution. In this subsection, typical solution-based synthesis approaches and the representative products are reviewed in details. Some other methods, where the liquid phase is not preserved during the formation of 1D TiO₂ nanostructures, such as pyrolysis and electrospinning, are also covered, because the TiO₂ precursor solution is the critical component for receiving desired morphology and composition.

4.1.1. Hydrothermal/Solvothermal Methods. The hydrothermal/solvothermal method is widely used for manufacturing small particles in the ceramics industry using aqueous or nonaqueous solutions, respectively.³¹ The synthesis is typically implemented in autoclaves at elevated temperature and pressure. Under such conditions, a supercritical fluid is formed, which can significantly increase the solubility of most solid precursors and allows the precipitation of nanostructures from a wide range of inorganic materials. Due to the simple setup, facile operations, and desirable growth results, many researchers used this method to produce 1D TiO₂ nanostructures. Initial work was mostly for TiO₂ nanotube growth.^{95–97} More recently, these approaches were adapted to the growth of solid 1D TiO₂ nanostructures, e.g., NRs and NWs.

Huang et al. developed a convenient hydrothermal method to synthesize rutile TiO₂ NRs by employing TiCl₃/HCl solution and ethanol.⁹⁸ The growth was conducted at 180 °C for 18 h. It was found that the concentrations of HCl and ethanol were key factors for controlling the structure of TiO₂. An appropriate amount of H⁺ and ethanol could lead to the formation of TiO₂ NRs rather than nanoparticles; while higher acidity and ethanol content would result in assembly of NRs into microflowers. Melcarne et al. applied a nonaqueous, solvothermal method to the synthesis of anatase TiO₂ NRs using Ti(IV)-isopropoxide as the Ti precursor. The solvent was benzyl alcohol and additional acetic acid was added to the reactant for morphology control.⁹⁹ The rod-like anatase TiO₂ nanostructures were possibly a result of the attachment of

acetic acid to certain crystal facets, where the deposition rates were limited. The formation of anatase phase was attributed to the lower acidity environment and lower pressure due to the higher boiling point of benzyl alcohol compared to the growth conditions of rutile TiO₂ NRs.

Hydro/solvothermal approaches are able to adapt a large variety of Ti-precursors for TiO₂ growth because of its high-pressure and high-temperature conditions. For example, through the same approach, Ti(OC₃H₇)₄, TiCl₄, and C₆H₂₂N₂O₈Ti were used by different research groups and successfully received 1D TiO₂ nanostructures.^{100–102} Besides, Eu(NO₃)₃ was also introduced to create Eu-doped TiO₂ NWs.¹⁰³ Hydrothermal approach typically yields a large amount of 1D TiO₂ nanostructures from solution. When no substrates or seeding layer were applied, the as-received TiO₂ NWs were random and existed in a powder form. Well-aligned TiO₂ NW arrays can be created by using TiO₂ NP-seeded substrates in a hydrothermal system.^{9,104,105} The seed layer could be prepared by spin coating the TiO₂ polymeric sol on the substrate followed by 450 °C annealing for 1 h. In a typical synthesis, titanium(IV) butoxide in HCl solution was used as the precursor. The hydrothermal growth was conducted at 170 °C for 6 h. The products were washed and annealed at 450 °C in air. This process yielded well-aligned single-crystalline rutile TiO₂ NRs with a good size uniformity (Figure 7a).¹⁰⁵

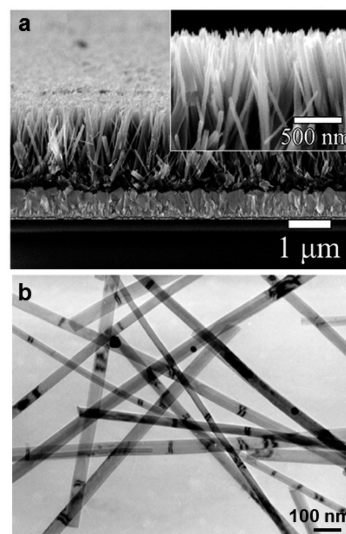


Figure 7. One dimensional TiO₂ nanostructure synthesized through hydro/solvothermal method. (a) Cross sectional view of a TiO₂ NRs array on FTO substrates. Reprinted with permission from ref 105. Copyright 2011, American Chemical Society. (b) TEM image of bamboo-shaped Ag-doped TiO₂ NWs. Reprinted with permission from ref 112. Copyright 2005, the American Chemical Society.

Solvent is another important aspect in hydro/solvothermal growth since it controls the state of active Ti species during the growth. In addition to conventional one-solvent system (aqueous or organic), cosolvent systems were implemented to achieve more controllable crystal growth or arrangement. Kajari et al. investigated the influence of cosolvent to the morphology of 1D TiO₂ nanostructures.¹⁰⁶ In a growth system containing anatase TiO₂ powders and caustic soda solution at the pH of 12.77, three types of solvent (water, water + ethanol, and water + ethylene glycol) were used. After heating the mixture in an autoclave for 16 h at 150 °C, TiO₂ NRs, ultralong

NWs, and nanotubes were obtained from the three different solvents, respectively. During the hydrothermal process, sodium titanate ($\text{Na}_2\text{Ti}_3\text{O}_7$) nanosheets were found to be an important intermediate phase that would eventually transform into TiO_2 nanostructures. The polarity and coordinating ability of the cosolvent systems could affect the solubility, reactivity and diffusion behavior of the reactants and intermediate phases, and thus control the TiO_2 morphology. For example, when a high-alkaline water–ethanol solvent was applied, ultralong NWs were formed instead of NRs due to the high concentration and rapid decomposition of the $\text{Na}_2\text{Ti}_3\text{O}_7$ nanosheets. Nanotube morphology was formed in the water–ethylene glycol solvent as a result of stacking and rolling of the $\text{Na}_2\text{Ti}_3\text{O}_7$ nanosheets due to Na^+ deficiency and the chelating property of ethylene glycol.¹⁰⁶ This method has been followed by many researchers for producing 1D TiO_2 nanostructures.^{107–111}

In addition to a simple NW structure, hydro/solvothermal methods are able to provide various nanomorphologies. Figure 7b shows bamboo-shaped Ag-doped TiO_2 NWs which were synthesized by a simple solvothermal method using a solution of titanium butoxide [$\text{Ti}(\text{OC}_4\text{H}_9)_4$] in ethanol as the precursor and AgNO_3 as the doping reagent.¹¹² The junctions (dark contrast region in the NW) were believed to be the locations where the Ag elements were concentrated in the anatase TiO_2 crystal lattice. TiO_2 NW/NB arrays could also be created by hydrothermally oxidizing the Ti substrate in aqueous alkali followed by post annealing.¹¹³ In this process, $\text{Na}_2\text{Ti}_5\text{O}_{11}$ NBs first grew through the reaction of Ti plate with NaOH aqueous solution. When the $\text{Na}_2\text{Ti}_5\text{O}_{11}$ NBs were long enough, the dislocation-induced strain could convert the NBs into a multilayer NW structure. After replacing Na^+ with H^+ by HCl treatment, the final TiO_2 NWs arrays were obtained by annealing. This is a simple and large-scale process, which does not need any seeds, TiO_2 powder, templates, or stabilizers to achieve the 1D growth and orientation alignment. This structure has been successfully applied to multifunctional NW bioscaffolds.³⁶ Feng et al. further developed densely packed single crystal TiO_2 NW arrays up to 5 μm long on FTO substrates via a low temperature nonpolar solvent/hydrophilic substrate interface hydrolysis reaction.¹¹⁴

Branch-type 1D nanostructures of mono- and two-phase anatase/rutile TiO_2 were also created by hydrothermal processes. Oh et al. and Wang et al. presented such structures by applying presynthesized TiO_2 NWs as the seeds for secondary TiO_2 branch growth.^{115,116} Through a typical hydrothermal process using TTIP as the precursor, Oh et al. directly grew rutile TiO_2 NR branches on rutile NW surfaces, forming a homogeneous branched structure (Figure 8a). The key for growing such homogeneously branched structures is to initiate the nucleation on NW surfaces, which typically requires higher driving force than continuous growth of the initial NW seeds. It might be because the surfaces of the initial NW seeds were terminated with foreign molecules, which raised the energy for continuous lattice growth, and thus secondary nucleation became energetically favorable. TEM characterization showed that both the core NWs and branch NRs were grown along the [001] direction. The typical branch diameter and length are ~ 20 and ~ 150 nm, respectively.¹¹⁵ Anatase TiO_2 NWs were also used as the core material to support rutile TiO_2 NR branch growth via a water–dichloromethane interface-assisted hydrothermal process using highly reactive TiCl_4 as the precursor.¹¹⁶ Figure 8b shows the rutile–anatase heterogeneously branched TiO_2 NW structures synthesized by Wang et

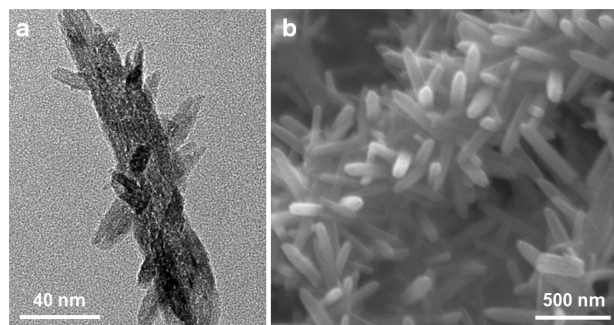


Figure 8. Morphologies of branched TiO_2 . (a) A TEM image showing rutile branches grown on rutile TiO_2 NWs. Reprinted with permission from refb 115. Copyright 2009, the American Chemical Society. (b) An SEM image of rutile NWs grown on anatase TiO_2 NWs. Reprinted with permission from ref 116. Copyright 2011, Elsevier.

al. In the water–dichloromethane system, the water reacts with TiCl_4 precursor and initiates the nucleation of TiO_2 both on the TiO_2 NWs surface and at the water–dichloromethane interface. As the temperature rising up, water-in-dichloromethane emulsions were formed at the water–dichloromethane interface and stabilized by forming TiO_2 NPs inside via TiCl_4 hydrolysis.¹¹⁷ The emulsion-encapsulated TiO_2 NPs would collide and adherence to the TiO_2 NWs and act as the nuclei for growing rutile branches in the subsequent growth stage.

TiO_2 -based heteronanostructures have been developed from a wide range of materials and morphology combinations, such as TiO_2 nanobranches on CuO NWs,¹¹⁸ TiO_2 NRs on Si NWs,^{47,74,119,120} and Si/ TiO_2 core–shell NWs.¹²¹ Most of them were synthesized via similar hydrothermal processes following a stepwise nucleation and growth sequence.¹²² This type of heterostructure has the potential to integrate the different physical and/or chemical properties from the core and shell materials. For example, the TiO_2 branches could act as highly active photocatalysts, while the core NW could serve as low-loss charge conductors when they are applied in photoelectrochemical (PEC) or photovoltaic devices. Another type of functional heterostructure is to decorate TiO_2 NRs/NWs with plasmonic or magnetic nanocrystals. The decorating nanocrystals include Fe_xO_y , Co, and Ag, which are typically synthesized via a solution-based colloidal nucleation process on TiO_2 backbones.^{123–126} These nanocrystals could introduce additional size-related optical, electrical, or magnetic properties to engineer the regular functions of the TiO_2 NWs. In general, developing TiO_2 NW-based heterostructures is a promising strategy for improving the performance of TiO_2 -based devices to the level possibly beyond what pure-phased TiO_2 nanomaterials can ever reach. Specific application examples will be discussed in details in section 5.

4.1.2. Sol–Gel Methods. Sol–gel methods are widely used in synthesizing inorganic or organic–inorganic hybrid materials.¹²⁷ In a sol–gel process, the sol is a colloidal suspension that is typically prepared by mixing the precursors (e.g., metal organic compounds or inorganic metal salts) with water. When stirring the sol for hydrolysis and polymerization reactions, loss of solvent converts the liquid sol into a three-dimensional network called a gel. The gel has a continuous solid skeleton surrounded by a continuous liquid phase.¹²⁸ The wet gel is further converted into solid nanostructures after heat treatment under proper conditions. Sol–gel methods are particularly useful for synthesizing oxide ceramic nanomaterials, because the sol brings together necessary precursor elements in their

liquid states and then converts into nanostructure with desired composition via gel solidification. This approach effectively circumvents the poor ionic diffusivity in most oxide ceramic materials that restricts the formation of desired composition and morphology.

The sol–gel method has a long history of being applied for TiO₂ NP manufacturing from hydrolyzing titanium precursors.^{129–132} As for TiO₂ 1D nanomaterials, the process typically requires particular guidance or confinement in order to achieve 1D anisotropic growth. For example, TiO₂ nanofibers were synthesized via a sol–gel process using titanium(IV) isopropoxide (TTIP) and acetic acid. These precursors yielded a hexanuclear titanium acetate complex, Ti₆O₆(OAc)₆(OⁱPr)₆, which could be converted into 1D macromolecules upon condensation. Removing the organic groups from the macromolecules chains at high temperature produced polycrystalline TiO₂ nanofibers (Figure 9a).¹³³ Reverse micelle system could

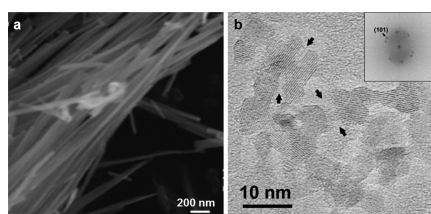


Figure 9. One dimensional TiO₂ nanostructures grown by sol–gel methods. (a) Straight and long TiO₂ nanofibers synthesized by a sol–gel method after 380 °C calcination. Reprinted with permission from ref 133. Copyright 2006, the American Chemical Society. (b) TEM image of TiO₂ NRs formed by oriented attachment mechanism. Reprinted with permission from ref 135. Copyright 2004, American Chemical Society.

also provide necessary confinement for the formation of TiO₂ 1D nanostructures. It has been successfully integrated into low temperature sol–gel systems for the fabrication of TiO₂ NR arrays. The sizes of TiO₂ NRs were defined by the micelle and were typically small (~40 nm in height) but uniform.¹³⁴

Through a sol–gel process, TiO₂ NPs can be aligned following their crystal orientations and form NWs. This is known as the “oriented attachment” mechanism (will be discussed in details in the next section). In a typical example, Adachi et al. used an aqueous solution of laurylamine hydrochloride (LAHC), tetraisopropylorthotitanate (TIPT) and acetylacetone (ACA) as the sol, which was then converted into a gel suspension after heat treatment at 353 K for 8 h. During this process, TiO₂ NPs condensed and attached with each other forming a NW network structure with identically oriented anatase TiO₂ crystals (Figure 9b).¹³⁵ Other morphologies, such as short and straight TiO₂ NRs, can also be synthesized via this mechanism.¹⁰⁰

4.1.3. Surfactant-Assisted Methods. As discussed in section 3.3, the involvement of surfactant is also a common strategy to realize 1D growth of nanomaterials, where the surfactants act as capping reagents that chemically or physically adhere to special crystal facets and control their relative growth rates.^{79,136–140} This mechanism has been successfully applied to 1D TiO₂ synthesis by several groups.^{49,79–81,83}

High aspect ratio anatase TiO₂ NRs were obtained by Cozzoli et al. through hydrolysis of TTIP in the presence of OLEA surfactant at low temperatures (80–100 °C).⁸¹ The fast hydrolysis process was carried out by injecting the aqueous base

solution rapidly into OLEA/TTIP mixtures (typical molar ratio ranging from 15:1 to 130:1). Tertiary amines or quaternary ammonium hydroxides were added as catalysts for polycondensation in order to ensure a crystalline product. It was observed that there was no precipitate (either amorphous or crystalline) at $T < 80$ °C even after long reaction times. The hydrolysis of TTIP was activated leading to gelification of the mixture only when the temperature was higher than 80 °C (up to 100 °C). The as-synthesized TiO₂ NRs exhibited ~40 nm in length and 3–4 nm in diameter with the elongated crystalline domain aligning with the *c*-axis direction (Figure 10). Initially,

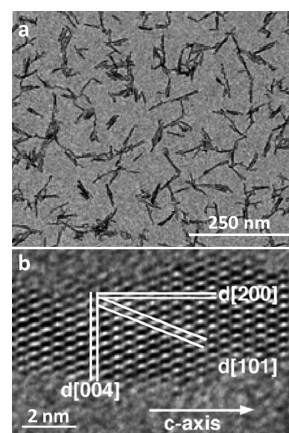


Figure 10. TEM images of TiO₂ NRs prepared by the fast hydrolysis method with surfactant assistance. (a) Low magnification overview. (b) High magnification image of a single NR showing the growth direction is along the *c*-axis. Reprinted with permission from ref 81. Copyright 2003, the American Chemical Society.

titanium oxocarboxylalkoxide was formed from the reaction between TTIP and OLEA. It was a Ti–O framework composed of hexacoordinated Ti atoms and protected by a hydrocarbon periphery. This large Ti-containing molecule was considered as the “monomer” for constructing the TiO₂ crystals. At a relatively high temperature (>80 °C), the carboxylic chains (–OR, where R = –CH(CH₃)₂) are hydrolyzed into –OX (X = R or H) and become active for assembly. Therefore, polycondensation of the hydrolyzed monomers occurs on the –OX group-rich surfaces, and lead the growth of TiO₂ NRs along the [001] direction.^{81,137,141}

Buonsanti et al. synthesized brookite TiO₂ NRs using high-temperature aminolysis of titanium carboxylate complexes (Figure 11a).¹⁴² The reaction solution was a mixture of TiCl₄, OLEA, oleyl amine (OLAM), and 1-octadecene (ODE), which was slowly heated to 290 °C and kept for 30 min. NRs with various sizes were obtained after the subsequent addition of different amounts of an equimolar TiCl₄/OLAM mixture. A larger amount of the mixture yielded thicker (~10 nm) and longer (~200 nm) NRs. It was found that anatase seeds were precipitated first during the nucleation stage and followed by heterogeneous nucleation of brookite on their surfaces. The nucleation phase change was possibly attributed to the size-dependent structural stability of titania polymorphs at the nanoscale.^{142–147} The brookite crystals continuously grew into NRs with continuous TiCl₄/OLAC feeding.

Using the same precursors and surfactants, Joo et al. synthesized similar-sized TiO₂ NRs (3.4 nm × 38 nm) but with a pure anatase phase (Figure 11b).⁸³ The NRs were grown at 270 °C from the nonhydrolytic sol–gel reaction. The size

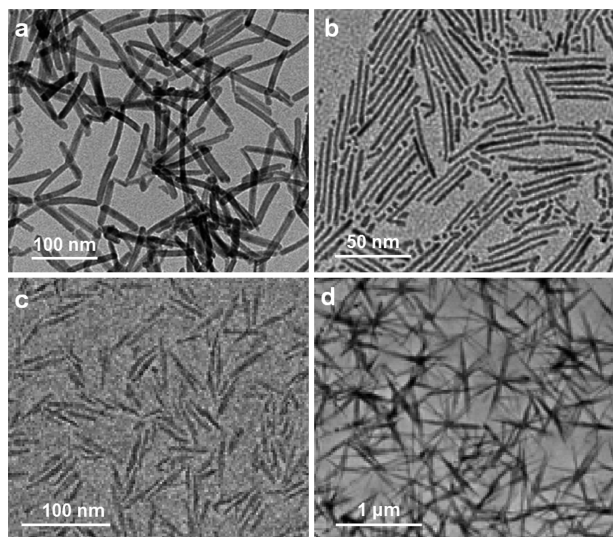


Figure 11. TiO₂ NRs synthesized with oleic acid as surfactant through different procedures. (a) Brookite NRs. Reprinted with permission from ref 142. Copyright 2008, the American Chemical Society. (b) Anatase NRs. Reprinted with permission from ref 83. Copyright 2005, the American Chemical Society. (c) Anatase NRs. (d) Star-shaped rutile NRs. Reprinted with permission from ref 148. Copyright 2006, the American Chemical Society.

could be controlled by introducing 1-hexadecylamine as a cosurfactant. The more 1-hexadecylamine was added to the reaction mixture, the thinner and longer NRs were produced. The phase and size control of the TiO₂ NRs from this nonhydrolytic sol–gel reaction was further investigated by Koo et al. using TiCl₄, titanium(IV) isopropoxide, 1-octadecene, oleic acid, and Oleylamine as reaction chemicals.¹⁴⁸ The two Ti precursors were delivered to the reaction system separately and TiO₂ was formed via the reaction between them: TiCl₄ + Ti(OR)₄ → 2TiO₂ + 4RCl. At an injection rate of 30 mL/h for both precursors, small anatase TiO₂ NRs were received with an average size of 6 nm × 50 nm (Figure 11c). When both injection rates were reduced to 1.25 mL/h, the products changed to 25 nm × 450 nm star-shaped rutile NRs (Figure 11d). The injection rate–morphology relationship is consistent with those observed in nanoparticle systems.¹⁴⁹ Rapid precursor injection gives short nucleation and growth time; while slow injection extends the nucleation period, and thus larger nanostructures and even secondary nucleation (leading to branched structure) could be received. It was also found that the TiO₂ phases were related to the size of the NRs. The critical diameter of the TiO₂ NRs was found to be ~15 nm for the phase to transform from anatase to rutile.^{143,148} The size-dependent phase conversion was possibly a result of the surface free energy that determines the most stable crystal structure under given dimension regimes.^{148,150,151} Similar branched morphology has also been obtained and reported by several other researchers.^{79,115,116,152}

The critical role of precursor injection rate in phase and morphology control has been observed in many other TiO₂ nanomaterial synthesis processes. Based on the same system for brookite NRs synthesis, as described above, Buonsanti et al. obtained hyperbranched anatase TiO₂ nanostructures simply by increased the injection rate of TiCl₄/OLAC from 0.1 mL/min to 0.2 mL/min (Figure 12a).¹⁵² The large amount of precursor and surfactant could possibly suppress the heterogeneous

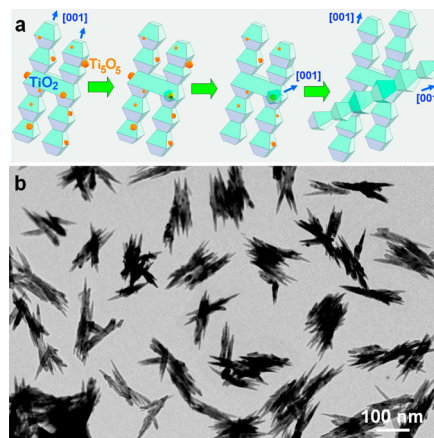


Figure 12. (a) Schematic illustration of a possible mechanism for the secondary branching and arm growth. (b) TEM image of hyperbranched anatase TiO₂ nanostructures via nonaqueous surfactant-assisted synthesis. Reprinted with permission from ref 152. Copyright 2011, the American Chemical Society.

nucleation of brookite phase on the anatase seeds and result in the condensation of Ti-containing monomers into zigzag nanoribbons. Starting from this structure, the first generation-branched nanocrystals (*I*-BNC) were formed as a result of primary growth along the *c*-axis and branching either along the *a*- or *b*-axis or along the equivalent transversal [101] and [011] directions.^{31,152} As schematically shown in Figure 12b, the surface of the *I*-BNCs was decorated with Ti₅O₅ domains, which act as the secondary heterogeneous branching seeds and lead the growth of the second generation-BNC.

4.1.4. Microwave Assisted Methods. The involvement of microwave in synthetic chemistry provides an alternative way for heating, which is considered to be simultaneous, selective, and volumetric with rapid heating rates.^{153–155} Therefore, “microwave flash heating” can dramatically reduce the reaction time for synthesizing organic and inorganic materials mainly by kinetics control.^{156–158} The microwave irradiation provides a unique progressive heating pattern, which is particularly effective for synthesizing colloidal nanomaterials.^{159–161} Microwaves also play an important role in nanomaterial shape control. Because the microwave energy stimulates molecular dipolar polarization and ionic motion, rapid precursor dissolution and quicker reaction kinetics are induced, leading to high fluxes of nuclei with a large concentration gradient. In addition, the microwave-induced dipole moment in primary nuclei building blocks facilitates interparticle collision and anisotropic attachment along the polar direction. This is a desired feature for TiO₂ 1D nanomaterial growth.^{162–167}

Microwave heating was mostly integrated with hydrothermal processes to synthesize TiO₂ NRs, where simple precursors and solvent systems can be applied.^{98,154,168} For example, Jia et al. reported the synthesis of mesoporous anatase TiO₂ NRs through a microwave-assisted method. The large TiO₂ NRs were assembled by small necklace-shaped NRs, which were assembled by spherical particles following the oriented attachment mechanism (Figure 13a).¹⁵⁴ The TiO₂ nanocrystal building blocks were formed by direct hydrolysis of TiCl₄ in diluted hydrochloric acid at room temperature. When the temperature increased, the TiO₂ nanocrystals became more energetic and tend to aggregate into large particles to lower the overall energy of the system. The formation of a necklace-shaped NR would be favorable to minimize the high energy

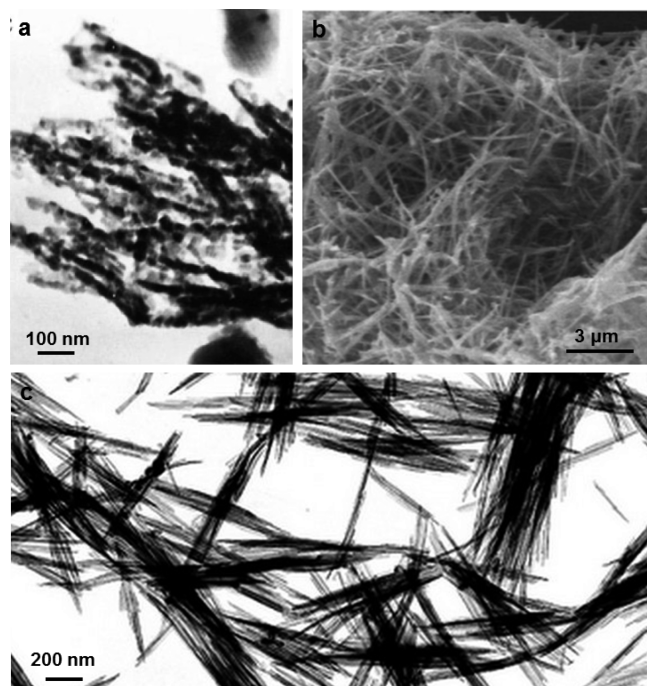


Figure 13. Microwave-assisted synthesis of TiO₂ NRs. (a) TiO₂ NRs assembled by small pearl-necklace-shaped NRs following the oriented attachment mechanism. Reprinted with permission from ref 154. Copyright 2007, Institute of Physics Science. (b) SEM image of TiO₂ NWs bundles synthesized by the microwave-assisted hydrothermal method. Reprinted with permission from ref 171. Copyright 2009, Institute of Physics Science. (c) TEM image of TiO₂ whiskers from sonochemical method. Reprinted with permission from ref 174. Copyright 2001, The Royal Society of Chemistry.

{001} surfaces,⁷⁵ and thus the TiO₂ NR grew along the [001] direction. Long necklace-shaped NRs would further perform a side by side assemble forming thicker NRs.

Lin et al. used a TiCl₄ and water system to synthesize TiO₂ NRs by microwave heating.¹⁶⁹ The reaction solution was prepared by slowly adding deionized (DI) water into TiCl₄ at low temperature (~ 4 °C) to prevent vigorous reactions and precipitation. Chloroform was introduced into the solution, which was then heated in a microwave system at 130 °C for 30 min. TiO₂ NRs were collected from the interface between water and chloroform. The as-synthesized polycrystalline TiO₂ NRs were rutile and bundled into a flower-like morphology with individual mean dimensions of 25 nm in diameter and 150 nm in length. Ma et al. also reported the synthesis of high-quality rutile TiO₂ NRs using a similar microwave-assisted hydrothermal method.¹⁶⁵ Chung et al. synthesized anatase TiO₂ NWs using TiO₂ NPs (ST01, 100% anatase) via the microwave-assisted hydrothermal method.¹⁷⁰ This result suggested that the precursor anatase phase could be retained, although the rutile phase was typically received when a soluble precursor (e.g., TiCl₃) was used.¹⁶⁵ Similarly, by treating a mixture of TiO₂ nanopowder and NaOH inside a microwave oven at 210 °C and 350 W for 5 h, Chang et al. obtained anatase TiO₂ NWs with fairly small and uniform diameters, as shown in Figure 13b.¹⁷¹

By comparing the reaction conditions and results, the temperature appeared to be the most important parameter that controlled the morphology, whereas the lengths of NWs were related to the reaction time.¹⁷⁰ In comparison with conventional hydrothermal processes that typically require

more than 10 h for the formation of NW structure, microwave heating can provide a rapid rise of thermal energy in the liquid reaction system, resulting in homogeneous nucleation and significantly accelerated growth rates. Therefore, microwave heating is highly efficient in terms of energy consumption and reaction time and is considered as an economic approach for nanomaterial manufacturing in large quantities.^{170,171} However, the rapid reaction rate also introduces more difficulties in morphology control.

4.1.5. Sonochemical Synthesis. Acoustic cavitation is a phenomenon that sonic or ultrasound waves generate bubbles in liquid. Interaction among those bubbles could create localized ultrahigh temperature ~5000 K, ultrahigh pressure approximately up to 1000 atm, and very fast heating and cooling rates more than 10¹⁰ K s⁻¹.^{172,173} Application of such high energy “shock waves” to a chemical system is known as sonochemistry. This method has also been successfully applied to synthesizing TiO₂ 1D nanostructures.^{174–177} A typical process simply used TiO₂ powders in a NaOH aqueous solution. TiO₂ 1D nanostructure would be received after sonicating the solution for a certain period of time by an immersed titanium horn. In most cases, tubular TiO₂ nanostructures were obtained.¹⁷⁴ Solid NWs could also be formed by raising the sonication power from 280 W (for nanotube synthesis) to 560 W and extending the growth time from 60 to 80 min (Figure 13c). The TiO₂ NWs were obtained directly from the precipitate without further oil-bath treatment (necessary for nanotube formation). The sonication played an important role in accelerating the precursor reactions as well as orienting the TiO₂ crystal growth due to the drastic temperature gradient near the reaction sites.^{174,178} The nanostructures synthesized by this method were typically very small (~5 nm in diameter) possibly related to the localized ultrahigh temperature/pressure generated by acoustic waves. The sonochemical strategy can also be integrated with other processes, such as anodization¹⁷⁹ or electrochemistry.¹⁸⁰ These integrations would significantly increase the growth rate compared to conventional heating and stirring approaches. Mohapatra et al. found that high-quality nanostructure could be produced by applying high viscous solvents such as ethylene glycol under ultrasonic treatment.¹⁸⁰ Although certain controllability on morphology and crystallinity has been shown through this method, due to the vigorous and nonequilibrium reaction conditions, the exact growth mechanism is still unclear.

4.1.6. High Temperature Pyrolysis. High temperature pyrolysis usually combines a hydrothermal process for precursor treatment followed by high temperature sintering. It is a typical ceramic processing technique but not so often seen in TiO₂ 1D nanostructure synthesis. Nevertheless, several successful attempts have been demonstrated to produced 1D TiO₂ nanostructures using modified pyrolysis approaches. Xu et al. synthesized TiO₂ NWs via a molten salt-assisted pyrolysis process. The reaction solution was a mixture of TiCl₄-ethyl acetate (EA) solution and Na₂S ethyl acetate solution. NaCl powders were used to create the molten salt environment at high temperature. At a relatively low calcination temperature (~820 °C), anatase phased TiO₂ NWs were received; while rutile TiO₂ NWs were obtained under a higher temperature of 970 °C.¹⁸¹ Wang et al. synthesized rutile TiO₂ NWs using an inverse microemulsion system containing TiCl₄, ammonia and NaCl as the aqueous phase. Rutile TiO₂ NWs with a diameter of 22 nm and a length of 4 μm were obtained after annealed the precursor Ti(OH)₄/NaCl at 750 °C.¹⁸²

A novel implementation of pyrolysis in nanostructure synthesis integrates sol–gel method, dip-coating, and flame spray pyrolysis, known as sol-flame synthesis.¹¹⁸ As schematically shown in Figure 14a, a typical sol-flame synthesis starts

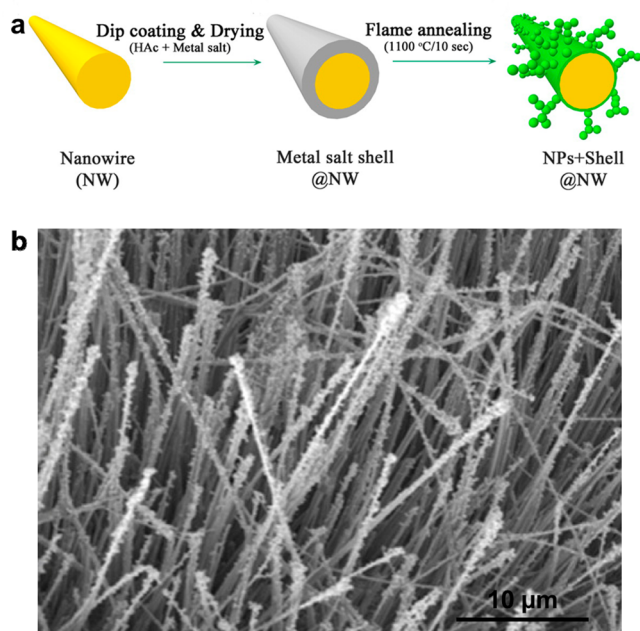


Figure 14. (a) Schematic of sol-flame synthesis procedure. (b) High-density TiO₂ NR branches on the surfaces of CuO NWs synthesized by the sol-flame approach. Reprinted with permission from ref 118. Copyright 2013, the American Chemical Society.

with a nanostructure template, which is then coated with a gel layer. The gel layer can turn into nanostructure branches or dope into the lattice upon flame burning. Through this approach, Feng et al. created high-density TiO₂ NW branches on the surfaces of CuO NWs (as shown in Figure 14b) by coating the CuO NWs with a solution of Ti[OCH(CH₃)₂]₄ in acetic acid and then burning them in a CH₄/H₂ flame for just one minute.¹¹⁸ This group also developed tungsten and carbon codoped TiO₂ NWs using the same sol-flame technique, where H₂WO₄/H₂O₂/C₃H₈O₂ solution and CO gas were used as the W and C doping precursors, respectively.¹⁸³ The flashing heating process could effectively mobilize the dopant elements while keep the morphology and crystallinity of the TiO₂ NWs unchanged. This is the first experimental demonstration of W-/C-co-doped TiO₂ NWs with significantly improved properties.

4.1.7. Electrospinning Methods. Electrospinning is a cost-effective approach for manufacturing nanofibers in large-scale. It uses electric fields and/or spinning force to eject liquid precursors through a fine orifice forming fibrous structures (Figure 15a). Post heat treatment usually is needed to remove the solvent and solidify the fiber structure. Although this technique typically was used for fabricating polymer fibers,^{184–186} many ceramic fibers can be made via the electrospinning process when spinnable precursors are available.^{187–189} The ceramic fiber products are usually polycrystalline and need high temperature annealing to densify the crystal grains and improve the structure stability.

By integrating a sol–gel process to prepare the precursor solution, TiO₂ nanofibers were fabricated via the electrospinning method.¹⁹⁰ Typical solution for spinning TiO₂ nanofibers includes three components: Ti precursor, binder

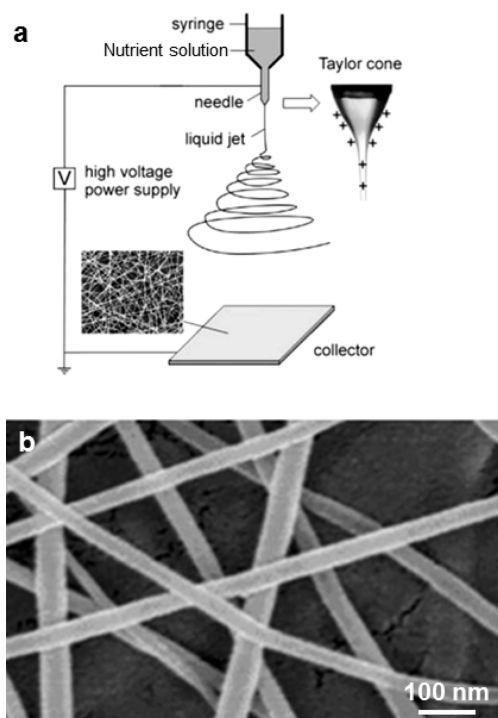


Figure 15. (a) Schematic of electrospinning design. Reprinted with permission from ref 184. Copyright 2004, Wiley Online Library. (b) Ultrafine TiO₂ nanofibers prepared by the electrospinning approach. Reprinted with permission from ref 195. Copyright 2008, Maney Publishing.

and stabilizer. Many Ti-based compounds (either inorganic or organic) can be used as the precursor as long as it is dissolvable and does not leave undesired residues after annealing. Typical precursors include TiP, Ti(OBu)₄, Ti(OiPr)₄, and Ti(OPr)₄.^{87,191,192} A binder refers to a polymer component that holds TiO₂ fine powders together in a fiber shape after spinning. It can serve as the solvent as well and usually is burned off during the final annealing process. Acetic acid is often used as the stabilizer in the solution to control the hydrolysis reaction. For example, Onozuka et al. dissolved TiP and acetic acid into polyvinyl acetate (PVAc) to form a transparent precursor solution and obtained PVAc/titania composite fibers by electrospinning.¹⁹¹ Many researchers used different solvent and binder materials, e.g., ethanol as the solvent and polyvinyl pyrrolidone (PVP) as the binder, for fabricating TiO₂ nanofibers.^{86,87,192} Less binder material and volatile solvent allowed the organic components to be completely removed during sintering and pure polycrystalline TiO₂ nanofibers were obtained. The size of TiO₂ nanofibers usually is determined by the size of the spin orifice. However, formation of ultrafine nanofibers (~40 nm in diameter) needs special solvents. For example, dimethylformamide (DMF), a dipolar aprotic solvent, has been used for fabricating fine TiO₂ nanofibers.^{193,194} It was believed that DMF could enhance the conductivity of the polymer solution. A more conductive solution could provide higher elongation of a jet along its axis due to the enhanced electrostatic force from higher charge density and thus to fabricate nanofibers with smaller diameters.¹⁹³ In addition, DMF is a nonvolatile solvent and increasing DMF ratio in solutions would lower the viscosity.¹⁹⁴ All of these features could help the elongated jet to avoid branching during electrospinning and form uniform fine

nanofibers. With the same procedure, Duan et al. used tetrabutyl titanate as the Ti precursor to prepare ultrafine and uniform TiO₂ nanofibres (Figure 15b).¹⁹⁵

4.2. Vapor-Based Approaches

Vapor deposition is typically conducted in vacuum and under high temperature. Compared to the wet chemistry methods, it offers several unique advantages. First, the high quality of NW's crystallinity is secured due to the utilization of high-temperature and high-vacuum deposition conditions. Second, since the vapor deposition processes are typically performed in conventional thin film deposition systems, the knowledge of thin film growth techniques can be adopted to understanding the NW growth behaviors. Third, control of location, composition, dimension, and organization of NWs could be achieved via vapor deposition processes by engineering catalysts, growth sites, or precursors. Nevertheless, vapor deposition is usually associated with high cost and small scale production. This subsection reviews and compares several representative vapor deposition approaches for TiO₂ 1D nanostructure growth.

4.2.1. Chemical/Physical Vapor Deposition. Chemical vapor deposition (CVD) refers to a process in which vaporized precursor materials decompose or react on particular substrate surfaces to form solid materials. Typically, the precursors are carried by an inert gas and the reaction happens in a vacuum chamber. If there are no chemical reactions involved during the deposition, the process is called physical vapor deposition (PVD). CVD/PVD methods are very popular in nanomaterial synthesis and have been applied to a wide range of materials including semiconductors (e.g., ZnO, TiO₂, Si, and Ge), metals (e.g., tungsten), and insulators (e.g., SiO₂ and SiN).

A mass of work has been performed for synthesizing 1D TiO₂ nanostructures based on CVD/PVD methods.^{56,164,196,197} Ti-based metalorganic compounds are the group of precursors that were commonly used in CVD processes. The corresponding processes are also recognized as metal–organic chemical vapor deposition (MOCVD). Wu et al. used titanium acetylacetonate [Ti(C₁₀H₁₄O₅)] to grow single-crystalline rutile and anatase TiO₂ NRs on silicon substrates at 630 and 560 °C, respectively.¹⁹⁸ This discovery revealed the role of deposition temperature in controlling the NR phase. When the deposition temperature was further lowered to 535 °C, anatase TiO₂ NRs could grow at a very high density forming a nanowall-like structure, possibly due to the largely expedited nucleation rate at a higher level of supersaturation.

The TiO₂ NR orientation can be aligned by introducing single-crystalline substrates with matching crystal lattices. Chen et al. demonstrated well aligned rutile TiO₂ NRs on (100)-oriented sapphire substrates using titaniumtetrakisopropoxide (TTIP, Ti(OC₃H₇)₄) as precursor (Figure 16a).¹⁹⁹ The rutile TiO₂ NRs were grown in a very high density and exhibited a uniform height (Figure 16b). All of the NRs were grown along the [001] direction. The lattice orientation relationship between the basal plane of rutile TiO₂ NRs and the (100) sapphire surface is described as TiO₂ (001) [100] || SA (100) [010], as shown in Figure 16c. The lattice mismatch between the [100]_{TiO₂} ($a = 0.476$ nm) and [010]_{SA} ($b = 0.459$ nm) directions is ~3.57%. This small mismatch allowed epitaxial growth of well-aligned TiO₂ NWs.

Metalorganic precursors offer good controls over the nanostructure morphology and growth rates. However, they have high requirements on the reaction environment and are rather expensive and toxic. Therefore, many inorganic

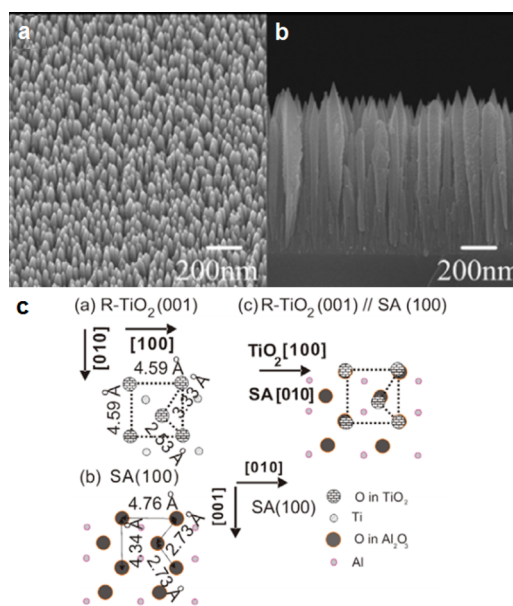


Figure 16. SEM images of vertically aligned and densely packed TiO₂ NRs grown on sapphire (100) substrate. (a) 30° tilted view and (b) cross sectional view. (c) Schematic illustration of the epitaxial relationship between (001) rutile TiO₂ and (100) Sapphire. Reprinted with permission from ref 199. Copyright 2008, Institute of Physics Science.

precursors, such as Ti, TiO, and mineral ilmenite sands (FeTiO₃), have been explored for 1D TiO₂ nanomaterials growth via CVD.^{54,196,199} Single-crystal rutile TiO₂ NWs with lengths of 10–30 μm and mean diameter of 48 nm were synthesized using Ti and TiO as precursors. The growth was conducted at 850–950 °C under atmosphere, where Ar carrier gas was applied (Figure 17a). The growth was seeded by a 50 nm thick Ti layer plus a 2 nm Ni film deposited on the silicon substrate.¹⁹⁹ Similar growth strategy was also demonstrated by Park et al. They illustrated a controlled synthesis of single crystalline TiO₂ NWs on Ni/Ti/SiO₂/Si substrate *via* a combined vapor–liquid–solid (VLS) and vapor–solid (VS) process using TiO powder the evaporation source.²⁰⁰ It was suggested that the longitudinal growth was control by the VLS mechanism where Ni/Ti alloy served as the catalysts. Meanwhile, direct condensation of TiO₂ on the NW side walls occurred simultaneously during the growth due to the high concentration of vapor-phase reactant at the deposition region. This VS process was able to control the diameter distribution of TiO₂ NWs.

Direct oxidation of Ti was also found to be effective for the formation of TiO₂ 1D nanostructures. It typically needs other metals to facilitate the anisotropic 1D growth. Figure 17b shows rutile TiO₂ NWs that were prepared by oxidizing a thermally evaporated Ti film under O₂ gas flow, where another thin layer of Au served as the catalyst.⁵⁴ During the growth, a quartz or sapphire substrate covered with 500 nm Ti and 50 nm Au was placed at 1050 °C under Ar and O₂ flow. The authors believed Ti vaporized and transported to gold droplet forming NW structure after oxidation by the O₂ gas following a VLS process. TEM investigation shows that the TiO₂ NWs grown on (0001)-oriented sapphire substrates had twinned structure, while no dislocations were observed from the TiO₂ NWs grown on quartz substrates.

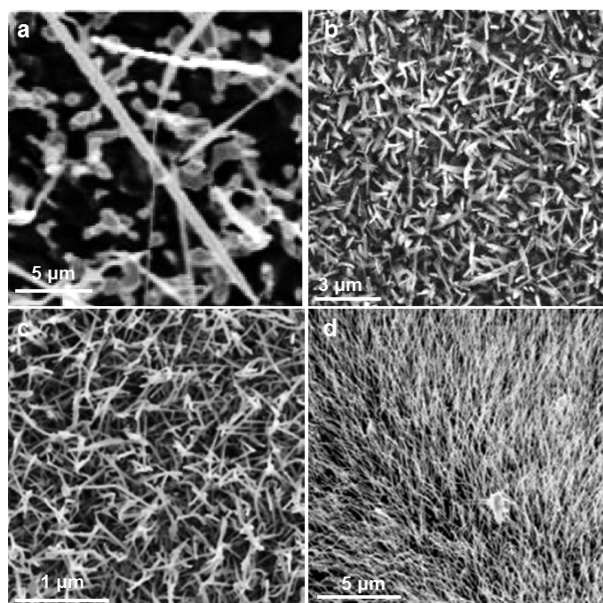


Figure 17. Representative SEM images of TiO₂ NWs synthesized by vapor deposition. (a) TiO₂ NWs grown on a Ni/Ti/SiO₂/Si substrate using TiO as the precursor. Reprinted with permission from ref 199. Copyright 2008, American Institute of Physics. (b) TiO₂ NWs grown on a Au/Ti/sapphire substrate using Ti as the precursor. Reprinted with permission from ref 54. Copyright 2006, Institute of Physics Science. (c) TiO₂ NWs grown on a TiO₂-coated sapphire substrate using Ti as the precursor. Reprinted with permission from ref 57. Copyright 2006, Institute of Physics Science. (d) TiO₂ NWs grown on a Si substrate using Ti as precursor. Reprinted with permission from ref 55. Copyright 2005, Institute of Physics Science.

Pure Ti metal powders or foils have also been used as the precursor source by many researchers. Wu et al. thermally evaporated Ti powder at 850 °C and grew single-crystalline rutile TiO₂ NWs on a TiO₂-covered sapphire substrate (Figure 17c).⁵⁷ The deposition chamber was kept at a low pressure of 1 Torr and filled with argon gas. Oxygen was added after the growth temperature was reached. Through a similar approach, Xiang et al. synthesized single-crystalline TiO₂ NWs on Si substrates using Ti metal powder as precursor (Figure 17d).⁵⁵ In Wu's experiment, polycrystalline TiO₂ layer was used as the nucleation sites to guide the deposition of the Ti/TiO₂ species and the NW growth was governed by the VS process. A low chamber pressure (~1 Torr) was desired to achieve high Ti partial pressure, which was favorable for direct vapor deposition and oxidation. When Si was used as the substrate, the O and Ti species would dissolve into Si and form nanosized Si–O–Ti alloy islands on the Si–Ti alloy film covering the substrate surface. Continuous supply of Ti and O₂ vapor to the quasi-liquid Si–Ti–O nanosized islands led to 1D growth of TiO₂ single crystals following the VLS process. A relatively high chamber pressure (~300 Torr) corresponded to a low Ti partial pressure, which was preferred by a VLS NW growth for achieving uniform sizes and lengths.⁵⁷ Direct deposition of Ti vapor from metallic Ti source is the simplest and most straightforward approach for growing TiO₂ 1D nanostructure from the vapor phase at elevated temperature. However, it was challenging to achieve a fine control over the Ti vapor pressure during the growth. Therefore, the TiO₂ NW morphology was usually less defined and the reproducibility was not as good as other approaches, such as MOCVD.

4.2.2. Atomic Layer Deposition-Related Methods.

Atomic layer deposition (ALD) technique is a cyclic self-limited CVD process using separated precursor pulses. It has been widely applied to the growth of conformal thin films with precisely controlled thickness down to the subnanometer level.²⁰¹ Based on this strategy, Shi et al. recently developed the SPCVD technique that can grow highly uniform single-crystalline TiO₂ NRs over a large area, even inside highly confined submicrometer-sized spaces.⁷⁰ TiO₂ SPCVD operates at 600 °C and uses pulsed TiCl₄ and H₂O vapor precursors (1.5 s each) that were separated by N₂ purging for 60s. Because of the similar cycle-wise operation process as ALD, SPCVD inherited the unique conformal-coating merit of ALD and was able to achieve conformal growth of TiO₂ NRs arrays inside highly confined spaces, such as anodic aluminum oxide (AAO) nanochannels. Formation of NR morphology was believed to be due to the high deposition temperature and elongated purging time.

The as-grown anatase TiO₂ NR-coated AAO channel is shown in Figure 18. Figure 18a shows the cross section of the AAO

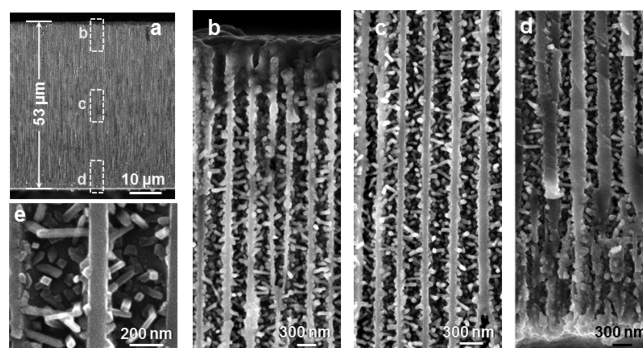


Figure 18. SEM images of anatase TiO₂ NRs grown inside AAO channels by the SPCVD technique. (a) Cross sectional image of the TiO₂ NR-covered AAO template. Higher magnification image of the top section (b), middle section (c), and bottom section (d) of the AAO channel shown in panel a. (e) Morphology and distribution of TiO₂ NRs in the AAO channels. Reprinted with permission from ref 70. Copyright 2011, the American Chemical Society.

template after 660 cycles of SPCVD growth. SEM images acquired from the top, middle, and bottom sections are shown in Figure 18b–d, respectively, revealing the uniform and dense coverage of TiO₂ NRs along the entire channel length. All NRs were rooted on the walls of the AAO channels and pointed inward (Figure 18e). Majority of the as-synthesized TiO₂ NRs had lengths and widths of between 170 and 210 nm and 25–30 nm, respectively. TEM and XRD spectrum revealed that the NWs were single-crystalline anatase TiO₂.

Using the SPCVD technique, TiO₂ NWs can be grown on a variety of surfaces inside confined spaces. Figure 19a demonstrated a uniform coverage of TiO₂ NWs on the entire surface of dense Si NWs.¹¹⁹ The Si NWs used in the experiments were fabricated by deep reactive ion etching (RIE) using silica spheres as a mask. The length of the Si NWs were ~15 μm and the spaces in between were only 200–300 nm. This result demonstrated the versatility of the SPCVD technique for making TiO₂ NW arrays inside different material matrixes. Such high-density 3D branched NW architectures are particularly useful for solar cell electrode development.

By controlling the growth cycles, SPCVD can also introduce point defects, such as dangling –OH and –Cl groups into TiO₂

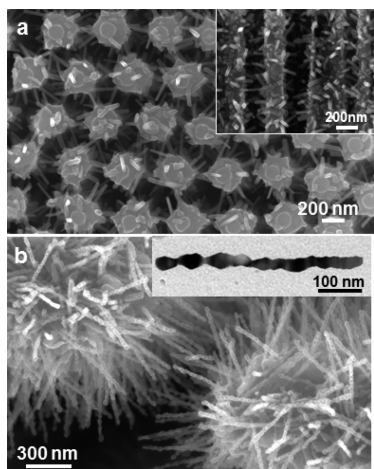


Figure 19. (a) TiO₂ NRs grown on vertically aligned Si NW surfaces. Inset is cross sectional image of the heterostructure. Reprinted with permission from ref 119. Copyright 2011, the American Chemical Society. (b) Defective TiO₂ NWs grown by SPCVD with modified precursor ratios. Inset shows an individual TiO₂ NW with a necklace-like morphology. Reprinted with permission from ref 74. Copyright 2012, the Royal Society of Chemistry.

NW lattices.⁷⁴ In this case, increased water exposures and reduced TiCl₄ exposures were applied. The as-synthesized TiO₂ NWs exhibited larger aspect ratio than those made via regular SPCVD process. (Figure 19b) They were typically 20–30 nm in diameter and ~500–600 nm long with a very narrow dimensional distribution. All of the TiO₂ NWs had a necklace-like structure that was composed of coherent nanocrystals with nearly identical sizes and diamond-like shapes, indicating the oriented attachment growth mechanism. The defective TiO₂ NWs exhibited broader band absorption and photoactivity in the visible light regime.

4.2.3. Pulsed Laser Deposition. Pulsed laser deposition (PLD) is one type of physical vapor deposition, where a pulsed high power laser beam is used as the heating source. Upon the laser beam illumination, the target material can be vaporized stoichiometrically in vacuum and then deposits onto a substrate with the same stoichiometric ratio. Although mostly used in thin film deposition,^{202–205} PLD has recently been involved in the synthesis of 1D TiO₂ nanostructures. The morphology evolution of nanostructured TiO₂ via PLD process was studied by Noh et al.²⁰⁶ Using a high purity (99.99% pure) TiO₂ target and the KrF excimer laser (248 nm, 1.5 J cm⁻², and 5 Hz), TiO₂ nanostructures were deposited on a fluorine-doped tin oxide (FTO) glass under the oxygen pressure ranging from 25 mTorr to 300 mTorr. In the PLD process, the morphology was directly controlled by the surface diffusion of the TiO₂ species, which was related to two major factors: kinetic energy of the ablated TiO₂ and the thermal energy provided by the substrate temperature. At constant deposition temperature, the TiO₂ morphology was primarily controlled by the working pressure, because the ablated TiO₂ species would have more collisions with gas molecules at higher pressure and lose their kinetic energy before reaching the substrate, and thus less surface diffusion. As a result, more porous or isolated nanostructures were obtained under higher working pressure. For example, when the pressure increased from 25 mTorr to 100 mTorr, the dense TiO₂ film was transformed to vertically aligned NR-like structures (Figure 20a). At higher working pressure of 300 mTorr, films with loose interparticle connections were formed

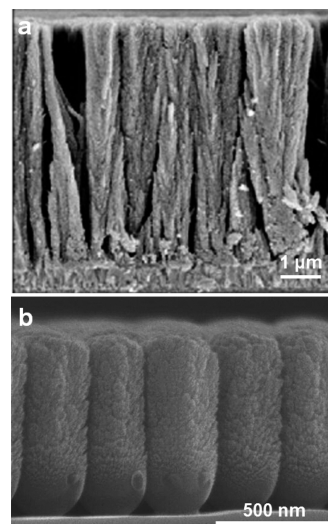


Figure 20. (a) Cross sectional SEM image of a dense TiO₂ NW film deposited by PLD. Reprinted with permission from ref 206. Copyright 2012, the American Chemical Society. (b) PLD TiO₂ nanocolumns grown on a PS sphere monolayer template. Reprinted with permission from ref 208. Copyright 2008, the American Chemical Society.

owing to the significantly reduced amount of deposited TiO₂ species. Similar results were also obtained by Sauvage et al. in their PLD TiO₂ experiments.²⁰⁷

Instead of directly depositing TiO₂ by PLD, templates were also used to facilitate the PLD growth of 1D TiO₂ nanostructure. Li et al. fabricated TiO₂ periodic NRs arrays on silicon substrates using rutile TiO₂ as the target and polystyrene (PS) microsphere monolayer to control the NR distribution.^{208,209} A hexagonal-close-packed TiO₂ NRs array was obtained with one NR standing on top of each PS sphere (Figure 20b). Due to the relatively low substrate temperature, this process was simply physical accumulations of TiO₂ materials and did not involve any crystal growth as other vapor deposition methods did. As a result, the NRs were amorphous or had very poor crystallinity. However, the low substrate temperature allowed the PS sphere pattern to be well preserved during deposition. By removing the PS sphere in a CH₂Cl₂ solution, a free-standing TiO₂ NR membrane could be peeled off from the substrate.²⁰⁸ Besides, the PS spheres could also be removed by annealing at 650 °C for 2 h in air, yielding a periodic NR array on the silicon substrate.²⁰⁹ Sauthier et al. modified above process for preparing nitrogen-doped TiO₂ vertically aligned nanocolumns by adding a second PLD procedure after depositing TiO₂ hemispheres and removing the PS template by 500 °C annealing.²¹⁰ The doping amount of nitrogen was setting by adjusting the nitrogen partial pressure inside the PLD chamber. The as-synthesized N-doped TiO₂ nanocolumnar arrays showed mixed rutile and anatase polycrystalline phases.

4.3. Templated Growth

In general, template growth is a very versatile synthesis technique that forms nanostructure with a morphology that follows the porous template. It was combined with different pore-filling techniques based on the chemical and physical properties of templates and targeting materials as well as the pore geometry. Solid nanostructures can also be used as templates to define the coating geometry.^{211–215} Since this approach only leads to tubular or porous structure, it will not

be covered in our discussion. The significant advantage of the templating technique is that it can form designed nano-geometry independent of the materials lattice preferences. Therefore, templated growth is particularly useful for making 1D nanostructures from materials that do not naturally show preferred fast growth axis.^{216–219} TiO_2 is within this category and many researchers have applied this technique to grow TiO_2 NW arrays. However, one significant drawback of this method is the crystal quality and purity control during template filling and removing. Here, we review several representative templated growth approaches for making TiO_2 NWs and the corresponding results are discussed.

4.3.1. Sol–Gel Template Methods. The sol–gel methods, due to their simple solution-based process and broad selections of precursor, were often the first choice for filling tubular templates to create 1D TiO_2 nanostructures.^{220–223} The most common nanotubular template is AAO. However, it is always challenging to completely fill a nanosized narrow tube via simple solution infiltration and solidification. As a result, most products exhibit a tubular structure with various diameters and wall thickness, i.e., TiO_2 nanotubes, which is beyond the scope of this review.^{221,222}

It was suggested that a long immersing time of the AAO membrane and a high solution temperature would lead to complete filling of the template channel and thus the formation of TiO_2 NWs. [001]-oriented anatase TiO_2 NWs were obtained by this method.²²⁴ Attar et al., and Ren et al. synthesized TiO_2 NR and nanotube arrays via the sol–gel template method using AAO templates as well, and the typical NW morphology is shown in Figure 21a.²²⁵ Their experiments showed that a sol–gel template process usually started with nucleation around the side walls in the template pores. Therefore, a tubular structure was always developed first. Afterward, competition between the equilibrium growth rate on the side walls and the diffusion rate of charged sol particles down the pore became the key factor

that determined the final morphology (NR or nanotube). If the diffusion rate of positively charged sol particles exceeded the equilibrium growth rate on the pore walls, the sol particles would be deposited on the pore's base, forming a solid NW. Otherwise, the sol particles would continuously attach to the pore walls, growing horizontally and forming a tube.²²⁶ Due to the use of templates, this approach demonstrated a good dimension controllability and uniformity over a very large scale of 1D TiO_2 nanostructure arrays. However, as shown in Figure 21b, the as-received TiO_2 NWs typically had poor crystallinity and rough surfaces, which may be harmful for electron transportation and make it challenging for applications as photocatalyst, electrodes, and electronic devices.

4.3.2. Suspended Molecular Template Methods. A suspended molecular template refers to 1D molecular level structures, such as carbon nanotubes and wire-shaped organic molecules that are suspended and dispersed on a supporting substrate. They can serve as templates to direct the deposition of desired materials by sputtering, electron beam evaporation, etc. and forming 1D nanostructures.^{227–229} Lee et al. demonstrated such a process for synthesizing Co-doped TiO_2 NWs. Flexible organic poly(3,4-ethylenedioxythiophene) (PEDOT) NWs were used as suspended templates for the growth of Co-doped TiO_2 NWs by a conventional reactive radio frequency magnetron sputtering technique. The as-prepared NWs were ~ 200 nm in diameter with a ~ 50 nm thick Co- TiO_2 layer covering the template wires.²³⁰ The NW was polycrystalline and consisted of a chain of NPs on the molecular template. One unique advantage of this approach was that the position of the as-grown NWs could be defined by the molecular NW templates, which could be much more easily positioned or manipulated. For example, an individual PEDOT NW was suspended between a pair of prefabricated Nb electrodes. Thus, after coating, the Co-doped TiO_2 NW was formed directly between the electrodes allowing immediate applications as an electronic device (Figure 21c). Therefore, although this technique might not be ideal for fabricating 1D TiO_2 NWs in large scale, it provided a unique and facile approach for characterizing the physical properties of individual NWs.^{229,230}

4.3.3. Electrochemical Deposition Methods. Electrochemical deposition is a widely used manufacturing process for depositing films onto a conductive surface through electric field-induced electrochemical reactions. Despite its long history in material processing from art to science, electrochemical deposition found great potential in nanomaterial synthesis in recent years due to its good material selectivity and morphology controllability.^{56,231–235}

Zhang et al. described a way to synthesize TiO_2 NW arrays via anodic oxidative hydrolysis of TiCl_3 within a hexagonal close packed AAO template on an Au substrate (Figure 21d).²³⁶ The layer of Au film was deposited as an electrode on one side of the anodic porous alumina template. Growth of TiO_2 NWs was performed at 25 °C, pH 2.5, and under Ar atmosphere. The as-received TiO_2 NWs were annealed at 500 °C to obtain the anatase phase. In the anodic oxidative hydrolysis of TiCl_3 , the rate of anodic Ti^{3+} oxidation was controlled by the hydrolytic pre-equilibrium forming TiOH^{2+} . Since the AAO pore walls were positively charged due to the large quantity of surface vacancies, the TiOH^{2+} molecules were repelled by the walls and went down the pores and grew into NWs from the bottom. Compared to sol–gel templating methods, this technique is more time efficient and more

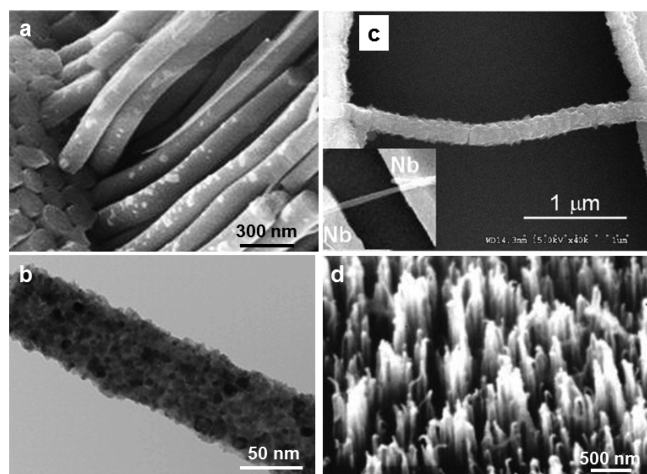


Figure 21. (a) SEM image of TiO_2 NWs synthesized using AAO templates. (b) TEM image show of an individual NW showing the rough surface and low crystallinity. Reprinted with permission from ref 225. Copyright 2009, Elsevier Ltd. (c) A Co- TiO_2 NW suspended in between two Nb electrodes fabricated using a PEDOT NW as the template. The NW template is shown in the inset. Reprinted with permission from ref 230. Copyright 2005, American Institute of Physics. (d) Vertically aligned anatase TiO_2 NW array synthesized by electrochemical template filling method. Reprinted with permission from ref 236. Copyright 2001, the Electrochemical Society.

controllable for achieving well aligned NWs with uniform dimension and morphology. However, because this process involves charge transport, the requirements of precursor chemicals are much more restrictive and supporting substrates need to be conductive. Again, the electrochemical deposition can also be used to deposit TiO₂ nanotube structures given appropriate templating structure and deposition conditions.^{237,238}

4.4. Top-down Fabrication Techniques

Top-down fabrication techniques describe the creation of nanostructures from the bulk form. This approach typically is able to process a large quantity of nanostructures with uniform morphology and orientation. For TiO₂ 1D nanostructures, a top-down process usually starts from a bulk Ti foil followed by selective etching and/or oxidization. Here, significant progresses of these techniques and their outcomes will be review.

4.4.1. Direct Oxidation of Titanium Sheets. Ti has very good thermal and chemical stabilities within a wide temperature range. Therefore, as we discussed earlier, different metals are often needed to facilitate the melting and to initiate catalyzed NW growth. However, it was found that in the presence of appropriate organic vapor Ti metal can be directly oxidized forming NW structures.

Daothong et al. showed a size-controlled growth of TiO₂ NWs by oxidizing Ti wires (~0.25 mm in diameter) in the presence of ethanol vapor at low pressure (~10 Torr) and high temperature (650–850 °C), as shown in Figure 22a. The

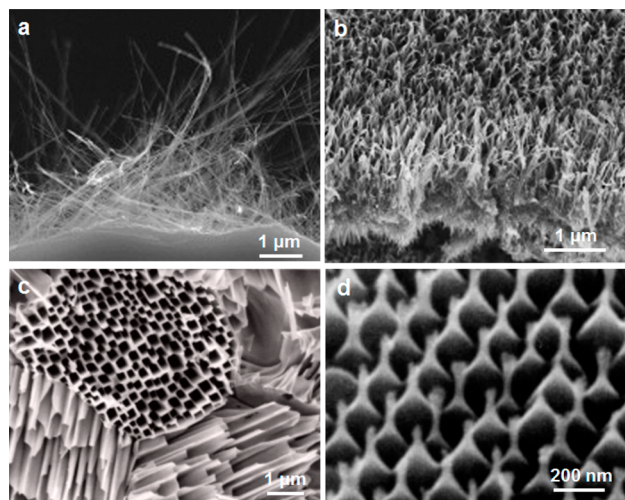
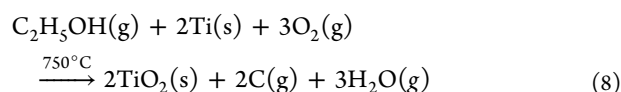
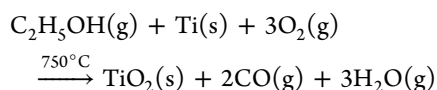


Figure 22. (a) TiO₂ NWs grown by oxidizing titanium metal wires in ethanol vapor. Reprinted with permission from ref 239. Copyright 2007, Elsevier. (b) TiO₂ NWs grown on Ti substrate by oxidizing the Ti substrate in aqueous hydrogen peroxide, melamine and nitric acid mixture solution. Reprinted with permission from ref 247. Copyright 2010, Elsevier. (c) TiO₂ Nanohoneycomb structure obtained by PEC etching. Reprinted with permission from ref 252. Copyright 1999, the Electrochemical Society. (d) TiO₂ NR arrays photoetching TiO₂ substrate following a mechanically imprinted pattern. Reprinted with permission from ref 253. Copyright 2003, Wiley-VCH.

following reactions were proposed to explain the formation of TiO₂ NWs:



The NW diameter was strongly related to the oxidation temperature (the thinnest NWs with a diameter of ~23 nm were obtained from 750 °C oxidation); while the length of NW was directly proportional to the oxidation time. The size-temperature relationship was possibly a result of the oxidation reaction rate. According to above reactions, the size might also have a certain dependence on the oxygen partial pressure, which has yet to be tested experimentally.²³⁹

Following this work, Huo et al. demonstrated quasi-aligned TiO₂ NW/carbon nanocone core-shell nanostructure arrays produced from Ti substrate via a simple one-step thermal reaction under acetone vapor at 850 °C. At elevated temperature, acetone would decompose into –CH₃ radicals and CO. Because of the low oxygen concentration in the system, CO would act as the oxidation reagent to convert Ti into TiO₂ and form C. The high carbon content led the accumulation and formation of carbon shell around the TiO₂ NWs. It was also suggested that the temperature gradient between the top and bottom of the NWs and the hydrogen etching from the decomposition of –CH₃ might be the reason of the conical NW shape.^{240,241} Generally, the NWs produced from the direct oxidation methods were thin and typical mean diameters were less than 100 nm.^{239,240} However, the NW arrays still suffer from their poor orientation alignment, which may limit their application potentials.

4.4.2. Electrochemical Etching Methods. Electrochemical etching is a metal etching process which relies on surface reduction/oxidation (redox) reactions to selectively remove certain portions of the bulk material and leave 1D nanostructures.²⁴² The redox reactions can be activated by applying electric bias or introducing redox reactants. Many researchers have synthesized TiO₂ 1D nanostructures via electrochemical anodization of Ti foils or sheets.^{89,243–246} Due to the nature of etching selection, most products were TiO₂ nanotube arrays. Here, we focus our discussion on NW formation through the etching method, though the NW product was relative rare.

Tao et al. fabricated TiO₂ NW arrays with pickling Ti foil in 50 mL of a 30 mass% H₂O₂ solution which contained 15 mg of melamine (C₃H₆N₆) and 1.0 mL of 63 mass% HNO₃, and was kept at 80 °C for 72 h.²⁴⁷ The Ti foil were immersed in a 1:3:6 (in volume) mixture of a 55 mass% HF aqueous solution, a 63 mass% HNO₃ aqueous solution and distilled water for 2 min, followed by ultrasonic clean. The sample was finally washed in DI water, dried at 80 °C, and annealed at 450 °C for 1 h in air. The NWs were polycrystalline anatase with diameters of 25 nm and lengths of ~1 μm (Figure 22b). It was suggested that the NWs were formed via deposition of Ti-based species from oxidizing the Ti substrate. This argument was partially supported by the observation that if the Ti foil was oxidized in a mixture of glycol and water containing NH₄F, the TiO₂ tubular structure would be received. However, clear and direct understandings of the morphology selectivity are still lacking. Wang et al. found that TiO₂ NWs could be formed on the top of TiO₂ nanotubes fabricated through electrochemically anodizing Ti foil in fluorine-containing ethylene glycol electrolyte.²⁴⁸ Formation of TiO₂ NWs was attributed to electric field induced chemical etching of the TiO₂ nanotubes, i.e., the anodically grown nanotubes vertically split during a

long period of anodization. The as-received TiO₂ NWs were amorphous and can be separated from the TiO₂ nanotubes by multistep washing and sonicating.

4.4.3. Photoelectrochemical Etching methods. When TiO₂ is used as photoelectrode in a photoelectrochemical (PEC) cell, its surface may suffer corrosion and morphology changing during photo-oxidation reactions.²⁴⁹ This is known as PEC etching or photoetching, which, if well controlled, can effectively convert flat TiO₂ crystalline surfaces into organized 1D nanostructures.^{250,251}

Sugiura et al. synthesized TiO₂ nanohoneycomb structure by PEC etching of sintered TiO₂ pellets. The *n*-type TiO₂ pellets acted as the photoanode in a 0.1 M H₂SO₄ aqueous solution under UV illumination following the reaction:



The PEC etching yielded 1D quadrangular nanochannel arrays on the TiO₂ pellets, as shown in Figure 22c. Selective area electron diffraction (SAED) pattern suggested that the etching occurred was along the [001] direction of rutile TiO₂. The four walls of the quadrangular cells were identified to be the {110} crystal facets possibly due to their good chemical stability and low surface energy.²⁵² Kisumi et al. later showed a very similar nanostructure in their PEC experiments when rutile TiO₂ (001) wafer was applied as the photoanode in aqueous H₂SO₄.⁸⁸

Similar to electrochemical etching, the PEC etching typically yielded interconnected vertical walls following certain crystal facets. This always led to bundles of 1D nanochannels. However, if certain confinements were applied to the TiO₂ surface to control the etching orientation and rates, NW morphology would be created. Masuda et al. reported a fabrication of ordered arrays of NRs by PEC etching on TiO₂ single crystals (Figure 22d).²⁵³ (001)-orientated single-crystalline rutile TiO₂ was used as the substrate. A SiC mold with a triangular nanotip array was used to imprint an array of very small dimples on the TiO₂ surface. The dimpled areas exhibited a much lower etching rate compared to the flat areas. Thus, vertically aligned TiO₂ NR arrays were obtained on the TiO₂ photoanode surface after PEC etching under 150 W high pressure Xe lamp illumination and 1 V bias.

5. PROPERTIES AND APPLICATIONS OF 1D TiO₂ NANOMATERIALS

Generally, bulky TiO₂ is a wide band gap *n*-type semiconductor.²⁵⁴ Nanoscale forms like NPs and NWs are peculiarly important since they offer larger surface area, more reaction sites, higher volume of depletion regions, and possible quantum confinement effects compared to the bulk structures. These merits are substantially deterministic in boosting the performances of energy, sensing and catalysis-related manifestations. Different from NP films in which electrons walk randomly and often interact with scattering sites resulting in a high probability of charge recombination, the NW structures may serve as confined conductive channels, where their longer charge diffusion lengths could reduce charge recombination and facilitate charge transport. Therefore, 1D TiO₂ nanostructures are often regarded as a highly efficient framework highlighted by their fast charge transport and collection abilities in emerging applications such as photovoltaics, photocatalysis, energy storage systems, electrochromic devices and sensor devices.^{255,256} The intrinsic and morphology-related properties

of 1D TiO₂ nanomaterials and corresponding applications are reviewed in this section.

5.1. Electronic Property and Photocatalytic Applications of 1D TiO₂ Nanomaterials

TiO₂ is a widely used photocatalytic material due to its excellent stability, suitable electronic property and environmentally benign nature.^{248,257,258} In general, in a photocatalysis process, electron–hole pairs are created inside TiO₂ upon absorbing photons with energy larger than the band gap. The photogenerated charges then separate and transfer outside to react with chemicals that are adhered on the TiO₂ surfaces.^{259–261} In principle, the photocatalytic efficiency is controlled by light absorption, charge transport, number of surface reaction sites, and redox reaction rates. The light absorption wavelength range can be adjusted by electronic band structure engineering of TiO₂. Charge transport property and redox reaction rate can be modified by introducing doping elements into the TiO₂ lattices.¹² Number of reaction sites is directly related to the active surface area. Owing to the unique and controllable electronic properties as well as the large surface-to-volume ratio associated with the 1D morphology, TiO₂ NWs have received considerable research interests in advanced photocatalysis applications.

5.1.1. Size-Related Electronic Property of TiO₂ NWs.

Size, facets, phases and growth orientations are the most interesting aspects leading to versatile electronic properties in NW morphology. As the NW size shrinks to the nanometer scale, the NW band gap starts to increase dictated by the quantum size effects. The shifting of valence and conduction band and its alignment with certain redox potentials could therefore be optimized to facilitate corresponding redox reactions occurring on the TiO₂ NW surfaces. Serpone et al. found the exciton radius (r_{ex}) of TiO₂ was in the range of 0.35–1.9 nm.²⁶² Later Iacomino et al. concluded that the TiO₂ r_{ex} was at least 1.5 nm based on their density functional theory (DFT) calculations.²⁶² For NWs grow along the [001] direction, the blue shift with respect to the bulk value was estimated to range from 0.18 to 0.67 eV depending on the size of the NWs. Iacomino et al. predicted that when the majority of TiO₂ (anatase) surface are (101) and (001), TiO₂ NW would retain their bulky electronic properties and barely exhibit any quantum confinement.²⁶³ NW structural distortions were also found to be harmful in enabling quantum size effects.

The electronic band structure of TiO₂ is very important for its applications in catalysis and electrochemistry. For example, in TiO₂-catalyzed water redox reactions, the band alignment between hydrogen reduction potential and conduction band minimum (CBM) must be in a proper configuration. Bulk anatase TiO₂ is considered more preferable for hydrogen reduction compared to its rutile phase because the CBM of anatase TiO₂ is ~0.2 eV higher than that of rutile TiO₂. The size-related quantum effects is able to modulate the CBM of NWs of both rutile and anatase phases, and thus engineer their capability of catalyze electrochemical reactions on the surfaces. Iacomino et al. calculated the VBM and CBM of TiO₂ NWs with and without water or hydrogen coverage, which revealed the significance of band alignments between TiO₂ NW and chemical redox potentials for photocatalysis (Figure 23).

Peng et al. found that the quantum confinement effects of rutile TiO₂ NW becomes significant when its diameter is smaller than 2.5 nm.²⁶⁴ Their first principle calculations predicted the band shift of rutile TiO₂ NW as a function of

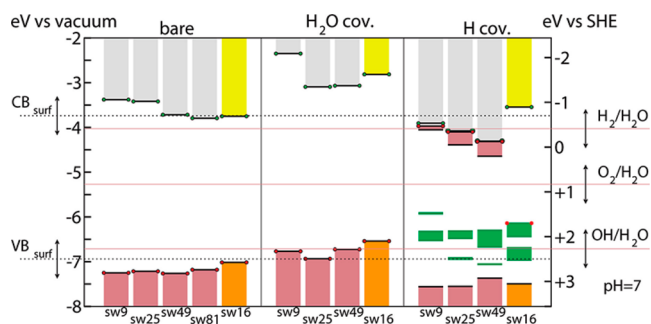


Figure 23. Band line-up of the TiO₂ NWs in the gap region. Brown bars indicate occupied states; gray bars for empty states; green for hydrogen-induced in-gap states; red circles for the HOMO energy level; green circles for the LUMO energy level. The dotted horizontal lines are the experimental HOMO and LUMO energy levels. Continuous horizontal lines are the energy value of relevant redox potential couples at pH 7. Reprinted with permission from ref 263. Copyright 2010, the American Chemical Society.

its diameter, which follows the relationship: $\Delta E_g = \beta/d^d$. Figure 18a shows the band gap of TiO₂ NW as a function of its diameter d for different cross-section atomic structures. NWs surrounded by (100) crystal surfaces show much weaker quantum confinement effect than others. It was found that the existence of anisotropic quantum confinement effect is mainly due to the anisotropy of the effective masses in NW structures, as indicated by the different slopes of energy functions (versus diameter, shown in Figure 24a) of four types of NW cross

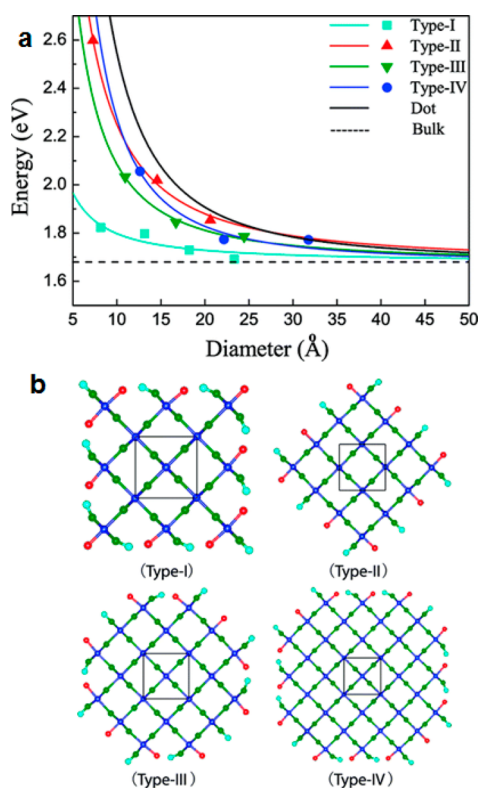


Figure 24. (a) Band gap as a function of the diameter d of the NW in different structures. (b) Four types of cross sections of TiO₂ NWs: the blue spheres are the Ti atoms, the green ones are the O atoms, and the red and cyan ones are corresponding pseudohydrogen atoms. Reprinted with permission from ref 264. Copyright 2008, the American Chemical Society.

section structures shown in Figure 24b. Tafen et al. investigated the electronic properties of anatase TiO₂ NWs by DFT calculations and revealed that for round- and hexagonal-shape NWs growing along the [001] direction, their band gap enlargement is proportional to the reciprocal of their perimeter's square ($\Delta E_g = A/P^2$), as shown in Figure 25.²⁶⁵

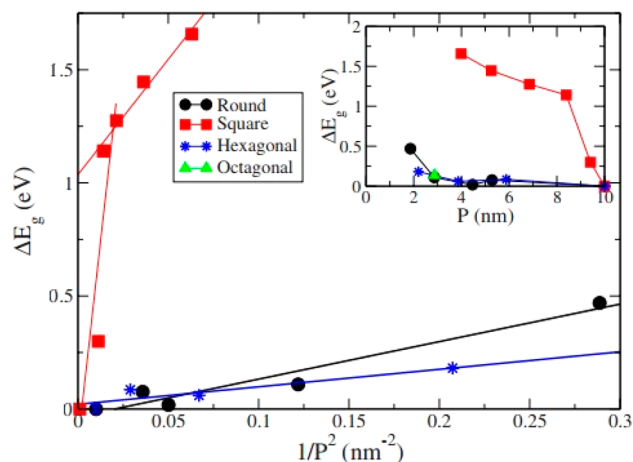


Figure 25. Shift of the band gap with respect to bulk TiO₂ anatase as a function of $1/P^2$. Reprinted with permission from ref 265. Copyright 2009, the American Physical Society.

Such a relation failed when it was applied to square-shape NWs possibly due to the pronounced effect of surface tension and surface charge-induced electronic shifting of molecular orbitals. Studies on the quantum confinement effects of TiO₂ NWs structure shed light on the design of efficient photoactive TiO₂ nanomaterials for their implementations in photocatalysis and photodetectors. However, due to the limited capability of synthesizing high quality ultrathin TiO₂ NWs in that size regime, most of the theoretical analyses are yet to be demonstrated experimentally.

5.1.2. Foreign Element Doped TiO₂ NWs. Although TiO₂ exhibits many merits as a promising photocatalytic material, a major drawback of intrinsic TiO₂ is its large band gap, which constrains the absorption only in the UV light range. This limitation seriously impairs the energy conversion efficiency when TiO₂ is used as the light absorber in PEC systems. Doping foreign elements into TiO₂ lattices has been the main strategy to reduce the optical band gap and align the band edges properly with target products' redox reaction levels.²⁶⁶ Many research efforts have been allocated on fabricating doped TiO₂ NWs and investigating corresponding electronic and optical property changes.

Without considering the degradation of charge mobility in TiO₂ NW, anionic doping would be ideal for band gap engineering for the application of photoanode in PEC water splitting, because it could introduce acceptor levels above the O 2p orbital and meanwhile hold a positive driving potential for water oxidation. A cationic doping introduces donor levels to reduce the band gap but often the donor levels are lower than the potential of water reduction reactions. Thus an external bias is required to drive the water splitting to occur. Nitrogen has been propounded to be a promising solution for TiO₂ NW doping.^{267,268} It can be easily achieved by annealing TiO₂ NWs in NH₃ atmosphere with adjustable N doping concentration (by annealing temperature, time, and NH₃ pressure).²⁶⁹ Hoang

et al. demonstrated visible light driven PEC water-splitting using N-doped TiO₂ NWs.²⁶⁹ The low-energy threshold of the incident photon to current efficiency (IPCE) spectra of N-doped TiO₂ sample was at ~520 nm, where the corresponding IPCE was 1.7%. The performance was further improved (photocurrent density increased from 0.23 mA/cm² to 0.61 mA/cm² at 1.23 V vs reversible hydrogen electrode, RHE) by decorating TiO₂ NW surface with a layer of cobalt elements. Cobalt treatment was suggested to passivate surface states on the N-modified TiO₂ surface and act as a water oxidation cocatalyst.²⁶⁹ Hoang et al. also reported a synergistic effect involving hydrogenation and nitridation cotreatment of TiO₂ NW arrays.²⁶⁹ The visible light (>420 nm) photocurrent of the cotreated TiO₂ was 0.16 mA/cm². Interaction between the N-dopant and Ti³⁺ was expected to be the key for realizing the spectrum extension and visible light photo-oxidation activities.

However, most experiments on photocatalysis and PEC water splitting showed that the enhancement of solar energy conversion efficiency of N-doped TiO₂ NWs was actually much lower than the expectations, though the visible light absorption ability was largely enhanced.^{270,271} Recent experiments and DFT simulations revealed that the charge recombination rate increased along with the doping of N element.^{270,272} Wang et al. found that in N doped anatase TiO₂ NBs (N is located in the interstitial site of the anatase lattice when doping concentration is lower than a certain level; above this level, extra N goes to the substitutional position), nitrogen positions its N 2p levels above the VBM. Color centers induced by the oxygen vacancies and 3d states of Ti³⁺ species below the conduction band are naturally created.²⁷⁰ Visible light absorption and photoactivity arise from these defects levels. However, oxygen vacancies and the Ti³⁺ species can drastically escalate the recombination rates of photoexcited electron and holes. Overall, the photoactivity of the N-doped TiO₂ NBs manifested in the visible light regime was almost completely compensated by the decreased photoactivity in the UV region. Figure 26 shows the photocatalytic activities of pristine and

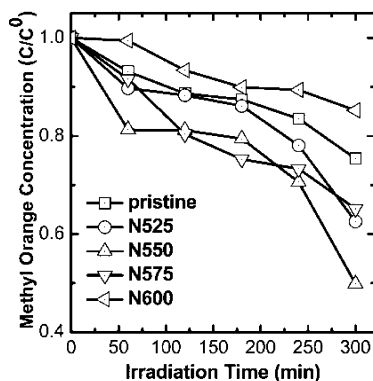


Figure 26. Photocatalytic activities of TiO₂ NBs under visible light illumination. Reprinted with permission from ref 270. Copyright 2009, the American Chemical Society.

four TiO₂ NB samples doped with different concentrations of N element. To maximize the overall efficiency by balancing visible light absorption ability and defects-induced recombination, doping elements, concentrations, and distributions have to be optimized. For 1D TiO₂ nanostructure, this confliction may be overcome by creating surface doping while leaving the center as a scattering-free conductive channel.

Another popular anionic doping element to TiO₂ is carbon, which has been extensively investigated from powders to NW structures. Di Valentin et al. calculated the electronic band structure of anatase TiO₂ with carbon doping by DFT simulation.²⁷³ They showed that under oxygen-deficient conditions, carbon substituting oxygen and oxygen vacancies are favored; under oxygen-rich conditions, interstitial carbon and substitutional carbon at Ti sites become popular. When carbon serves as a substitutional atom, based on their DFT calculation, it introduces two occupied and one empty localized states within the TiO₂ band gap, as shown in Figure 27a. These

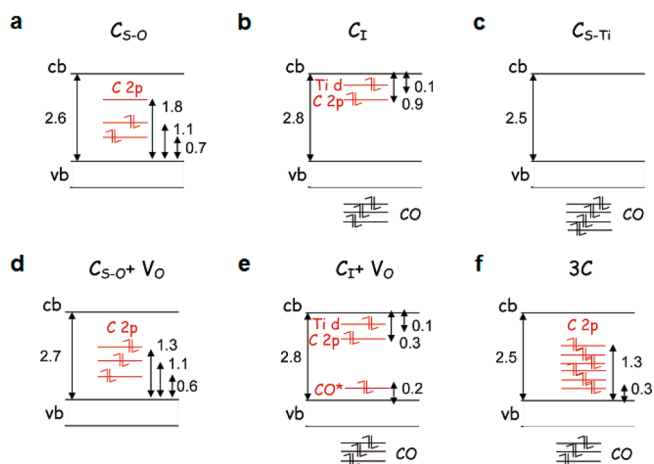


Figure 27. Energy levels of TiO₂ with (a) substitutional carbon doping (to replace oxygen atom), (b) interstitial carbon doping, (c) substitutional carbon doping (to replace Ti atom), (d) substitutional carbon doping (to replace oxygen) accompanied by an oxygen vacancy, (e) interstitial carbon doping accompanied by an oxygen vacancy, and (f) high carbon doping concentration. Reprinted with permission from ref 273. Copyright 2005, the American Chemical Society.

three states locate above the oxygen 2p level (the VBM) by 0.7, 1.1, and 1.8 eV, respectively. When carbon becomes an interstitial atom, electron transfer occurs from C–O bonding to Ti 3d states and two occupied states are formed (0.9 eV and 0.1 eV) below the CBM. The 0.1 eV level shares a similar character as the conduction band and the 0.9 eV level is more localized. Valentin et al. also revealed that oxygen vacancy is unavoidable in carbon-doped TiO₂. Figure 27b–f shows the electronic band structure of TiO₂ with oxygen vacancies involved. A general trend of the oxygen vacancy influence to the anatase TiO₂'s band structure is that higher concentration of oxygen vacancies would introduce more localized states within the band gap. It was concluded that the increased photoactivity in carbon-doped TiO₂ was mainly derived from the stoichiometric change of TiO₂ (i.e., the formation of oxygen vacancies) during doping process.

Besides nitrogen and carbon doping, sulfur, selenium and phosphorus have also been proposed as potential band gap narrowing dopants, which often lift up the valence band edge – a preferable case for maximizing solar energy conversion efficiency.^{272,274,275} However, the electronic and photocatalytic properties of TiO₂ NWs doped by these elements have been rarely studied, though their TiO₂ NP or powder counterparts have shown promising photoactivity.

Cationic dopants have also been investigated in order to enhance the photoactivity properties of TiO₂. These dopants include various 3d transition metals such as V, Cr, Mn, Fe, Co,

Nb, Mo, Rh, and Ni. By DFT simulation, Umeyashi et al. predicted that when TiO_2 is doped with V, Cr, Mn, Fe, or Co, an electron occupied level within the band gap will appear with localized characteristics.²⁷⁶ Heavier dopants move the localized levels to lower energy. For example, when Co was used for doping, the localized level sat slightly above the valence band. When a heavier element such as Ni was introduced to TiO_2 , the corresponding dopant levels were delocalized and participated in the formation of the valence band together with the O p and Ti 3d electrons, which was expected to significantly change the photo activity of TiO_2 . The density of states (DOS) of a number of transition metal-doped TiO_2 is shown in Figure 28.

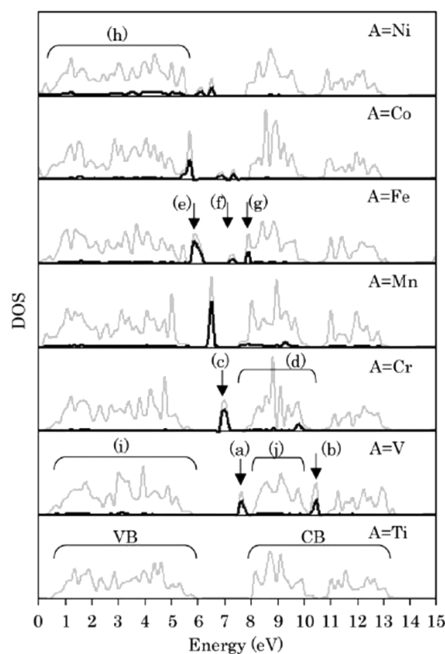


Figure 28. The DOS of the metal-doped TiO_2 . The gray solid lines are total DOS and the black solid lines are dopant's DOS. Reprinted with permission from ref 276. Copyright 2002, Elsevier.

It was predicted that a red shift in the band gap transition could be induced when TiO_2 was doped with V, Mn, or Fe, which was attributed to the charge-transfer between the d orbital electrons of the dopant and the conduction or valence band of TiO_2 itself.²⁷⁴ When Cr served as the dopant, the doping levels localized in the middle of the TiO_2 band gap, rendering a new visible light absorption transition.

Guided by the theoretical predictions, Liu et al. recently developed a general strategy to synthesize TiO_2 NWs with a variety of transition metal dopants including V, Cr, Mn, Fe, Co, Nb, Mo, and Rh for the purpose of tuning their optical, electrical and catalytic properties.²⁷⁷ It was found that by introducing any of these dopants into TiO_2 rutile lattice, the overpotential for the oxygen evolution reaction was drastically reduced. For example, 2% Mn-doped TiO_2 NW had an overpotential of 0.488 V, which was 28% lower than pristine TiO_2 NWs. The reduction of oxygen evolution reaction overpotential was believed to be due to the strong interaction among the absorbed species on the doped-NW surfaces. Compared to anionic doping, the PEC performance or the solar energy conversion of transition metal-doped TiO_2 NWs are much less studied.

Monodoping such as nitrogen doping can reduce the band gap of TiO_2 effectively, but it was found experimentally that the electron–hole recombination rate increased catastrophically due to the presence of the partially occupied impurity bands. Transition metal doping experienced the same problem as well, where the d orbital localized levels significantly impeded the charge separation. To solve this problem, a passivated codoping method was proposed by Gai et al.²⁷² They suggested that the charge compensated donor–acceptor pairs such as (N+V), (Nb+N), (Cr+C), and (Mo+C) could help to passivate the recombination centers introduced in TiO_2 by monodopant. The principle was that the electrons on the donor levels annihilate the same amount of holes on the acceptor levels. With this guideline, they proposed that a combination of Mo+C codoping would be ideal for developing TiO_2 -based PEC photoanodes since it does not affect much of the CBM but increases VBM by 0.85 eV (Figure 29a), which is

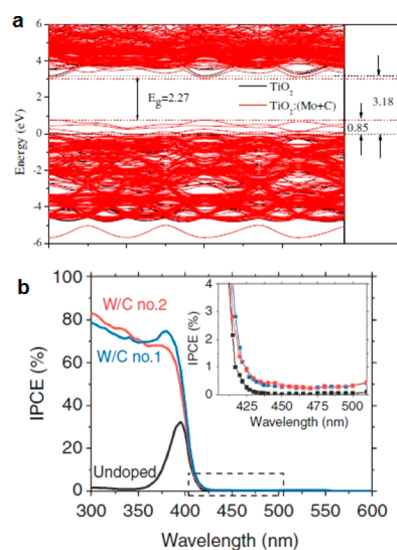


Figure 29. (a) Band structure of TiO_2 codoped by Mo+C. Reprinted with permission from ref 272. Copyright 2009, The American Physical Society. (b) Comparison of IPCEs of W/C codoped and undoped TiO_2 NWs. Reprinted with permission from ref 183. Copyright 2013, the Nature Publishing Group.

thermodynamically preferable in enabling spontaneous water splitting reaction. Cho et al. performed the codoping of W+C into TiO_2 NWs by a sequentially annealing W-precursor-coated TiO_2 NWs in flame and carbon monoxide gas.¹⁸³ They found that the codoping TiO_2 NWs indeed exhibited a much higher saturation photocurrent density and high quantum efficiency in the UV region, which was attributed to the reduced recombination rate and increased charge mobility (Figure 29b).

In addition to these heavy dopants, hydrogen, an omnipresent specie, was recently introduced to modify the electronic property of TiO_2 NPs and NWs.^{21,278} Though the underlying mechanism is still under debate, compared to pristine TiO_2 , hydrogen-treated TiO_2 NWs have demonstrated substantially increased quantum efficiency in UV illumination region for PEC water splitting applications. Wang et al. reported the application of hydrogen-treated TiO_2 NW arrays as PEC photoanodes for water splitting, which yielded a photocurrent density of $\sim 1.97 \text{ mA/cm}^2$ (-0.6 V vs Ag/AgCl, in 1 M NaOH solution) under the illumination of simulated solar light.²⁷⁸ It corresponded to a solar energy conversion

efficiency of $\sim 1.63\%$, as shown in Figure 30a. Such a high efficiency was attributed to the increased donor density of TiO_2

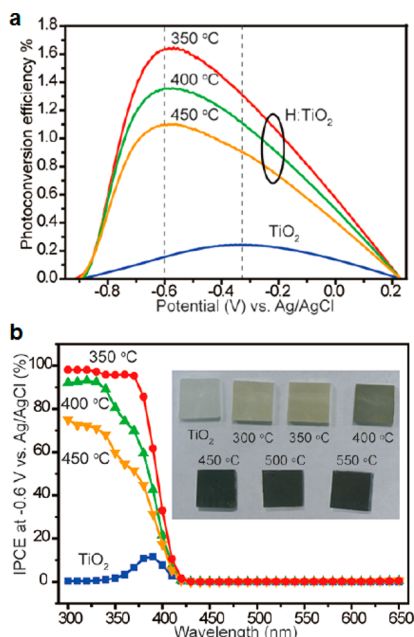


Figure 30. Photoconversion efficiencies (a) and IPCE spectra (b) of pristine TiO_2 and H: TiO_2 NWs prepared at 350, 400, and 450 °C. Inset is a photo of pristine TiO_2 and H: TiO_2 NW samples annealed in hydrogen at various temperatures. Reprinted with permission from ref 278. Copyright 2011, American Chemical Society.

NWs via creating a high density of oxygen vacancies from hydrogen treatment. The IPCE curves in Figure 30b revealed that hydrogen treat has successfully enhanced the efficiency in the UV region. In addition to hydrogen, Shi et al. found Cl impurities may also contribute similar band gap narrowing effect to TiO_2 NRs.⁷⁴ Through a nonstoichiometry deposition condition, dangling Ti–Cl and Ti–OH groups were introduced inside anatase TiO_2 NRs, resulting in visible light absorption and PEC activity as shown in Figure 31. Inset picture shows the defective and black TiO_2 NR arrays.

5.1.3. TiO_2 NW Heterostructures. Another strategy to effectively utilize the good catalytic property but circumvent the poor charge transport property of TiO_2 is to create a heterostructure based on the 1D morphology. The most common approach is to deposit TiO_2 shell on conductive NW core structures, where TiO_2 serves as the reaction sites and the

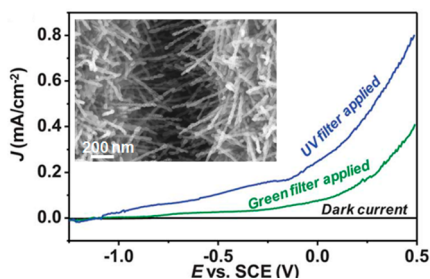


Figure 31. $J-E$ curve of TiO_2 -Si NW PEC photoanode under 100 mW cm^{-2} solar simulator illumination with UV filter and green light filter applied. Inset is an SEM image of the hierarchical TiO_2 -Si NW structure. Reprinted with permission from ref 74. Copyright 2012, The Royal Society of Chemistry.

charges transport through the core material. Hwang et al. synthesized a Si/ TiO_2 core-shell NW heterostructure and demonstrated a promising application potential as PEC photoanodes.¹²¹ The NW heterostructure achieved 2.5 times higher photocurrent compared to planar photoanode made from the same materials due to the enlargement of surface area, higher charge conductivity and better light absorption. They found that n-Si/ TiO_2 had a favorable band alignment, resulting in higher photocurrent and open-circuit voltage.

Although the NW morphology could enlarge the surface area density, it was still not comparable to that of packed NP films. Three-dimensional (3D) NW architectures are ideal to maximize the surface area density and meanwhile retain good charge transport property from the NW morphology.²⁷⁹ Shi et al. reported a novel 3D high-density NW heterostructure for PEC photoanodes.¹¹⁹ The 3D NW architecture is schematically shown in Figure 32a. Vertically aligned heavily doped Si NW

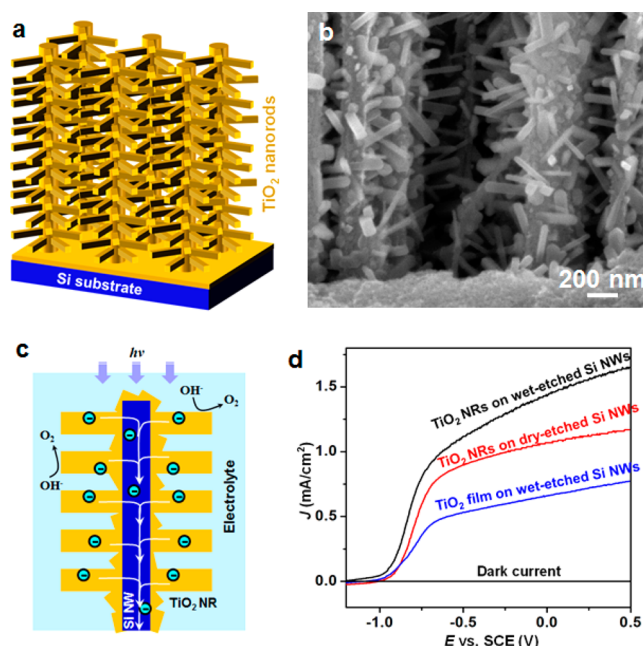


Figure 32. (a) Schematic structure of treelike TiO_2 NR-Si NW 3D architectures. (b) SEM image of the hierarchical NW structure showing dense and uniform coverage of TiO_2 NRs. (c) Schematic illustration of employing 3D TiO_2 NR-Si NW architectures for PEC water splitting. (d) $J-E$ curves of different TiO_2 -Si NW configurations demonstrating enhanced PEC performance by introducing high density TiO_2 NR branches. Reprinted with permission from ref 119. Copyright 2011, American Chemical Society.

arrays were used as the backbones and high density anatase TiO_2 NRs were uniformly grown around the Si NWs. An additional thin film of anatase TiO_2 was coated on the NR-NW heterostructure to completely cover Si NW surfaces. A typical image of the 3D NW architecture is shown in Figure 32b. When this heterogeneous structure was used as a PEC anode for water splitting, photocatalyzed H_2O oxidation reactions would only occur on the TiO_2 surfaces. In principle, the photogenerated electrons should quickly be transported through the Si NW backbone and reach the counter electrode with minimal losses owing to the high conductivity of Si NWs and isolation from electrolyte, as shown in Figure 32c.^{121,280} The very large surface area provided by the TiO_2 NR arrays together with the high-speed electron transport channels

provided by the Si NWs are promising features that could lead to a significant improvement of PEC efficiency. A typical plot of photocurrent density versus bias potential is shown in Figure 32d. The $J-E$ curve exhibited a fill factor of 0.54 and short circuit current density (J_{SC}) of 1.14 mA/cm², which demonstrated good charge transport properties and interfacial reaction chemistries of these 3D TiO₂ NR-Si NW anodes. The highest efficiency (2.1%) was identified from the 20- μ m Si NW arrays with \sim 200 nm TiO₂ NRs and a \sim 25 nm TiO₂ overcoating. This value was three times higher than that of TiO₂ film-Si NWs core-shell structure. This comparison suggested that the 3D NW architecture is likely superior to straight NW arrays for PEC electrode design.

A similar TiO₂ NR-Si NW heterostructure was also developed by Liu et al.¹²⁰ As schematically shown in Figure 33a, the NW heterostructure was a fully integrated n-TiO₂/p-Si

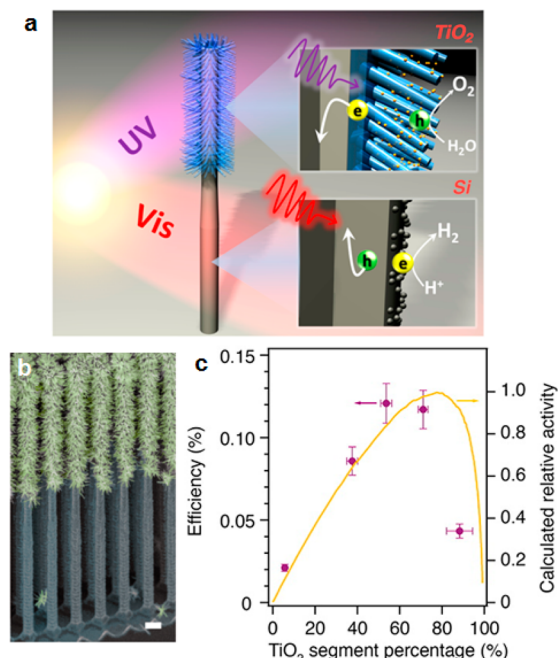


Figure 33. (a) Schematic of a heterogeneous n-type TiO₂ NR (blue) – p-type Si NW (gray) structure as a full PEC cell. The two insets show the oxidation and reduction reactions on TiO₂ NR and Si NW surfaces, respectively. (b) False-colored SEM image of the TiO₂–Si NW heterostructure. (c) Measured energy conversion efficiency (left axis) and estimated normalized relative photoactivity (right axis) of various NW heterostructures with different percentages of TiO₂ NR coverage. Reprinted with permission from ref 120. Copyright 2013, the American Chemical Society.

system that mimicked natural photosynthesis to generate O₂ and H₂ separately via the “Z-scheme”.²⁸¹ Upon illumination, TiO₂ NRs absorbed the UV light and oxidized the water producing O₂; meanwhile, Si NWs absorbed the visible light and reduced the water producing H₂ (inset of Figure 33a). Extra holes (from Si) and electrons (from TiO₂) recombined at the TiO₂/Si interface and thus completed the circuit. Geometry optimization showed that when TiO₂ NRs covered 50–80% of the length of Si NW (Figure 33b), the highest solar energy conversion efficiency of 0.12% was achieved under simulated sunlight (Figure 33c). This efficiency was comparable to that of photosynthesis in plants.

The other configuration of NW heterostructure is to use TiO₂ NWs as the core material and coat/decorate the surface with functional materials, including QDs, graphene, noble metals, metal oxides, and even molecules.^{282–284} This strategy is particularly useful for improving the catalytic activity of TiO₂ NWs. Ng et al. synthesized a unique TiO₂ NW morphology whose surface was decorated with SrTiO₃ nanocube precipitates.²⁸⁵ The photocatalytic water splitting efficiency of such as-prepared heterostructures was 4.9 times higher than that of bare TiO₂ NWs and 2.1 times higher than that of SrTiO₃. The high performance was attributed to efficient separation of photogenerated charges and negative redox potential shift of the Fermi level in TiO₂. By covering TiO₂ NRs with graphene oxide (GO), Liu et al. discovered a significantly improved photocatalytic activity for the degradation of methylene blue (MB).²⁸⁶ They suggested that the large improvement was a result of reduced charge recombination and effective absorption of MB on GO. The enhanced charge transfer from TiO₂ to GO and MB absorption on GO were confirmed by significant photoluminescence quenching of TiO₂ and UV–vis spectra, respectively. Pu et al. found that Au-decorated TiO₂ NWs demonstrated remarkably enhanced PEC performance in water oxidation within a broad wavelength range from 300 to 800 nm.²⁸⁷ Three types of Au nanomorphologies including NPs, NRs, and a mixture of NPs and NRs were incorporated onto TiO₂ surfaces. Slightly enhanced photoactivity in both UV and visible light regions was observed from Au NPs-decorated TiO₂ electrode; while Au NRs decoration showed remarkably increased photoactivity in the UV regime. By decorating the TiO₂ NWs with a mixture of NPs and NRs, the photoactivity was significantly enhanced in the entire UV–visible region. The enhanced photoactivity was attributed to the increased optical absorption of TiO₂ associated with the excitation of surface plasmonic resonance of Au nanostructures with appropriate surface passivation. Dinh et al. uniformly decorated Ag clusters to the surfaces of hydrophobic surfactant-capped TiO₂ NRs by photodeposition.²⁸⁸ Owing to the conformal dispersion of Ag clusters, this heterostructure showed a considerably higher photocatalytic activity for the decomposition of methylene blue dye compared to P25 TiO₂ NPs coated with Ag NPs. Yang et al. synthesized similar Ag-TiO₂ NR heterostructures with controllable Ag NR density and size by in situ reduction of silver acetate on TiO₂ NRs.²⁸⁹ The ultrasmall size of Ag NPs (\sim 2 nm) introduced an extremely larger surface area and more reactive sites, resulting in enhanced catalytic property.

It has also been found that the PEC performance of TiO₂ NWs could be improved by coating the surface with another epitaxial layer of TiO₂.¹⁰⁴ Hwang et al. used ALD technique to deposit rutile TiO₂ epitaxial film on rutile TiO₂ NWs grown by a hydrothermal technique. The ALD coating enhanced the photocatalytic activity by 1.5 times on 1.8 μ m-long TiO₂ NW photoanodes, reaching a current density of 1.1 mA/cm² (1.5 V vs RHE). More significantly, the enhancement of PEC performance became more significant for longer NWs, suggesting ALD coating improved the charge collection efficiency from TiO₂ NWs due to the passivation of surface states. Therefore, this could be a viable approach to more effective utilization of the length and surface area merits offered by the NW morphology. Yang et al. reported an effective photocatalyst based on TiO₂(B) NWs covered by anatase TiO₂ shells.²⁹⁰ This TiO₂ core/shell structure demonstrated superior photocatalytic property in degrading sulforhodamine B under UV light compared to either pure-phased NWs or mechanical

mixtures of anatase and TiO₂(B) NWs. Three unique features of this structure were suggested. First, the build-in potential at the core–shell interface is favorable for photogenerated charge separation. Second, the well-matched interface has very low trap concentration, and thus reduces the recombination loss. The coherent interface crystal structure between TiO₂(B) and anatase TiO₂ was suggested to be a general configuration in biphasic TiO₂ by Liu et al.²⁹¹ Third, surfaces of the anatase shell have a strong capability of absorbing the reactant molecules. Liu et al. synthesized a similar heterostructure with TiO₂(B) core and anatase TiO₂ shell aiming at facilitating charge separation through build-in potential.²⁹² They revealed that the TiO₂(B) NWs with a partially covered anatase shell exhibited higher photocatalytic activity than complete anatase covered TiO₂(B) NWs since electrons in the anatase shell and holes in the TiO₂(B) core both needed to participate in the degradation reactions.

5.2. 1D TiO₂ Nanostructures in Photovoltaics

TiO₂, owing to its stable chemistry and appropriate electronic band structure, has been widely used in many types of photovoltaic systems as the charge collector. Its 1D morphologies such as NW arrays have exhibited enhanced performance owing to improved carrier collection, reduced optical reflection, and efficient absorption. Although limitations still exist in terms of charge recombination, surface scattering and interface imperfection, understanding 1D charge transport properties and exploring novel configurations of TiO₂ NWs for efficient solar energy absorption, conversion and charge collection remain active research areas in novel photovoltaic system developments.

5.2.1. Dye-Sensitized Solar Cells. Dye-sensitized solar cell (DSSC) is a promising photovoltaic system that offers low fabrication cost and reasonably high efficiency and stability.²⁹³ Recently, a record solar energy conversion efficiency of 15% has been achieved by Burschka et al. based on a perovskite sensitizer and mesoporous TiO₂ film charge collector.¹⁷ Efforts to achieve high efficiency DSC mainly focus on the improvements of photoanode, dye and the redox species as well as counter electrode. Typical anode of DSSCs is made from oxide NPs (mostly TiO₂). Although packed NPs can provide very large surface roughness factor (defined as the total surface area per unit substrate area), improvement of efficiency is limited by the poor electronic transport property through the NP network.^{294–299} Substantial progresses on addressing this challenge have been demonstrated on both single-crystalline TiO₂ NWs and 1D TiO₂ nanocomposites.^{300–303}

Electronic Property Enhancement. The superior charge transport property of 1D TiO₂ nanostructures compared to NPs has been revealed by various research groups. Kang et al. analyzed the electron transport property and electron lifetime in anatase TiO₂ NRs using stepped light-induced transient measurements of photocurrent and voltage (SLIM-PCV) method.²⁹⁸ Compared to NP films, electron diffusion coefficient was improved slightly by the NR morphology (Figure 34a); while significant enhancement of electron lifetime was found in TiO₂ NRs (Figure 34b). This enhancement was attributed to the largely reduced grain boundaries in single-crystalline NR structures, which were favorable for eliminating electron trapping and avoiding charge recombination, resulting in increased electron diffusion length. Due to the superior charge transport property, the TiO₂ NR electrode yielded a better DSSC performance (a Voc of 0.68 V, a Jsc of 15.3 mA/

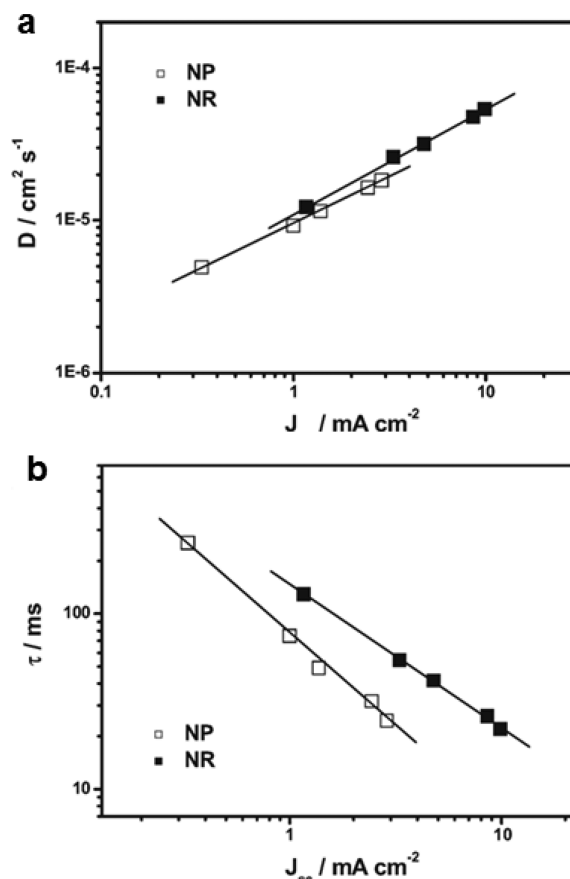


Figure 34. Electron diffusion coefficients (a) and electron lifetimes (b) characteristics of NP- and NR-based DSSCs under 635 nm laser illumination. Reprinted with permission from ref 298. Copyright 2008, Wiley-VCH.

cm^2 , a fill factor of 0.6, and an efficiency of 6.2%) than a TiO₂ NP-based electrode (a Voc of 0.63 V, a Jsc of 10.9 mA/cm², a fill factor of 0.63, and an efficiency of 4.3%) that had the same number of absorbed dye molecules. The 1D morphology-related electron diffusion in TiO₂ NRs was further investigated by Lee et al.²⁹⁹ They applied intensity modulation photocurrent spectroscopy (IMPS) and intensity modulation photovoltage spectroscopy (IMVS) to investigate the charge transport characteristics in TiO₂-based DSSCs and identified an eight-time longer electron lifetime in the NR configuration compared to NP electrodes. As a result, higher solar energy conversion efficiency (9.00%) was obtained from the TiO₂ NR DSSCs (vs 6.17% of NP DSSCs with the same film thickness).

Feng et al. found that the electron diffusion coefficient of single crystalline rutile TiO₂ NWs was twice as high as that of single crystalline rutile TiO₂ NPs under the same illumination condition.^{114,304} They also revealed that sub-bandgap defect states density of NW-based DSSC was significantly lower than NP-based DSSCs. Wang et al. applied rutile TiO₂ NR arrays to solid-state DSSCs with C106 dye and 2,2',7,7'-tetrakis-(*N,N*-dipmethoxyphenylamine) 9,9'-spirobifluorene (spiro-MeO-TAD) as the organic hole-transporting material (HTM).³⁰⁵ The J - V curves of these DSSCs are shown in Figure 35a, which revealed the efficiency under full sun light intensity was 2.9%. However, their transient photovoltage decay characteristics, as shown in Figure 35b,c, suggested that the recombination time of photogenerated electrons and holes in rutile TiO₂ NR DSSC was shorter than that in a sintered TiO₂ NP film under an

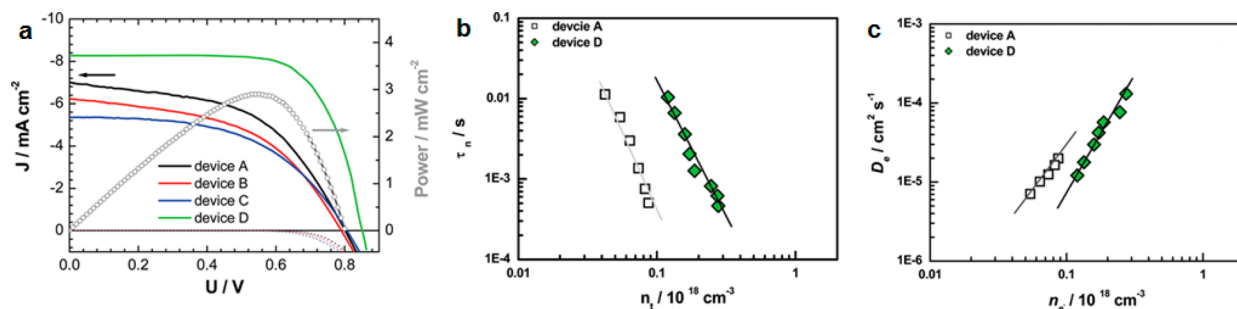


Figure 35. (a) J - V curves of solid state DSSC using TiO₂ NRs with different lengths (A-2.1 μ m, B-2.68 μ m, and C-3.65 μ m) and a 1.9 μ m-thick TiO₂ NP film (D) as the photoanodes under AM 1.5G illumination with full sun intensity. (b) Charge recombination lifetime plots of device A and device D. (c) Electron diffusion coefficients characteristics of device A and device D. Reprinted with permission from ref 305. Copyright 2012, the American Chemical Society.

identical charge density. This result is in contrast to the conclusion from Kang and Lee as we discussed earlier.^{298,299} This controversy might be a result of the significant recombination or back reactions of injected electrons on rutile TiO₂ surfaces, which canceled out the 1D morphology contributions.^{306,307}

NW Morphology Investigations. Compared to randomly oriented NWs, vertically aligned NW arrays grown on transparent conductive substrates are expected to exhibit high performance because every single NW is in direct contact with the electrode and no “dead ends” exist in such an electrode configuration. Liu et al. synthesized a vertically aligned single-crystalline rutile TiO₂ NW array on transparent conductive fluorine-doped tin oxide (FTO) substrate using hydrothermal method (Figure 36a).⁹ The DSSC built on a 4- μ m long TiO₂ NW array gave a short circuit current density of \sim 6.05 mA/cm², an open circuit voltage of \sim 0.71 V, a fill factor of 0.7 and 3.0% efficiency (Figure 36b). Kumar et al. synthesized similar single-crystalline rutile TiO₂ NWs on multiple substrates including FTO, ITO and silicon.³⁰⁸ Similar DSC performance

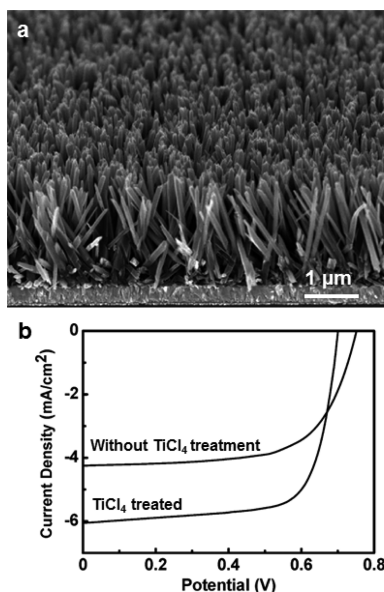


Figure 36. (a) Tilted cross-sectional SEM image of oriented rutile TiO₂ NRs grown on a FTO substrate. (b) J - V curves of a DSSC device fabricated using a 4 μ m-long rutile TiO₂ NR film without and with TiCl₄ treatment. Reprinted with permission from ref 9. Copyright 2009, the American Chemical Society.

(2.9% \pm 0.2%) was obtained for the vertically aligned TiO₂ NW array on FTO substrates. Recently, a record high efficiency (9.4%) of rutile TiO₂ NR based DSSCs was obtained by Kim et al. utilizing CH₃NH₃PbI₃ sensitizer, which is a halide organic-inorganic hybrid perovskite structure with superior light harvesting property and remarkable charge diffusion length (\sim 100 nm).³⁰⁹ Cross-section of the device is shown on Figure 37a, where photogenerated holes transport to the gold

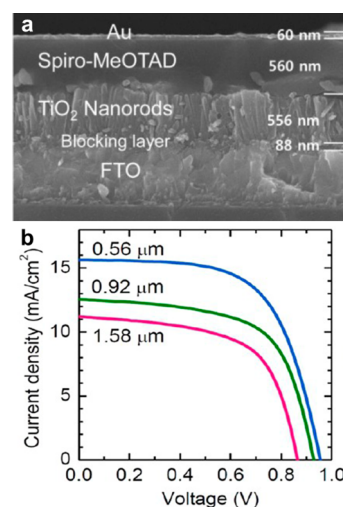


Figure 37. (a) Cross-section SEM image of a CH₃NH₃PbI₃ sensitized rutile TiO₂ NR/spiro-MeOTAD solar cell. (b) J - V curve of solar cells with various TiO₂ NR lengths. Reprinted with permission from ref 309. Copyright 2013, the American Chemical Society.

electrode through the hole transporting material (Spiro-MeOTAD) and electrons are collected by the TiO₂ NRs. The DSSC exhibited a J_{SC} of 15.6 mA/cm², a V_{OC} of 955 mV, and a fill factor of 0.63 under simulated AM 1.5G illumination. It was found that the photovoltaic performance was largely dependent on the length of TiO₂ NRs, where both J_{SC} and V_{OC} dropped with increasing the NR length (Figure 37b). Because the recombination properties were found to be almost independent of the NR length by impedance spectroscopy characterization, the V_{OC} reduction was attributed to the charge generation efficiency rather than recombination kinetics.

DSSCs made from aligned TiO₂ NWs yet show appreciable performance enhancement compared to random NWs or NPs, although the aligned NW morphology has been generally believed as the optimal geometry for electrode design. One critical limitation of aligned NW arrays is their small surface

area density that limits the amount of dye loading, e.g., the roughness factor of dense NW arrays is typically 1 order of magnitude lower than that of packed NP films.³⁰⁵ Increasing the NW's length and surface roughness are two general strategies to enlarge the surface area density. Lv et al. developed a highly ordered rutile TiO₂ NW array via the hydrothermal method. Following chemical etching treatment split the original TiO₂ NWs into bundles of smaller NWs (Figure 38a). DSSCs

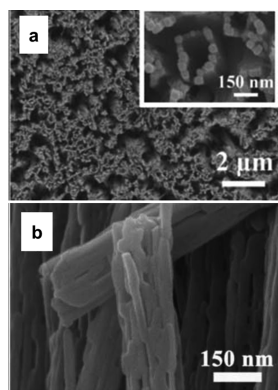


Figure 38. (a) SEM images of TiO₂ NR array after etching, inset is the top view with higher magnification showing the reduced diameter of NR after splitting. (b) SEM image of porous TiO₂ NRs. Reprinted with permission from refs 310 and 311. Copyright 2013, Royal Society of Chemistry.

made from this structure exhibited an efficiency of 5.94%.³¹⁰ To further increase the surface area, they improved the NW length up to $\sim 30 \mu\text{m}$ and etched the NWs into a porous structure by secondary hydrothermal treatments (Figure 38b).³¹¹ DSSCs made from such porous TiO₂ NW arrays yielded an efficiency of 7.91%. Wang et al. synthesized single crystalline rutile TiO₂ NW arrays with controllable length in the range of 6–46 μm . The extremely long NWs resulted in an enhanced surface area up to $95 \text{ m}^2 \text{ g}^{-1}$ and an optimal overall DSSC efficiency of 5.13% was identified from the TiO₂ NW electrode with 9.6 μm in length.³⁰⁵ However, because this strategy may introduce more electrical loss due to charge trapping or recombination, their efficiencies still remain at a moderate level. In order to improve the efficiency, it is equally important to achieve high-speed and low loss charge transport in the electrode configuration.

As discussed earlier in this article, 3D NW architectures are considered as a promising solution for addressing the surface area and charge transport challenges simultaneously. Sauvage et al. reported a 3D single-crystalline anatase TiO₂ nanotree structure for DSSC photoanode (Figure 39a).²⁰⁷ This architecture offered more than 1 order of magnitude faster electron transport than that of mesoporous TiO₂ films composed of 20 nm nanocrystal, as well as a high roughness factor and significant light scattering. They found this morphology was able to reduce charge recombination and enhance mass flow control of tri-iodide when used in the ionic liquid electrolyte. Thus, it reached a maximum solar energy conversion efficiency of 4.9% with the C101 dye and 7 μm thick NW film. The corresponding J – V curves under different light intensity are shown in Figure 39b. Roh et al. created an anatase pine tree-like TiO₂ nanostructure that consisted of vertically aligned nanotube stems and dense NR branches via one step hydrothermal reaction.³¹² The porous branch structure and long nanotube stems (19 μm) significantly

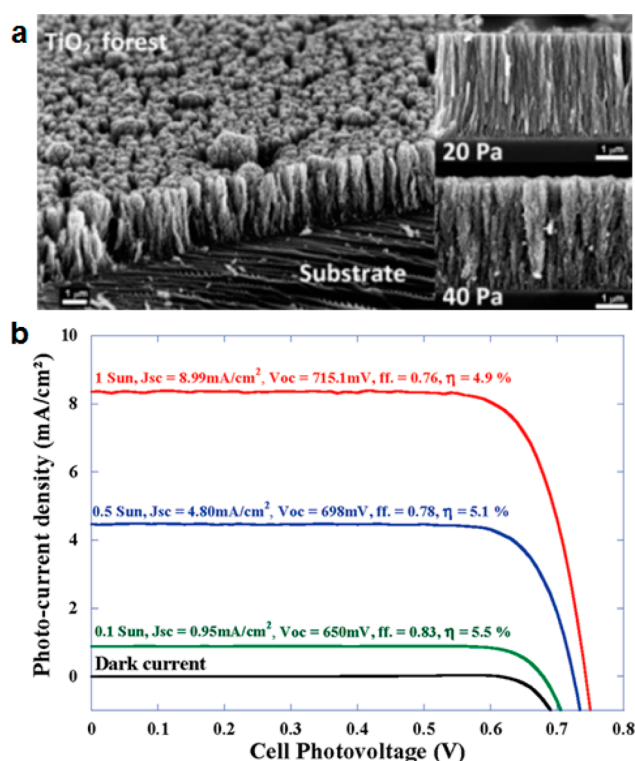


Figure 39. (a) SEM image of a PLD TiO₂ NR film for DSSC fabrication. Insets are the cross-sectional images. (b) J – V curves of the DSSC made from a 7 μm -long TiO₂ NR film measured under different AM 1.5G light intensities. Reprinted with permission from ref 207. Copyright 2010, the American Chemical Society.

enlarged the surface area density. Solid-state DSSC using N719 dye was assembled based on this structure and reached an impressive efficiency of 8.0%. Liao et al. synthesized partially aligned single-crystalline anatase TiO₂ NW arrays with short TiO₂ NR branches through a two-step hydrothermal method.³¹³ DSSCs were fabricated using the hierarchical TiO₂ nanostructures with either rigid (Pt/FTO) or flexible (PEDOT/ITO-PET) counter electrode. This hierarchical TiO₂ electrode yielded a significant efficiency improvement (4.51%) compared to straight TiO₂ NW arrays (3.12%). Kim et al. grafted anatase TiO₂ NRs onto various anatase TiO₂ scaffolds including NWs, nanospheres, and nanosheets by a facile sol-gel approach.³¹⁴ One of the hierarchical TiO₂ nanostructures (called chestnut bur) was used to fabricate DSSC and boosted the efficiency from 7.16% to 9.09% compared to TiO₂ nanosphere-based DSSCs. The enhancements of efficiency in such heterostructures were attributed to the large quantity of dye loading, favorable light scattering, and comparable electron transport property.

The correlation between the NW morphology and the photovoltaic performance of DSSCs was systematically studied by Cozzoli et al. using morphology-controlled TiO₂ NW and branch structures.¹⁵² The TiO₂ NW network reached an efficiency of 6.2% when first assembled into DSSC. This nanostructure was further proved to be a favorable platform for fabricating DSSC electrode by Marco et al.³¹⁵ Charge trapping and recombination were found to be effectively reduced in such TiO₂ nanostructures, leading to an efficiency of 7.8% (from a 9 μm thick TiO₂ electrode film). Agosta et al. investigated the relationship between DSSC performance and TiO₂ nanostructure from three groups of anatase TiO₂ NRs (aspect ratios of 4,

8, and 16) and two sets of branched anatase TiO₂ frameworks (braid-like and sheaf-like).³¹⁶ By analyzing the chemical capacitance and charge transfer resistance of these TiO₂-based electrodes, braid-like branched framework was found to be the most advantageous structure to minimize the interface charge recombination; while linear NRs with high aspect ratios exhibited a notable downshift of conduction band edge, which is favorable for the injection of photogenerated electrons from the LUMO of dye molecules. Marco et al. achieved a remarkable solar cell efficiency (10.26%) by using a mesoporous multilayered electrode composed of three breeds of the anatase TiO₂ NRs.³¹⁷ The significantly enhanced efficiency was attributed to the multilayer morphology, which was favorable for light harvesting but had minimal impacts to charge transport.

1D TiO₂ Heterostructures. 1D TiO₂ nanostructures also have been integrated with a variety of other nanomaterials, such as TiO₂ NPs, carbon fiber, ZnO NWs and doping elements, to improve the surface, charge transport, and light absorption properties for gaining on the DSSC performance.^{16,168,318–325} Tan et al. fabricated a heterostructure by filling anatase TiO₂ NPs into the spaces between single-crystalline anatase TiO₂ NW arrays for DSSC photoanode.³²² They compared the performance of three different mixing ratios (5, 20, and 77 wt % of NW) together with pure NP electrodes. It was found that the 20 wt %-NW mixture could boost the DSSC efficiency from 6.7% to 8.6%. Despite of the higher V_{OC} and larger fill factor, efficiency of 77 wt % sample was greatly hampered by the low current density caused by reduced specific surface areas. The enhancement was attributed to the long electron diffusion length from the NW component and the considerably large surface area from the NP component. A similar NP-NW heterostructure was created by Wu et al., who designed a double layered DSSC which had a layer of TiO₂ NPs resting on top of an anatase TiO₂ NW array, as schematically shown in the inset of Figure 40a.³²³ Figure 40a illustrates the *J*–*V* characteristics of DSSC fabricated with various NP film thicknesses and NW lengths. The 13 μm NW and 18 μm NP heterostructure yielded the highest solar energy conversion efficiency of 7.92%.

Incorporating highly conductive 1D carbon nanomaterials with 1D TiO₂ nanostructures is a promising strategy to improve the electron transport property of DSSC electrodes by increasing the electron mobility and extending the electron lifetime. Yang et al. introduced multiwalled carbon nanotubes (MWCNTs) inside the TiO₂ NR arrays with various weight ratios (from 0.05% to 0.15%) and investigated corresponding DSSC performance as shown in Figure 40b.³²⁵ This TiO₂ NR-MWCNT core-shell structure realized a considerable DSSC performance gain (an efficiency of 10.24%, a J_{sc} of 18.53 mA/cm² and a FF of 74% for 0.1% MWCNT concentration samples). The enhancement was believed to be a result of the optimized electrical contact and minimized electron loss due to MWCNT incorporation. Guo et al. reported a tube-shaped DSSC using TiO₂ NR-coated carbon fibers (CFs) as the photoanode.³²⁰ As shown in Figure 41a,b, TiO₂ NRs were uniformly and densely distributed on the carbon fibers. The CF/TiO₂ NR-based 3D DSSC solar cell configuration is schematically shown in Figure 41c. Dense TiO₂ NRs rooting on the surface of conductive CFs ensured the most effective path for charge transport. Intertwining the NR-coated CFs created a 3D structure with very large surface area. Therefore, the photocurrent was nearly doubled compared to simple TiO₂ NR

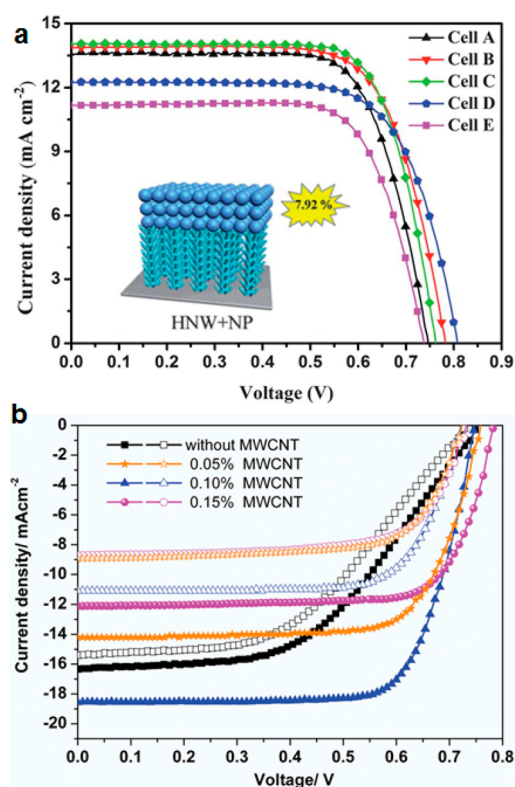


Figure 40. (a) *J*–*V* characteristics of DSSCs assembled from the TiO₂ NWs and NPs hybrid structures with various NP film thicknesses (cell A: 6.0 μm, cell B: 12.0 μm, cell C: 18.0 μm, cell D: 24.0 μm, cell E only had a 31 μm-thick TiO₂ NP component). Inset is the schematic illustration of TiO₂ NW/NP heterogeneous configuration. Reprinted with permission from ref 329. Copyright 2012, the Royal Society of Chemistry. (b) *J*–*V* curves of various photoanodes with different MWCNT percentages and film thicknesses (hollow symbols represent 6.6 ± 0.7 μm film thickness, solid symbols represent 14.3 ± 0.3 μm film thickness). Reprinted with permission from ref 325. Copyright 2013, Wiley-VCH.

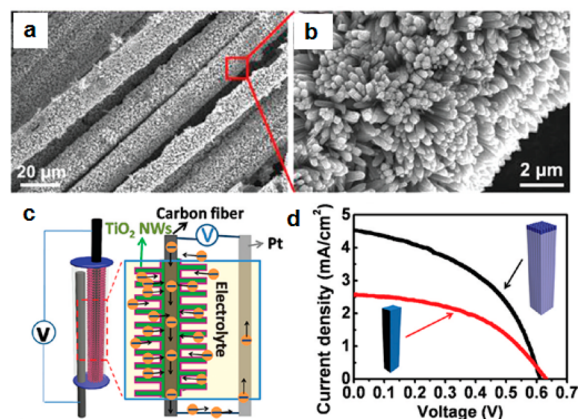


Figure 41. (a, b) SEM images of TiO₂ NR arrays grown on carbon fibers (CFs) showing the dense and uniform TiO₂ NR coating. (c) Schematic configuration of the CF/TiO₂ NR array-based 3D DSSC. (d) *J*–*V* curves of DSSCs made from TiO₂ NR arrays and CF/TiO₂ NR arrays. Reprinted with permission from ref 320. Copyright 2012, the American Chemical Society.

arrays, as shown in Figure 41d. Though its energy conversion efficiency (1.28%) is not competitive to state of the art mesoporous TiO₂ DSSCs, this novel TiO₂ NR-CF electrode

opened a new route toward flexible and integratable fibrous solar cells.

ZnO is a promising transparent conductive oxide (TCO) material. Therefore, single-crystalline ZnO NWs have also been investigated in TiO₂-based DSSCs as the charge conductor. Law et al. developed a core-shell DSSC photoanode by coating ZnO NWs with a thin layer of anatase TiO₂.¹⁴ The core-shell structure could provide a radial surface field along the NW's cross-section, resulting in reduced charge recombination. They found TiO₂ shells with thicknesses of 10–25 nm substantially raised the V_{OC} and the fill factor with a little decay of photocurrent compared to pure ZnO NW-based DSSCs. The optimal ZnO/TiO₂ photoanode yielded a solar energy conversion efficiency of 2.25% under 100 mW/cm² AM 1.5 simulated sunlight. Xu et al. reported highly efficient DSSCs using multiple layers of TiO₂ film-coated ZnO NWs as the photoanode.^{323,324} The multilayer ZnO NW electrode was 40–50 μ m thick, consisting four layers of vertically aligned ZnO NW arrays that were prepared by alternative cycles of NW growth and monolayer coating.³²⁴ As shown on Figure 42a, the

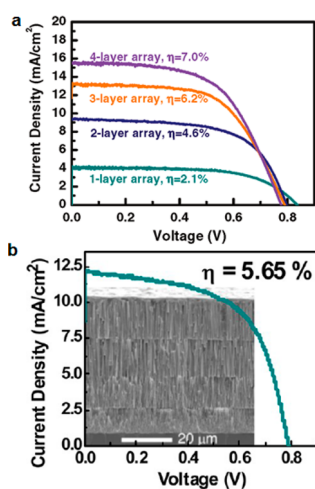


Figure 42. (a) J - V characteristics of DSSCs using multilayer TiO₂ coated ZnO NW arrays. Reprinted with permission from ref 324. Copyright 2011, American Chemical Society. (b) J - V characteristic of a solid state DSSC fabricated by filling a four-layer TiO₂-coated ZnO NW array. Inset shows the four-layer TiO₂-coated ZnO NW array structure after solid electrolyte filling. Reprinted with permission from ref 323. Copyright 2012, the American Chemical Society.

DSSC efficiency was raised from 2.1% to 7.0% with the increase of NW layers from 1 to 4 due to the internal surface area enlargement.³²⁴ The same structure was also implemented in solid-state DSSC by using spiro-OMeTAD as the hole transporting material (HTM). A four-layer TiO₂-ZnO NW configuration (shown in the inset of Figure 42b) achieved a high efficiency of 5.65%.³²³ The corresponding J - V curve is shown in Figure 42b.

5.2.2. Polymer-Based Solar Cells. Polymer-based solar cell (PSC) is a promising alternative photovoltaic technique that is low cost, flexible, and lightweight.^{326–328} Recently, He et al. demonstrated the highest certified efficiency of 9.2% utilizing an inverted structure which contained a blend of [6,6]-phenyl C₇₁-butyric acid methyl ester (PC₇₁BM) and low band gap semiconducting polymer thieno [3,4-*b*] thiophene/benzodithiophene (PTB7) as the photoactive layer, and an alcohol/water-soluble conjugated polymer as the ITO surface modifier.³²⁹

Principles and current progresses of PSC have been discussed in details in recent reviews.^{330,331} A typical PSC consists of a photoactive polymer as the electron donor, fullerene as the acceptor, and transparent conductive electrodes. Upon illumination, excitons are generated and separated at the acceptor/donor heterojunction. The offset between the highest occupied molecular orbital (HOMO) of donor and the lowest unoccupied molecular orbital (LUMO) of acceptor provides the primary driving force to overcome the exciton binding energy and determines the V_{OC} of PSC. The overall external quantum efficiency (EQE) is determined by four factors including absorption, exciton diffusion, charge separation and charge collection.³³⁰ In cells with planar junctions, exciton diffusion length (10 nm or even smaller) is orders of magnitude shorter than its light absorption length, resulting in low overall conversion efficiency.³³¹ This challenge can be addressed by the bulk heterojunction structure, where electron donor and acceptor materials are completely mixed. In such PV systems, however, charge transport bottleneck become a critical issue.^{332,333} Introducing metal oxides to serve as the acceptor, so-called hybrid solar cell (HSC), has been considered as a capable approach to adjusting the acceptor/donor interfaces and facilitating charge separation and collection.³³¹ 1D TiO₂ nanostructure is one of the promising metal oxide candidates because of its appropriate electronic band structure for charge separation and transportation as well as the 1D morphology that serves as an ideal scaffold for polymer crystallization.¹⁵ 1D TiO₂ nanostructures also can act as the optical spacer²⁰ and protect layer³³⁴ in PSC.

Zeng et al. developed a large interconnecting network by inserting a TiO₂ NR layer between the photoactive polymer layer and the aluminum electrode.³³⁵ The interconnected NR/polymer network largely enhanced charge transport from polymer to the metal electrode and raised the ECE by 2.5 times compared to the reference device without the TiO₂ NR layer. Kuo et al. prepared vertically aligned TiO₂ NR arrays by sol-gel spin coating on AAO templates and filled the space between NRs with conjugated polymer.³³⁶ The integrated hybrid system achieved a power conversion efficiency of 0.512%. Williams et al. fabricated postlike anatase TiO₂ nanostructures via pattern replication in nonwetting templates (PRINT) process.³³⁷ 2-fold improvement relative to the reference bilayer cell was observed from the HSC devices.

Lin et al. revealed that TiO₂ NR surface modification was able to suppress charge recombination at P3HT/TiO₂ interfaces.³³⁸ By modifying the TiO₂ NR surface with interfacial ligand molecules including anthracene-9-carboxylic acid (ACA), tetracarboxy phthalocyanine copper(II) (CuPc-dye), and *cis*-bis(4,4-dicarboxy-2,2-bipyridine) dithiocyanato ruthenium(II) (N3-dye), electron transport toward the electrode was significantly accelerated and the electron back recombination was substantially suppressed. The recombination mechanism is schematically illustrated in the inset of Figure 43a. The reduced charge recombination through surface modification was confirmed experimentally by the transient open-circuit voltage decay (TOCVD) measurements, as shown in Figure 43a. The inset of Figure 43b shows the schematic solar cell device configuration. From the J - V characteristics of TiO₂/P3HT PSCs with different surface ligand modifications, N3-dye molecule modification yielded the best performance with a solar energy conversion efficiency of 2.20% (Figure 43b). Lu et al. synthesized Ag-TiO₂ NR composite *via* a photocatalytic approach, where the photogenerated electrons from TiO₂ NR

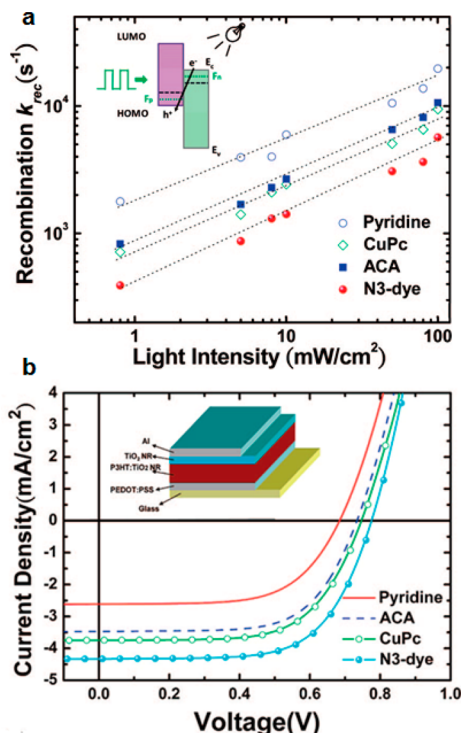


Figure 43. (a) TOCVD measurements of the charge recombination rate constant k versus light intensity at V_{oc} . Inset is a schematic illustration of the recombination mechanism and the TOCVD setup. (b) J - V characteristics of the photovoltaic devices with different interface ligand molecules measured under AM 1.5G 100 mW/cm^2 light intensity. Inset is the schematic configuration of the solar cell device. Reprinted with permission from ref 338. Copyright 2009, the American Chemical Society.

under UV illumination reduced the Ag^+ precursor to Ag NPs decorating on the TiO_2 surfaces.³³⁹ The presence of Ag was

found to be helpful in charge separation and transport in a PSC device, when the Ag- TiO_2 NR composite was used as the electron transport layer. A considerably enhanced efficiency (6.92%) was obtained from the Ag- TiO_2 NR composite electrode compared to pure TiO_2 NRs (5.81%).

On the other hand, removing unfavorable surface molecules/contaminations was also found to be an effective way to improving the charge transport property of TiO_2 NR-based polymer solar cells. Lojudice et al. revealed that the absorbed capping and hydrophilic ligands on the TiO_2 NR surface were detrimental to the charge transport in the TiO_2 NR-based PSCs.³⁴⁰ After removing surface molecules from TiO_2 NRs by UV light illumination, they integrated the TiO_2 NRs to both inverted and conventional PSCs. The efficiency of inverted and conventional devices showed three and two times enhancement regard to the untreated TiO_2 NR electrodes, respectively. Although 1D TiO_2 nanostructured HSCs demonstrated good potential for overcoming several critical design and operation limitations, its achieved performance is still far below the standard polymer bulk-heterojunction cells. A possible reason is the difficulty of optimizing all the HSC design parameters using the nanostructures. As a result, research in this area is mainly focused on demonstration and understanding of fundamental concept.³³¹

5.2.3. Quantum Dot Solar Cells. Colloidal quantum dot solar cells (QDSCs) are showing a promising future with unique merits of tunable spectral absorption, long-lifetime hot carriers, and multiple exciton generation by single photon, which may raise the efficiency higher than the thermodynamic limit of single junction bulk solar cells.³⁴¹ Recently, QDSCs have been developed with the highest 7% solar energy conversion efficiency using p-type QDs as absorbers and n-type wide bandgap semiconductors as electron collectors.¹⁸ Similar to DSSCs, introducing 1D TiO_2 nanostructure to QDSC design is also favorable for electron extraction and transport as well as obtaining high V_{oc} despite the types of

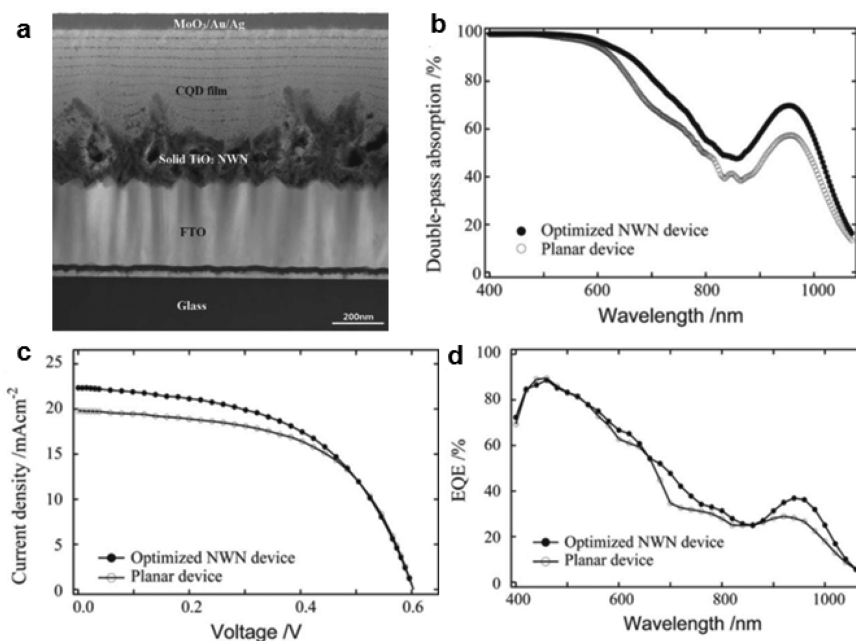


Figure 44. (a) TEM image of the TiO_2 NW-based QDSC. (b) Optical absorption spectra of TiO_2 planar and NW devices. (c) J - V curves of planar and NW QDSCs under AM1.5G illumination. (d) External quantum efficiencies of planar and NW QDSCs. Reprinted with permission from ref 349. Copyright 2013, Wiley-VCH.

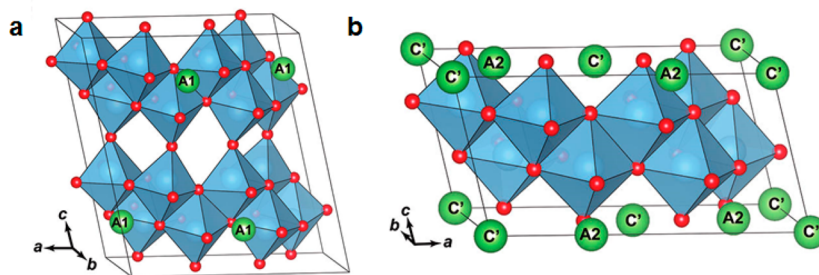


Figure 45. Ground state structure at a Li concentration of (a) 0.25 and (b) 0.75. Reprinted with permission from ref 357. Copyright 2012, the American Chemical Society.

QDSCs.³⁴² The advantages of using QDs over dye molecules include tunable band gap for broad-band absorption, very high efficiency limit, and high-quality solid state heterojunction.³⁴¹

Many research efforts have been devoted to studying the geometry contribution to the performance gain of TiO₂ NW-based QDSCs. Most QDSCs made from vertically aligned TiO₂ NW arrays exhibited photocurrent enhancements compared to conventional TiO₂ NP electrodes.^{343–348} The contributions made by TiO₂ 1D nanostructures were basically the same as they did in other types of solar cells. Lan et al. developed a solution-based process for fabricating TiO₂ NW 3D networks using a ZnO template.³⁴⁹ The dense TiO₂ NW network provided a continuous scaffold to build a depleted bulk heterojunction QDSC employing hybrid passivated colloidal QDs. The entire device structure is shown in Figure 44a. This new electrode design allowed the implementation of thicker active layer with largely improved light absorption and better charge transport, resulting in higher efficiency compared to planar cells. Figure 44b–d compares the absorptions, *J*–*V* characteristics, and EQEs, respectively, from QDSCs that were made using NW-based electrode and planar electrode, demonstrating improved performance as a result of the NW morphology. The optimal output of the TiO₂ NW-based QDSCs reached a high overall efficiency of 7.3% ± 0.2%. Lo Giudice et al. fabricated QDSCs composed of colloidal PbS QDs and TiO₂ NRs via a room-temperature solution process, which was capable for flexible plastic substrates and low-cost cell production.³⁵⁰ The QDSCs fabricated on rigid glass substrates and flexible plastic substrates achieved efficiencies of 3.6% and 1.8%, respectively.

5.3. 1D TiO₂ Nanostructures for Energy Storage

Development of next generation electrochemical energy storage systems (batteries or super capacitors) demands high energy density, high power, high charging/discharging rate, low weight, and compact size. 1D nanostructures are currently studied intensively as the building blocks for battery electrodes.^{54,351–354} Similar to photovoltaic devices, the applications of 1D nanostructures in electrode design could offer high surface areas and shorter ion path lengths compared to conventional thin film configurations. These merits could lead to higher capacities at high charge/discharge rates. Although TiO₂ is not within the core electrode material selection, its 1D morphologies still received considerable research attentions for the development of high-performance electrode architectures.

5.3.1. Lithium Ion Batteries. Inspired by the large lithium intercalation capacity in TiO₂, researchers have explored the applications of TiO₂ as anodes in lithium ion battery during the past decade.^{11,355,356} Among several TiO₂ polymorphs, TiO₂(B) has the lowest density and demonstrated a high

reversible capacity experimentally.¹¹ Based on first principle calculation, Dalton et al. predicated that in TiO₂(B), a Li/Ti ratio up to 1.25 is thermodynamically favorable.³⁵⁷ Such a large capacity is related to the favored intercalation sites switching in TiO₂(B) depending on the concentrations of Li. As shown in Figure 45, they revealed that there would be three Li intercalations sites occupied at different stages of intercalation in TiO₂(B). The A1 site is 5-fold coordinated to oxygen atoms sitting in the two (003) planes; the A2 site is also 5-fold coordinated to oxygen atoms sitting in the (001) plane; the C' site is 4-fold coordinated to oxygen sitting in the (001) plane. When the Li concentration is low, the A1 site intercalation leads to a system with the lowest free energy. When the Li concentration is high (>0.75), A2 and C' sites are completely occupied. The intercalation accompanies with the change of the lattice parameter and increases in TiO₂(B)'s volume.

NW forms of TiO₂(B) are believed to be superior to its bulk form as it can tolerate more volume expansion and have short ionic transport path for charging/discharging operation.³⁵⁸ Experimentally, a Li/Ti ratio of 0.91 in TiO₂(B) NWs was achieved by Armstrong et al.¹¹ Such a Li/Ti ratio is equal to the capacity of 305 mA h g⁻¹. In addition, they also observed that the charging/discharging rate in TiO₂(B) NWs was faster than the thin film morphology. Figure 46 shows the superior performance of TiO₂(B) NWs in comparison to bulk TiO₂(B) materials. The achieved specific charge-storage capacity was almost twice as high as that of anatase Li_{0.5}TiO₂ (165 mA h g⁻¹) and spinel Li₄Ti₅O₁₂ (175 mA h g⁻¹). TiO₂(B) NW-based anodes have also been integrated with LiFePO₄ and

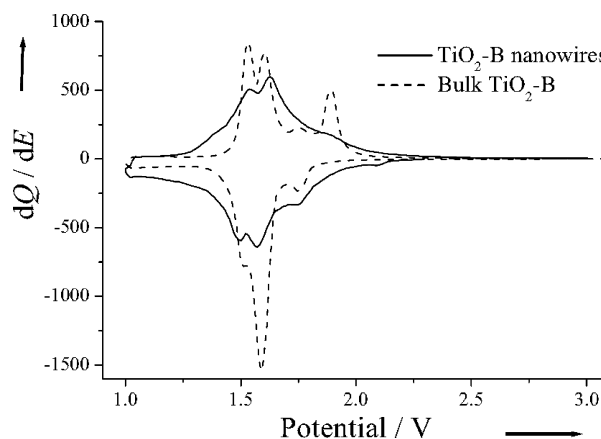


Figure 46. Incremental capacity curves measured from TiO₂(B) NW and bulk TiO₂(B) electrodes cycled at 10 mA g⁻¹ within at voltage limit from 1 to 3 V. Reprinted with permission from ref 11. Copyright 2005, Wiley-VCH.

LiNi_{0.5}Mn_{1.5}O₄ cathodes to fabricate rechargeable lithium ion batteries, which demonstrated higher capacities than Li₄Ti₅O₁₂ powder anodes (225 mA h g⁻¹ vs 150 mA h g⁻¹ at C/5).³⁵⁵ The TiO₂(B) NW-based batteries also showed excellent cycling stability and as much as 80% of the low-rate capacity was retained at 5C.

Additives, such as graphene³⁵⁹ and metal NWs³⁶⁰ were integrated with TiO₂ electrodes to improve the electric conductivity, and thus to further improve the charging/discharging rates. Wang et al. directly grew rutile TiO₂ NRs on graphene sheets and applied this hybrid structure in lithium ion batteries. Significant enhancement in specific capacity was obtained at high charging rate. Wang et al. fabricated a 3D Ni NW network followed by a TiO₂ ALD coating.³⁶⁰ This 3D Ni/TiO₂ NW heterostructure overcame the top agglomeration problem in NW-based battery electrodes. As a result, 100% capacity is retained after 600 operation cycles.

5.3.2. Supercapacitors. In addition to battery electrode developments, 1D TiO₂ nanostructures were also explored in supercapacitor applications, particularly, supercapacitor-battery hybrid devices. Lu et al. reported a TiO₂ NW-based asymmetric supercapacitor (ASC).³⁶¹ A typical ASC is composed of a battery-type Faradaic electrode as an energy source and a capacitor-type electrode as a power source and thereby to integrate the merits from both batteries (high energy density) and supercapacitors (high power density and cycle life).³⁶² ASCs can raise the maximum operation voltage by combining the voltage windows of the two types of electrodes.³⁶³ Lu et al. fabricated a flexible solid-state ASC device with hydrogen treated TiO₂-MnO₂ and TiO₂-carbon core-shell NWs as the positive and negative electrodes, respectively. The TiO₂ core with improved electron mobility after hydrogenation would serve as a conductive channel to support the function of electrochemically active materials. The core-shell NW electrodes exhibited superior capacitance performance, demonstrating a 1.8 V voltage window (Figure 47a) and a specific capacitance of 139.6 F g⁻¹ with an excellent cycling performance (8.8% capacitance loss after 5000 cycles, Figure 47b). Wang et al. developed a hybrid supercapacitor consisting of a carbon nanotube (CNT) cathode and a TiO₂(B) NW (TNW) anode. Compared with pure CNT-based supercapacitors, CNT-TNW systems doubled the energy density (12.5 W h kg⁻¹), while maintaining a comparable cycling life. The energy density gain was attributed to the synergistic effects of CNT and TNW, i.e., TNW anode improved the energy density and CNT cathode guaranteed a desirable cycling life.³⁶⁴ Integrated supercapacitor-PEC systems based on TiO₂/Ni(OH)₂ core-shell NR arrays were developed by Xia et al. to improve the solar energy utilization.³⁶⁵ In this device, photogenerated holes were stored in the pseudocapacitive Ni(OH)₂ layer and photogenerated electrons transported to the counter electrode for hydrogen evolution.

5.4. Electrochromism and Electrochromic Devices

Electrochromism describes a phenomenon that a material changes color upon oxidation or reduction reactions to the crystal lattices. When monovalent ions are intercalated into TiO₂, its color often changes from transparent to bluish, which reflects the electrochromic property of TiO₂. The well-accepted model during this process is: TiO₂ + x(M⁺ + e⁻) = M_xTiO₂.³⁶⁶ The electrochromism of TiO₂ motivated people to seek for its application as smart window, displays, sunroofs and mirrors. The coloration extent depends on the amount of metal ions or

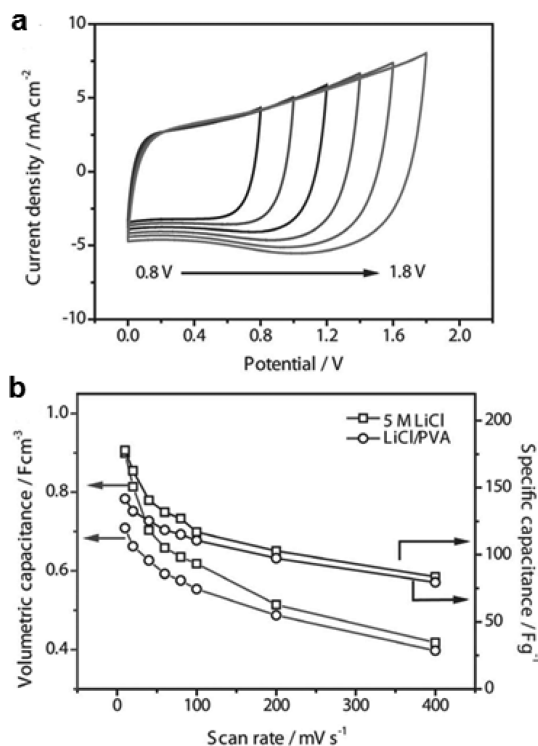


Figure 47. (a) C–V plots of a solid-state ASC device obtained within different scan voltage windows. (b) Calculated volumetric and specific capacitance as a function of scan rate in LiCl aqueous electrolyte (squares) and LiCl/PVA gel electrolyte (circles). Reprinted with permission from ref 361. Copyright 2013, Wiley-VCH.

proton intercalated to TiO₂: higher intercalation ratio leads to more color contrast. In addition, faster intercalation rate renders a faster coloration process, which is vital since such electrochemical based ions insertion is relatively slow. The large surface area and high aspect ratio of TiO₂ NW structures naturally render a higher intercalation ratio and rate. Xia et al. coated various conducting polymers, including polyaniline (PANI), and PEDOT [poly(3,4-ethylenedioxythiophene)] onto TiO₂ NW arrays using electrochemical polymerization method.³⁶⁷ The TiO₂/PANI core/shell NW structure demonstrated an effective electrochromic property with four color modes (Figure 48a) and a rapid optical switching speed that was superior to traditional inorganic electrochromic thin film including NiO and WO₃ (Figure 48b). Similarly, Vuong et al. demonstrated a substantially enhanced electrochromic property of WO₃ scaffold-supported TiO₂ NWs compared to their thin film counterparts.³⁶⁸ Chen et al. developed a high-porosity anatase TiO₂ NW-based device with dual antireflective and electrochromic functionalities.³⁶⁹ The device showed an enhanced optical transparency in visible light range, better color contrasts and faster color-switching time compared to NP-based device. The low refractive index and high porosity were believed to be responsible for the performance improvements. Though challenges such as the light scattering from NW surfaces remain in the development of highly transparent TiO₂ devices, the predominant merits of NW morphology are driving the development of fast and high-contrast electrochromic device forward.

5.5. Solid State Sensors

Solid state sensors operate based on surface reduction–oxidation (redox) reactions that alter its electrical conductivity.

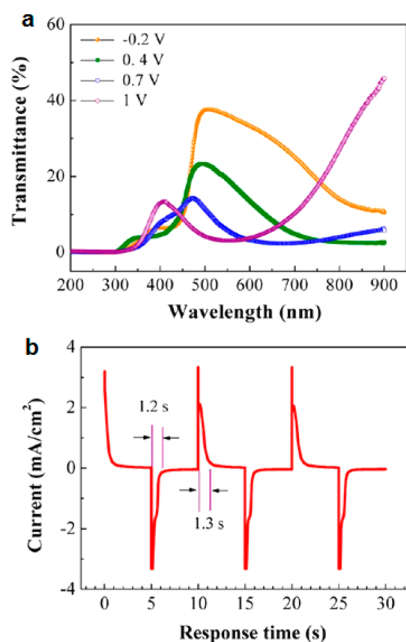


Figure 48. (a) Transmittance spectra of coaxial TiO₂/PANI core/shell NR arrays under different applied potentials. (b) The switching characteristic of coaxial TiO₂/PANI core/shell NR arrays. Reprinted with permission from ref 367. Copyright 2013, the American Chemical Society.

Sensitivity much higher than that of bulk or thin film sensors has been demonstrated in chemiresistor sensors based on 1D nanostructures.³⁷⁰ The high sensitivity of NWs/NTs is associated with the high surface-to-volume ratio and small thickness.

Wide band gap metal oxides are able to detect trace concentrations of various gases in air via charge-transfer interactions between sensor and chemisorbed species. TiO₂ NWs have been widely investigated as solid state sensory elements for various gaseous species including H₂O, C₂H₅OH, NH₃, and NO₂.^{364,371–374} Li et al. developed highly sensitive and stable humidity nanosensors using LiCl-doped TiO₂ nanofibers fabricated by electrospinning.³⁷¹ The sensor exhibited reasonably rapid response time (<3s) and recovery time (<7s) within a wide range of 11–95% humidity in air at room temperature. Kim et al. fabricated interconnected TiO₂ nanofiber mats with high porosity by electrospinning. The porous 3D structures formed by ultrasmall fibers offered very large active surfaces and thus more effective gas accessibility. As a result, it exhibited an excellent sensitivity to NO₂ gas with the detection limit estimated to below 1 ppb.³⁷⁴ Caricato et al. reported a NO₂ gas sensor based on a brookite TiO₂ NR/NP film deposited by matrix-assisted pulsed laser evaporation.³⁷⁵ Stable and reversible sensing signals were acquired after exposing the TiO₂ nanostructure to 1 ppm of NO₂ in dry air at 300 °C and the response and recovery time was found to be 2 and 13 min, respectively. Tian et al. fabricated precisely ordered TiO₂ NW using electron beam lithography, with which a robust and high-performance ethanol gas sensor was demonstrated.³⁷⁶ Sensing response and reaction time were determined within a temperature range from 200 to 350 °C. The optimal performance was identified at 300 °C, where the TiO₂ NW sensor achieved a rise/recovery time of 3.2s/17.5s and a corresponding signal change of 21.7% upon 0.2 μg ethanol injection.

5.6. Mechanical Properties

The single-crystalline 1D morphology is also able to enhance the mechanical strength and introduce higher fracture resistance of ceramic NWs compared to their bulk forms. Molecular dynamics simulations carried out by Dai et al. showed that TiO₂ NWs might be stiffer and superior to bulky material with respect to their toughness and ductility.³⁷⁷ When NW is thin enough (<1 nm), the free surface effects dictate the structure and mechanical property and the atoms on the surface can relax themselves to reach an equilibrium state. Based on their simulation, ultrathin TiO₂ NWs (diameter <3 nm) could tolerate a strain of maximum 1.7%, which was 1 order of magnitude higher than bulk or thin film structures. As shown in Figure 49, both Young's modulus and ultimate tensile strength

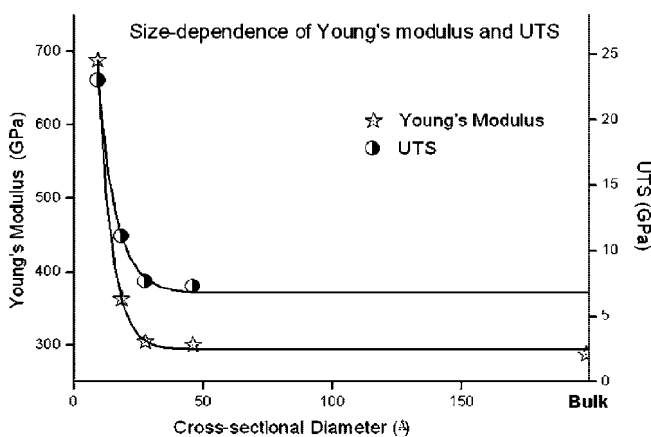


Figure 49. Calculated Young's modulus and ultimate tensile stress of TiO₂ NWs as a function of the NW diameter. Reprinted with permission from ref 377. Copyright 2009, the American Chemical Society.

fall approximately exponentially when NW's diameter was reduced down to <3 nm. Although very intriguing, due to the difficulty in synthesizing ideal TiO₂ NWs for mechanical testing, such size dependent effect is to be validated experimentally in the future.

6. CONCLUSION

Recent years evidenced explosive research and development efforts on TiO₂ nanomaterials, particularly in the energy-related areas. The NW structure of TiO₂ is continuously attracting increasing research interests from the fundamental understanding of growth behavior to rational control of structure and property and to the exploration of advanced applications. This review article is centralized on the TiO₂ NW structures and emphasizes the most current research outcomes covering structure, growth, property, and application. In this article, we first summarized the structural features of the four TiO₂ polymorphs that have been seen in TiO₂ nanostructures. Then representative 1D growth mechanisms of TiO₂ crystals (oriented attachment and surface-reaction-limited growth) were discussed in detail. After this, representative synthetic methods for making TiO₂ NWs were reviewed and grouped in four different categories, i.e., solution-based approaches, vapor deposition methods, templated growth, and top-down fabrication techniques. Their basic procedures, typical products, strengths, and limitations were discussed and compared, which provided a convenient guideline for synthesizing morphology

and property controlled TiO₂ 1D nanostructures. At last, the 1D morphology-related properties were reviewed and discussed together with their application potentials. The discussion was mainly focused on how TiO₂ NWs could benefit the solar energy conversion efficiency in PEC and photovoltaic systems. Other properties and application potentials, including energy storage, electrochromism, sensing, and mechanical merits, also were reviewed.

In general, the TiO₂ NW structure possesses both significant advantages and limitations as a novel building block for developing energy and environmental devices or systems compared to other bulk or nanoscale morphologies. In order to achieve the desired improvements by using TiO₂ NWs, several critical aspects still need to be addressed fundamentally and practically. First, repeatable, reliable, controllable, and scalable synthesis approaches are needed to create high quality TiO₂ NWs with designed morphology and properties. Second, the relationships between the 1D morphology, crystal structure, composition, and material's electronic and chemical properties need to be understood with greater depth, so that lead to a well-guided application roadmap. Third, reliable approaches need to be designed to realize large scale integration of TiO₂ NWs with other functional components in complete device systems. This also requires a good understanding of the heterogeneous interfaces and the associated transport properties. Supported by these fundamental understandings, integration of TiO₂ NWs with other functional materials into heterogeneous and multifunctional 3D complex nanosystems may represent a promising future direction of 1D TiO₂ nanostructure development.

AUTHOR INFORMATION

Corresponding Author

*E-mail: xudong@engr.wisc.edu.

Present Address

[†]School of Engineering and Applied Sciences, Harvard University, Cambridge, MA 02138.

Notes

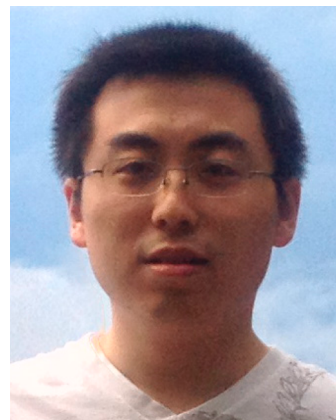
The authors declare no competing financial interest.

Biographies



Xudong Wang is an assistant professor in the department of Materials Science and Engineering at University of Wisconsin-Madison. He received his Ph.D. degree in Materials Science and Engineering from Georgia Tech in 2005. His current research interests include studying the growth and assembly of oxide nanowire arrays into complex 3D nanostructures, understanding the coupling effect of semiconductor

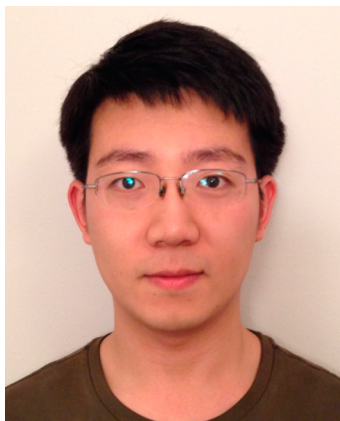
properties and piezoelectric charge displacement, and developing a nanogenerator that uses piezoelectric nanomaterials to convert low level mechanical energy into electricity.



Zhaodong Li is currently a Ph.D. student of Materials Engineering at the University of Wisconsin-Madison under the supervision of Prof. Xudong Wang. He obtained his B.S. degree in Applied Physics at Tianjin University, China in 2009 and M.S. degree in Physics at Southern University A&M College in 2011. His current research focuses on the fundamental understanding and system design of atomic layer deposition technology and its application for 3D nanowire architectures synthesis.



Jian Shi is currently a postdoctoral fellow in the School of Engineering and Applied Sciences at Harvard University. He received his B.S. degree in Materials Science and Engineering at the Xi'an Jiaotong University, China in 2006, his M.S. Degree in Mechanical Engineering at the University of Missouri—Columbia in 2008, and his Ph.D. degree in Materials Science at the University of Wisconsin—Madison in 2012. His Ph.D. research focused on the nucleation and growth of oxide nanomaterials, photovoltaics, photoelectrochemical cells, nanogenerators, and piezotronics. He is currently working on understanding and engineering metal-insulator transition in correlated nickelates and exploring the applications of correlated oxides interfaced with neural systems.



Yanhao Yu received his B.S. degree in Chemical Engineering at Dalian University of Technology, China in 2011. He is now a Ph.D. student of Materials Engineering at University of Wisconsin-Madison under the supervision of Prof. Xudong Wang. His current research focuses on the growth and integration of functional oxide nanomaterials for the applications of photovoltaics and photoelectrochemical water splitting.

ACKNOWLEDGMENTS

We thank the U.S. Department of Energy, Office of Basic Energy Sciences under Award DE-SC0008711, Air Force under Award FA9550-13-1-0168, and National Science Foundation under Award CMMI-1148919 for financial support.

REFERENCES

- (1) Pfaff, G.; Reynders, P. *Chem. Rev.* **1999**, *99*, 1963.
- (2) Zallen, R.; Moret, M. P. *Solid State Commun.* **2006**, *137*, 154.
- (3) Braun, J. H.; Baidins, A.; Marganski, R. E. *Prog. Org. Coat.* **1992**, *20*, 105.
- (4) Wakefield, G.; Green, M.; Lipscomb, S.; Flutter, B. *Mater. Sci. Technol.* **2004**, *20*, 985.
- (5) Fujishima, A.; Honda, K. *Nature* **1972**, *238*, 37.
- (6) Yang, H. G.; Sun, C. H.; Qiao, S. Z.; Zou, J.; Liu, G.; Smith, S. C.; Cheng, H. M.; Lu, G. Q. *Nature* **2008**, *453*, 638.
- (7) Jiu, J. T.; Isoda, S.; Wang, F. M.; Adachi, M. *J. Phys. Chem. B* **2006**, *110*, 2087.
- (8) Khan, S. U. M.; Al-Shahry, M.; Ingler, W. B. *Science* **2002**, *297*, 2243.
- (9) Liu, B.; Aydil, E. S. *J. Am. Chem. Soc.* **2009**, *131*, 3985.
- (10) Zuruzi, A. S.; Kolmakov, A.; MacDonald, N. C.; Moskovits, M. *Appl. Phys. Lett.* **2006**, *88*, 102904.
- (11) Armstrong, A. R.; Armstrong, G.; Canales, J.; Garcia, R.; Bruce, P. G. *Adv. Mater.* **2005**, *17*, 862.
- (12) Ni, M.; Leung, M. K. H.; Leung, D. Y. C.; Sumathy, K. *Renew. Sust. Energ. Rev.* **2007**, *11*, 401.
- (13) Bach, U.; Lupo, D.; Comte, P.; Moser, J. E.; Weissortel, F.; Salbeck, J.; Spreitzer, H.; Graetzel, M. *Nature* **1998**, *395*, 583.
- (14) Law, M.; Greene, L. E.; Radenovic, A.; Kuykendall, T.; Liphardt, J.; Yang, P. D. *J. Phys. Chem. B* **2006**, *110*, 22652.
- (15) Greene, L. E.; Law, M.; Yuhas, B. D.; Yang, P. D. *J. Phys. Chem. C* **2007**, *111*, 18451.
- (16) Liu, J.; Kuo, Y. T.; Klabunde, K. J.; Rochford, C.; Wu, J.; Li, J. *ACS Appl. Mater. Interfaces* **2009**, *1*, 1645.
- (17) Burschka, J.; Pellet, N.; Moon, S. J.; Humphry-Baker, R.; Gao, P.; Nazeeruddin, M. K.; Gratzel, M. *Nature* **2013**, *499*, 316.
- (18) Ip, A. H.; Thon, S. M.; Hoogland, S.; Voznyy, O.; Zhitomirsky, D.; Debnath, R.; Levina, L.; Rollny, L. R.; Carey, G. H.; Fischer, A.; Kemp, K. W.; Kramer, I. J.; Ning, Z.; Labelle, A. J.; Chou, K. W.; Amassian, A.; Sargent, E. H. *Nat. Nanotechnol.* **2012**, *7*, 577.
- (19) Günes, S.; Neugebauer, H.; Sariciftci, N. S. *Chem. Rev.* **2007**, *107*, 1324.
- (20) Kim, J. Y.; Kim, S. H.; Lee, H. H.; Lee, K.; Ma, W.; Gong, X.; Heeger, A. J. *Adv. Mater.* **2006**, *18*, 572.
- (21) Chen, X. B.; Liu, L.; Yu, P. Y.; Mao, S. S. *Science* **2011**, *331*, 746.
- (22) Bavykin, D. V.; Friedrich, J. M.; Walsh, F. C. *Adv. Mater.* **2006**, *18*, 2807.
- (23) Hagfeldt, A.; Graetzel, M. *Chem. Rev.* **1995**, *95*, 49.
- (24) Burda, C.; Chen, X.; Narayanan, R.; El-Sayed, M. A. *Chem. Rev.* **2005**, *105*, 1025.
- (25) Murray, C. B.; Kagan, C. R.; Bawendi, M. G. *Annu. Rev. Mater. Sci.* **2000**, *30*, 545.
- (26) Cushing, B. L.; Kolesnichenko, V. L.; O'Connor, C. J. *Chem. Rev.* **2004**, *104*, 3893.
- (27) Linsebigler, A. L.; Lu, G. Q.; Yates, J. T. *Chem. Rev.* **1995**, *95*, 735.
- (28) Chen, X.; Mao, S. S. *J. Nanosci. Nanotechnol.* **2006**, *6*, 906.
- (29) Roduner, E. *Chem. Soc. Rev.* **2006**, *35*, 583.
- (30) Valden, M.; Lai, X.; Goodman, D. W. *Science* **1998**, *281*, 1647.
- (31) Chen, X.; Mao, S. S. *Chem. Rev.* **2007**, *107*, 2891.
- (32) Chan, C. K.; Peng, H. L.; Liu, G.; McIlwrath, K.; Zhang, X. F.; Huggins, R. A.; Cui, Y. *Nat. Nanotechnol.* **2008**, *3*, 31.
- (33) Law, M.; Greene, L. E.; Johnson, J. C.; Saykally, R.; Yang, P. D. *Nat. Mater.* **2005**, *4*, 455.
- (34) Boettcher, S. W.; Spurgeon, J. M.; Putnam, M. C.; Warren, E. L.; Turner-Evans, D. B.; Kelzenberg, M. D.; Maiolo, J. R.; Atwater, H. A.; Lewis, N. S. *Science* **2010**, *327*, 185.
- (35) Yan, R. X.; Gargas, D.; Yang, P. D. *Nat. Photonics* **2009**, *3*, 569.
- (36) Dong, W.; Zhang, T.; Epstein, J.; Cooney, L.; Wang, H.; Li, Y.; Jiang, Y.-B.; Cogbill, A.; Varadan, V.; Tian, Z. R. *Chem. Mater.* **2007**, *19*, 4454.
- (37) Huang, C. T.; Song, J. H.; Lee, W. F.; Ding, Y.; Gao, Z. Y.; Hao, Y.; Chen, L. J.; Wang, Z. L. *J. Am. Chem. Soc.* **2010**, *132*, 4766.
- (38) Wang, Z. L. *Nano Today* **2010**, *5*, 540.
- (39) Ding, Y.; Wang, X. D.; Wang, Z. L. *Chem. Phys. Lett.* **2004**, *398*, 32.
- (40) Wang, X. D.; Song, J. H.; Wang, Z. L. *J. Mater. Chem.* **2007**, *17*, 711.
- (41) Banfield, J. F.; Veblen, D. R. *Am. Mineral.* **1992**, *77*, 545.
- (42) Cromer, D. T.; Herrington, K. J. *Am. Chem. Soc.* **1955**, *77*, 4708.
- (43) Marchand, R.; Brohan, L.; Tourmoux, M. *Mater. Res. Bull.* **1980**, *15*, 1129.
- (44) Gong, X.-Q.; Selloni, A.; Batzill, M.; Diebold, U. *Nat. Mater.* **2006**, *5*, 665.
- (45) Shibata, N.; Goto, A.; Choi, S.-Y.; Mizoguchi, T.; Findlay, S. D.; Yamamoto, T.; Ikuhara, Y. *Science* **2008**, *322*, 570.
- (46) Weigang, L.; Britain, B.; Gilberto, C.; Sergio, M.-R.; Patrick, J. F.; Miguel, J.-Y. *Nanotechnology* **2012**, *23*, 335706.
- (47) Shi, J.; Li, Z.; Kvit, A.; Krylyuk, S.; Davydov, A. V.; Wang, X. *Nano Lett.* **2013**, *13*, 5727.
- (48) De Caro, L.; Carlino, E.; Caputo, G.; Cozzoli, P. D.; Giannini, C. *Nat. Nanotechnol.* **2010**, *5*, 360.
- (49) Jun, Y.-w.; Choi, J.-s.; Cheon, J. *Angew. Chem., Int. Ed.* **2006**, *45*, 3414.
- (50) Jun, Y.-w.; Lee, J.-H.; Choi, J.-s.; Cheon, J. *J. Phys. Chem. B* **2005**, *109*, 14795.
- (51) Niederberger, M. *Acc. Chem. Res.* **2007**, *40*, 793.
- (52) Cozzoli, P. D.; Pellegrino, T.; Manna, L. *Chem. Soc. Rev.* **2006**, *35*, 1195.
- (53) Ha, J. Y.; Sosnowchik, B. D.; Lin, L. W.; Kang, D. H.; Davydov, A. V. *Appl. Phys. Express* **2011**, *4*, 065002.
- (54) Lee, J. C.; Park, K. S.; Kim, T. G.; Choi, H. J.; Sung, Y. M. *Nanotechnology* **2006**, *17*, 4317.
- (55) Xiang, B.; Zhang, Y.; Wang, Z.; Luo, X. H.; Zhu, Y. W.; Zhang, H. Z.; Yu, D. P. *J. Phys. D: Appl. Phys.* **2005**, *38*, 1152.
- (56) Pradhan, S. K.; Reucroft, P. J.; Yang, F.; Dozier, A. J. *Cryst. Growth* **2003**, *256*, 83.
- (57) Wu, J.-M.; Shih, H. C.; Wu, W.-T. *Nanotechnology* **2006**, *17*, 105.
- (58) Fan, H. J.; Werner, P.; Zacharias, M. *Small* **2006**, *2*, 700.
- (59) Wang, N.; Cai, Y.; Zhang, R. Q. *Mater. Sci. Eng., R* **2008**, *60*, 1.

- (60) Wacaser, B. A.; Dick, K. A.; Johansson, J.; Borgstrom, M. T.; Depert, K.; Samuelson, L. *Adv. Mater.* **2009**, *21*, 153.
- (61) Lieber, C. M.; Wang, Z. L. *MRS Bull.* **2007**, *32*, 99.
- (62) Xia, Y.; Yang, P.; Sun, Y.; Wu, Y.; Mayers, B.; Gates, B.; Yin, Y.; Kim, F.; Yan, H. *Adv. Mater.* **2003**, *15*, 353.
- (63) Hu, J.; Odom, T. W.; Lieber, C. M. *Acc. Chem. Res.* **1999**, *32*, 435.
- (64) Dubrovskii, V. G.; Sibirev, N. V.; Cirilin, G. E.; Soshnikov, I. P.; Chen, W. H.; Larde, R.; Cadel, E.; Pareige, P.; Xu, T.; Grandidier, B.; Nys, J. P.; Stievenard, D.; Moewe, M.; Chuang, L. C.; Chang-Hasnain, C. *Phys. Rev. B* **2009**, *79*, 205316.
- (65) Wang, Z. L. *ACS Nano* **2008**, *2*, 1987.
- (66) Shi, J.; Wang, X. D. *J. Vac. Sci. Technol. B* **2011**, *29*, 060801.
- (67) Patolsky, F.; Lieber, C. M. *Mater. Today* **2005**, *8*, 20.
- (68) Cao, G.; Wang, Y. *Nanostructures and Nanomaterials: Synthesis, Properties, and Applications*, 2nd ed.; World Scientific: Singapore, 2010.
- (69) Penn, R. L.; Banfield, J. F. *Am. Mineral.* **1998**, *83*, 1077.
- (70) Shi, J.; Sun, C.; Starr, M. B.; Wang, X. *Nano Lett.* **2011**, *11*, 624.
- (71) Kim, M. H.; Baik, J. M.; Zhang, J. P.; Larson, C.; Li, Y. L.; Stucky, G. D.; Moskovits, M.; Wodtke, A. M. *J. Phys. Chem. C* **2010**, *114*, 10697.
- (72) Barnard, A. S.; Zapol, P.; Curtiss, L. A. *J. Chem. Theory Comput.* **2005**, *1*, 107.
- (73) Oskam, G.; Nellore, A.; Penn, R. L.; Searson, P. C. *J. Phys. Chem. B* **2003**, *107*, 1734.
- (74) Shi, J.; Wang, X. *Energy Environ. Sci.* **2012**, *5*, 7918.
- (75) Penn, R. L.; Banfield, J. F. *Geochim. Cosmochim. Acta* **1999**, *63*, 1549.
- (76) Penn, R. L. *J. Phys. Chem. B* **2004**, *108*, 12707.
- (77) Ribeiro, C.; Lee, E. J. H.; Longo, E.; Leite, E. R. *ChemPhysChem* **2005**, *6*, 690.
- (78) Burrows, N. D.; Yuwono, V. M.; Penn, R. L. *MRS Bull.* **2010**, *35*, 133.
- (79) Jun, Y. W.; Casula, M. F.; Sim, J. H.; Kim, S. Y.; Cheon, J.; Alivisatos, A. P. *J. Am. Chem. Soc.* **2003**, *125*, 15981.
- (80) Li, X. L.; Peng, Q.; Yi, J. X.; Wang, X.; Li, Y. *Chemistry* **2006**, *12*, 2383.
- (81) Cozzoli, P. D.; Kornowski, A.; Weller, H. *J. Am. Chem. Soc.* **2003**, *125*, 14539.
- (82) Zhang, Z. H.; Zhong, X. H.; Liu, S. H.; Li, D. F.; Han, M. Y. *Angew. Chem., Int. Ed.* **2005**, *44*, 3466.
- (83) Joo, J.; Kwon, S. G.; Yu, T.; Cho, M.; Lee, J.; Yoon, J.; Hyeon, T. *J. Phys. Chem. B* **2005**, *109*, 15297.
- (84) Ma, R.; Fukuda, K.; Sasaki, T.; Osada, M.; Bando, Y. *J. Phys. Chem. B* **2005**, *109*, 6210.
- (85) Amin, S. S.; Nicholls, A. W.; Xu, T. T. *Nanotechnology* **2007**, *18*, 445609.
- (86) Mukherjee, K.; Teng, T. H.; Jose, R.; Ramakrishna, S. *Appl. Phys. Lett.* **2009**, *95*, 012101.
- (87) Fujihara, K.; Kumar, A.; Jose, R.; Ramakrishna, S.; Uchida, S. *Nanotechnology* **2007**, *18*, 365709.
- (88) Kisumi, T.; Tsujiko, A.; Murakoshi, K.; Nakato, Y. *J. Electroanal. Chem.* **2003**, *545*, 99.
- (89) Albu, S. P.; Ghicov, A.; Macac, J. M.; Hahn, R.; Schmuiki, P. *Nano Lett.* **2007**, *7*, 1286.
- (90) Zhu, Y.; Qian, Y. *Sci. China, Ser. G: Phys., Mech. Astron.* **2009**, *52*, 13.
- (91) Vayssieres, L. *Adv. Mater.* **2003**, *15*, 464.
- (92) Yu, H.; Buhro, W. E. *Adv. Mater.* **2003**, *15*, 416.
- (93) Chang, Y.; Lye, M. L.; Zeng, H. C. *Langmuir* **2005**, *21*, 3746.
- (94) Sun, Y.; Gates, B.; Mayers, B.; Xia, Y. *Nano Lett.* **2002**, *2*, 165.
- (95) Kasuga, T.; Hiramatsu, M.; Hoson, A.; Sekino, T.; Niihara, K. *Langmuir* **1998**, *14*, 3160.
- (96) Yao, B. D.; Chan, Y. F.; Zhang, X. Y.; Zhang, W. F.; Yang, Z. Y.; Wang, N. *Appl. Phys. Lett.* **2003**, *82*, 281.
- (97) Tian, Z. R.; Voigt, J. A.; Liu, J.; McKenzie, B.; Xu, H. *J. Am. Chem. Soc.* **2003**, *125*, 12384.
- (98) Ye, Z. Z.; Huang, J. Y.; Xu, W. Z.; Zhou, J.; Wang, Z. L. *Solid State Commun.* **2007**, *141*, 464.
- (99) Melcarne, G.; De Marco, L.; Carlino, E.; Martina, F.; Manca, M.; Cingolani, R.; Gigli, G.; Ciccarella, G. *J. Mater. Chem.* **2010**, *20*, 7248.
- (100) Christy, P. D.; Melikechi, N.; Nirmala Jothi, N. S.; Baby Suganthi, A. R.; Sagayaraj, P. *J. Nanopart. Res.* **2010**, *12*, 2875.
- (101) Tahir, M. N.; Theato, P.; Oberle, P.; Melnyk, G.; Faiss, S.; Kolb, U.; Janshoff, A.; Stepputat, M.; Tremel, W. *Langmuir* **2006**, *22*, 5209.
- (102) Kandiel, T. A.; Feldhoff, A.; Robben, L.; Dillert, R.; Bahnemann, D. W. *Chem. Mater.* **2010**, *22*, 2050.
- (103) Chi, B.; Victorio, E. S.; Jin, T. *Nanotechnology* **2006**, *17*, 2234.
- (104) Hwang, Y. J.; Hahn, C.; Liu, B.; Yang, P. *ACS Nano* **2012**, *6*, 5060.
- (105) Cho, I. S.; Chen, Z.; Forman, A. J.; Kim, D. R.; Rao, P. M.; Jaramillo, T. F.; Zheng, X. *Nano Lett.* **2011**, *11*, 4978.
- (106) Das, K.; Panda, S. K.; Chaudhuri, S. *J. Cryst. Growth* **2008**, *310*, 3792.
- (107) Mu, Q.; Li, Y.; Wang, H.; Zhang, Q. *J. Colloid Interface Sci.* **2012**, *365*, 308.
- (108) Finkelstein-Shapiro, D.; Tsai, C. Y. H.; Li, S.; Gray, K. A. *Chem. Phys. Lett.* **2012**, *546*, 106.
- (109) Shen, X. J.; Zhang, J. L.; Tian, B. Z. *J. Mater. Sci.* **2012**, *47*, 3855.
- (110) Wu, Y.; Long, M.; Cai, W.; Dai, S.; Chen, C.; Wu, D.; Bai, J. *Nanotechnology* **2009**, *20*, 185703.
- (111) Liu, D.; Liu, T.; Lv, C.; Zeng, W. *J. Mater. Sci.: Mater. Electron.* **2011**, *23*, 576.
- (112) Wen, B.; Liu, C.; Liu, Y. *Inorg. Chem.* **2005**, *44*, 6503.
- (113) Wang, W.; Lin, H.; Li, J.; Wang, N. *J. Am. Ceram. Soc.* **2008**, *91*, 628.
- (114) Feng, X.; Shankar, K.; Varghese, O. K.; Paulose, M.; Latempa, T. J.; Grimes, C. A. *Nano Lett.* **2008**, *8*, 3781.
- (115) Oh, J.-K.; Lee, J.-K.; Kim, H.-S.; Han, S.-B.; Park, K.-W. *Chem. Mater.* **2010**, *22*, 1114.
- (116) Wang, C.; Zhang, X.; Shao, C.; Zhang, Y.; Yang, J.; Sun, P.; Liu, X.; Liu, H.; Liu, Y.; Xie, T.; Wang, D. *J. Colloid Interface Sci.* **2011**, *363*, 157.
- (117) Lin, Y.; Skaff, H.; Emrick, T.; Dinsmore, A. D.; Russell, T. P. *Science* **2003**, *299*, 226.
- (118) Feng, Y.; Cho, I. S.; Rao, P. M.; Cai, L.; Zheng, X. *Nano Lett.* **2013**, *13*, 855.
- (119) Shi, J.; Hara, Y.; Sun, C.; Anderson, M. A.; Wang, X. *Nano Lett.* **2011**, *11*, 3413.
- (120) Liu, C.; Tang, J.; Chen, H. M.; Liu, B.; Yang, P. *Nano Lett.* **2013**, *13*, 2989.
- (121) Hwang, Y. J.; Boukai, A.; Yang, P. *Nano Lett.* **2009**, *9*, 410.
- (122) Carbone, L.; Cozzoli, P. D. *Nano Today* **2010**, *5*, 449.
- (123) Buonsanti, R.; Grillo, V.; Carlino, E.; Giannini, C.; Curri, M. L.; Innocenti, C.; Sangregorio, C.; Achterhold, K.; Parak, F. G.; Agostiano, A.; Cozzoli, P. D. *J. Am. Chem. Soc.* **2006**, *128*, 16953.
- (124) Buonsanti, R.; Grillo, V.; Carlino, E.; Giannini, C.; Gozzo, F.; Garcia-Hernandez, M.; Garcia, M. A.; Cingolani, R.; Cozzoli, P. D. *J. Am. Chem. Soc.* **2010**, *132*, 2437.
- (125) Buonsanti, R.; Snoeck, E.; Giannini, C.; Gozzo, F.; Garcia-Hernandez, M.; Angel Garcia, M.; Cingolani, R.; Cozzoli, P. D. *Phys. Chem. Chem. Phys.* **2009**, *11*, 3680.
- (126) Casavola, M.; Grillo, V.; Carlino, E.; Giannini, C.; Gozzo, F.; Pinel, E. F.; Garcia, M. A.; Manna, L.; Cingolani, R.; Cozzoli, P. D. *Nano Lett.* **2007**, *7*, 1386.
- (127) Limmer, S. J.; Cao, G. *Adv. Mater.* **2003**, *15*, 427.
- (128) Brinker, C. J.; Scherer, G. W. *Sol-gel science, the physics and chemistry of sol-gel processing*; Academic Press: Boston, 1990.
- (129) Chemseddine, A.; Moritz, T. *Eur. J. Inorg. Chem.* **1999**, *1999*, 235.
- (130) Bessekhoud, Y.; Robert, D.; Weber, J. V. *J. Photochem. Photobiol., A* **2003**, *157*, 47.
- (131) Sugimoto, T.; Zhou, X.; Muramatsu, A. *J. Colloid Interface Sci.* **2003**, *259*, 43.

- (132) Manorama, S. V.; Madhusudan Reddy, K.; Gopal Reddy, C. V.; Narayanan, S.; Rajesh Raja, P.; Chatterji, P. R. *J. Phys. Chem. Solids* **2002**, *63*, 135.
- (133) Sui, R.; Rizkalla, A. S.; Charpentier, P. A. *J. Phys. Chem. B* **2006**, *110*, 16212.
- (134) Wei, Q.; Hirota, K.; Tajima, K.; Hashimoto, K. *Chem. Mater.* **2006**, *18*, 5080.
- (135) Adachi, M.; Murata, Y.; Takao, J.; Jiu, J.; Sakamoto, M.; Wang, F. *J. Am. Chem. Soc.* **2004**, *126*, 14943.
- (136) Liu, Z.; Hu, Z.; Liang, J.; Li, S.; Yang, Y.; Peng, S.; Qian, Y. *Langmuir* **2004**, *20*, 214.
- (137) Peng, X.; Manna, L.; Yang, W.; Wickham, J.; Scher, E.; Kadavanich, A.; Alivisatos, A. P. *Nature* **2000**, *404*, 59.
- (138) Sun, Y.; Xia, Y. *Science* **2002**, *298*, 2176.
- (139) Manna, L.; Scher, E. C.; Alivisatos, A. P. *J. Am. Chem. Soc.* **2000**, *122*, 12700.
- (140) Manna, L.; Scher, E. C.; Li, L. S.; Alivisatos, A. P. *J. Am. Chem. Soc.* **2002**, *124*, 7136.
- (141) Yang, C.-S.; Awschalom, D. D.; Stucky, G. D. *Chem. Mater.* **2002**, *14*, 1277.
- (142) Buonsanti, R.; Grillo, V.; Carlino, E.; Giannini, C.; Kipp, T.; Cingolani, R.; Cozzoli, P. D. *J. Am. Chem. Soc.* **2008**, *130*, 11223.
- (143) Zhang, H.; Banfield, J. F. *J. Mater. Chem.* **1998**, *8*, 2073.
- (144) Zhang, H.; Gilbert, B.; Huang, F.; Banfield, J. F. *Nature* **2003**, *424*, 1025.
- (145) Finnegan, M. P.; Zhang, H.; Banfield, J. F. *J. Phys. Chem. C* **2007**, *111*, 1962.
- (146) Barnard, A. S.; Curtiss, L. A. *Nano Lett.* **2005**, *5*, 1261.
- (147) Barnard, A. S.; Zapol, P. *J. Phys. Chem. B* **2004**, *108*, 18435.
- (148) Koo, B.; Park, J.; Kim, Y.; Choi, S. H.; Sung, Y. E.; Hyeon, T. *J. Phys. Chem. B* **2006**, *110*, 24318.
- (149) Trentler, T. J.; Denler, T. E.; Bertone, J. F.; Agrawal, A.; Colvin, V. L. *J. Am. Chem. Soc.* **1999**, *121*, 1613.
- (150) Garvie, R. C. *J. Phys. Chem.* **1978**, *82*, 218.
- (151) Garvie, R. C. *J. Phys. Chem.* **1965**, *69*, 1238.
- (152) Buonsanti, R.; Carlino, E.; Giannini, C.; Altamura, D.; De Marco, L.; Giannuzzi, R.; Manca, M.; Gigli, G.; Cozzoli, P. D. *J. Am. Chem. Soc.* **2011**, *133*, 19216.
- (153) Simon, C. J.; Dupuy, D. E.; Mayo-Smith, W. W. *Radiographics* **2005**, *25* (Suppl 1), S69.
- (154) Jia, X.; He, W.; Zhang, X.; Zhao, H.; Li, Z.; Feng, Y. *Nanotechnology* **2007**, *18*, 075602.
- (155) Gedye, R.; Smith, F.; Westaway, K.; Ali, H.; Baldisera, L.; Laberge, L.; Rousell, J. *Tetrahedron Lett.* **1986**, *27*, 279.
- (156) Chen, Z.; Li, S.; Yan, Y. *Chem. Mater.* **2005**, *17*, 2262.
- (157) Cundy, C. S.; Cox, P. A. *Chem. Rev.* **2003**, *103*, 663.
- (158) Motuzas, J.; Julbe, A.; Noble, R. D.; Guizard, C.; Beresnevicius, Z. J.; Cot, D. *Microporous Mesoporous Mater.* **2005**, *80*, 73.
- (159) Baghbanzadeh, M.; Carbone, L.; Cozzoli, P. D.; Kappe, C. O. *Angew. Chem., Int. Ed. Engl.* **2011**, *50*, 11312.
- (160) Park, J.; Joo, J.; Kwon, S. G.; Jang, Y.; Hyeon, T. *Angew. Chem., Int. Ed. Engl.* **2007**, *46*, 4630.
- (161) Kwon, S. G.; Hyeon, T. *Acc. Chem. Res.* **2008**, *41*, 1696.
- (162) Bilecka, I.; Niederberger, M. *Nanoscale* **2010**, *2*, 1358.
- (163) Gressel-Michel, E.; Chaumont, D.; Stuerga, D. *J. Colloid Interface Sci.* **2005**, *285*, 674.
- (164) Wu, X.; Jiang, Q.-Z.; Ma, Z.-F.; Fu, M.; Shangguan, W.-F. *Solid State Commun.* **2005**, *136*, 513.
- (165) Ma, G.; Zhao, X.; Zhu, J. *Int. J. Mod. Phys. B* **2005**, *19*, 2763.
- (166) Yamamoto, T.; Wada, Y.; Yin, H.; Sakata, T.; Mori, H.; Yanagida, S. *Chem. Lett.* **2002**, 964.
- (167) Szabó, D. V.; Vollath, D.; Arnold, W. *Ceram. Trans.* **2001**, *111*, 217.
- (168) Yang, M.; Ding, B.; Lee, S.; Lee, J.-K. *J. Phys. Chem. C* **2011**, *115*, 14534.
- (169) Lin, K.-L.; Mai, F.-D.; Chan, Y.-C.; Chung, J.-C.; Lin, K.-M.; Yu, C.-C.; Liao, M.-Y.; Li, F.-Y. *J. Chin. Chem. Soc.* **2012**, *59*, 603.
- (170) Chung, C.-C.; Chung, T.-W.; Yang, T. C. K. *Ind. Eng. Chem. Res.* **2008**, *47*, 2301.
- (171) Chang, M.; Lin, C. H.; Deka, J. R.; Chang, F. C.; Chung, C. C. *J. Phys. D: Appl. Phys.* **2009**, *42*, 145105.
- (172) Suslick, K. S.; Hammerton, D. A.; Cline, R. E. *J. Am. Chem. Soc.* **1986**, *108*, 5641.
- (173) Flint, E. B.; Suslick, K. S. *Science* **1991**, *253*, 1397.
- (174) Zhu, Y.; Li, H.; Koltypin, Y.; Hacoheh, Y. R.; Gedanken, A. *Chem. Commun.* **2001**, 2616.
- (175) Jokanović, V.; Spasić, A. M.; Uskoković, D. *J. Colloid Interface Sci.* **2004**, *278*, 342.
- (176) Yun, C.; Chah, S.; Kang, S.; Yi, J. *Korean J. Chem. Eng.* **2004**, *21*, 1062.
- (177) C. Yu, J.; Zhang, L.; Yu, J. *New J. Chem.* **2002**, *26*, 416.
- (178) Suslick, K. S.; Choe, S.-B.; Cichowlas, A. A.; Grinstaff, M. W. *Nature* **1991**, *353*, 414.
- (179) Lei, B.-X.; Liao, J.-Y.; Zhang, R.; Wang, J.; Su, C.-Y.; Kuang, D.-B. *J. Phys. Chem. C* **2010**, *114*, 15228.
- (180) Mohapatra, S. K.; Misra, M.; Mahajan, V. K.; Raja, K. S. *J. Catal.* **2007**, *246*, 362.
- (181) Xu, C.; Zhan, Y.; Hong, K.; Wang, G. *Solid State Commun.* **2003**, *126*, 545.
- (182) Wang, G.; Li, G. *Eur. Phys. J. D* **2003**, *24*, 355.
- (183) Cho, I. S.; Lee, C. H.; Feng, Y.; Logar, M.; Rao, P. M.; Cai, L.; Kim, D. R.; Sinclair, R.; Zheng, X. *Nat. Commun.* **2013**, *4*, 1723.
- (184) Li, D.; Xia, Y. N. *Adv. Mater.* **2004**, *16*, 1151.
- (185) Huang, Z.-M.; Zhang, Y. Z.; Kotaki, M.; Ramakrishna, S. *Compos. Sci. Technol.* **2003**, *63*, 2223.
- (186) Subbiah, T.; Bhat, G. S.; Tock, R. W.; Parameswaran, S.; Ramkumar, S. S. *J. Appl. Polym. Sci.* **2005**, *96*, 557.
- (187) Li, D.; Xia, Y. *Nano Lett.* **2003**, *3*, 555.
- (188) Fu, Z.-W.; Ma, J.; Qin, Q.-Z. *Solid State Ionics* **2005**, *176*, 1635.
- (189) Dai, H.; Gong, J.; Kim, H.; Lee, D. *Nanotechnology* **2002**, *13*, 674.
- (190) Li, D.; McCann, J. T.; Xia, Y.; Marquez, M. *J. Am. Ceram. Soc.* **2006**, *89*, 1861.
- (191) Onozuka, K.; Ding, B.; Tsuge, Y.; Naka, T.; Yamazaki, M.; Sugi, S.; Ohno, S.; Yoshikawa, M.; Shiratori, S. *Nanotechnology* **2006**, *17*, 1026.
- (192) Juengsuwattananon, K.; Rujitanaroj, P. O.; Supaphol, P.; Pimpha, N.; Matsuzawa, S. *Mater. Sci. Forum* **2008**, *569*, 25.
- (193) Tan, S. H.; Inai, R.; Kotaki, M.; Ramakrishna, S. *Polymer* **2005**, *46*, 6128.
- (194) Khil, M. S.; Bhattacharai, S. R.; Kim, H. Y.; Kim, S. Z.; Lee, K. H. *J. Biomed. Mater. Res., Part B* **2005**, *72*, 117.
- (195) Duan, H. G.; Xie, E. Q.; Zhao, J. G.; Jia, C. W. *Mater. Sci. Technol.* **2008**, *24*, 241.
- (196) Yu, J.; Chen, Y.; Glushenkov, A. M. *Cryst. Growth Des.* **2009**, *9*, 1240.
- (197) Wu, J.-M.; Wu, W.-T.; Shih, H. C. *J. Electrochem. Soc.* **2005**, *152*, G613.
- (198) Wu, J.-J.; Yu, C.-C. *J. Phys. Chem. B* **2004**, *108*, 3377.
- (199) Chen, C. A.; Chen, Y. M.; Korotcov, A.; Huang, Y. S.; Tsai, D. S.; Tiong, K. K. *Nanotechnology* **2008**, *19*, 075611.
- (200) Park, Y.-S.; Lee, J.-S. *Bull. Korean Chem. Soc.* **2011**, *32*, 3571.
- (201) George, S. M. *Chem. Rev.* **2010**, *110*, 111.
- (202) Hitosugi, T.; Ueda, A.; Furubayashi, Y.; Hirose, Y.; Konuma, S.; Shimada, T.; Hasegawa, T. *Jpn. J. Appl. Phys.* **2007**, *46*, L86.
- (203) Doeswijk, L. M.; de Moor, H. H. C.; Blank, D. H. A.; Rogalla, H. *Appl. Phys. A: Mater. Sci. Process.* **1999**, *69*, S409.
- (204) Paily, R.; DasGupta, A.; DasGupta, N.; Bhattacharya, P.; Misra, P.; Ganguli, T.; Kukreja, L. M.; Balamurugan, A. K.; Rajagopalan, S.; Tyagi, A. K. *Appl. Surf. Sci.* **2002**, *187*, 297.
- (205) Moret, M. P.; Zallen, R.; Vijay, D. P.; Desu, S. B. *Thin Solid Films* **2000**, *366*, 8.
- (206) Noh, J. H.; Park, J. H.; Han, H. S.; Kim, D. H.; Han, B. S.; Lee, S.; Kim, J. Y.; Jung, H. S.; Hong, K. S. *J. Phys. Chem. C* **2012**, *116*, 8102.
- (207) Sauvage, F.; Di Fonzo, F.; Li Bassi, A.; Casari, C. S.; Russo, V.; Divitini, G.; Ducati, C.; Bottani, C. E.; Comte, P.; Graetzel, M. *Nano Lett.* **2010**, *10*, 2562.

- (208) Li, Y.; Sasaki, T.; Shimizu, Y.; Koshizaki, N. *J. Am. Chem. Soc.* **2008**, *130*, 14755.
- (209) Li, Y.; Fang, X.; Koshizaki, N.; Sasaki, T.; Li, L.; Gao, S.; Shimizu, Y.; Bando, Y.; Golberg, D. *Adv. Funct. Mater.* **2009**, *19*, 2467.
- (210) Sauthier, G.; György, E.; Figueras, A.; Sánchez, R. S.; Hernando, J. *J. Phys. Chem. C* **2012**, *116*, 14534.
- (211) Qiu, J.; Yu, W.; Gao, X.; Li, X. *Nanotechnology* **2006**, *17*, 4695.
- (212) Qiu, J.; Yu, W.; Gao, X.; Li, X. *Nanotechnology* **2007**, *18*, 295604.
- (213) Venkataraman, N. S.; Matsui, K.; Kawanami, H.; Ikushima, Y. *Green Chem.* **2007**, *9*, 18.
- (214) Bae, C.; Yoon, Y.; Yoo, H.; Han, D.; Cho, J.; Lee, B. H.; Sung, M. M.; Lee, M.; Kim, J.; Shin, H. *Chem. Mater.* **2009**, *21*, 2574.
- (215) Knez, M.; Nielsch, K.; Niinistö, L. *Adv. Mater.* **2007**, *19*, 3425.
- (216) Hultheen, J. C.; Martin, C. R. *J. Mater. Chem.* **1997**, *7*, 1075.
- (217) Limmer, S. J.; Seraji, S.; Forbess, M. J.; Wu, Y.; Chou, T. P.; Nguyen, C.; Cao, G. Z. *Adv. Mater.* **2001**, *13*, 1269.
- (218) Limmer, S. J.; Seraji, S.; Wu, Y.; Chou, T. P.; Nguyen, C.; Cao, G. Z. *Adv. Funct. Mater.* **2002**, *12*, 59.
- (219) Lakshmi, B. B.; Patrissi, C. J.; Martin, C. R. *Chem. Mater.* **1997**, *9*, 2544.
- (220) Singh, D. P.; Ali, N. *Sci. Adv. Mater.* **2010**, *2*, 295.
- (221) Zhang, M.; Bando, Y.; Wada, K. *J. Mater. Sci. Lett.* **2001**, *20*, 167.
- (222) Kang, T. S.; Smith, A. P.; Taylor, B. E.; Durstock, M. F. *Nano Lett.* **2009**, *9*, 601.
- (223) Miao, Z.; Xu, D.; Ouyang, J.; Guo, G.; Zhao, X.; Tang, Y. *Nano Lett.* **2002**, *2*, 717.
- (224) Lakshmi, B. B.; Dorhout, P. K.; Martin, C. R. *Chem. Mater.* **1997**, *9*, 857.
- (225) Attar, A. S.; Ghamsari, M. S.; Hajiesmaeilbaigi, F.; Mirdamadi, S.; Katagiri, K.; Koumoto, K. *Mater. Chem. Phys.* **2009**, *113*, 856.
- (226) Ren, X.; Gershon, T.; Iza, D. C.; Munoz-Rojas, D.; Musselman, K.; Macmanus-Driscoll, J. L. *Nanotechnology* **2009**, *20*, 365604.
- (227) Zhang, Y.; Dai, H. *Appl. Phys. Lett.* **2000**, *77*, 3015.
- (228) Bezryadin, A.; Lau, C. N.; Tinkham, M. *Nature* **2000**, *404*, 971.
- (229) Bezryadin, A.; Goldbart, P. M. *Adv. Mater.* **2010**, *22*, 1111.
- (230) Lee, Y.-H.; Yoo, J.-M.; Park, D.-h.; Kim, D. H.; Ju, B. K. *Appl. Phys. Lett.* **2005**, *86*, 033110.
- (231) Golden, T. D.; Shumsky, M. G.; Zhou, Y.; VanderWerf, R. A.; Van Leeuwen, R. A.; Switzer, J. A. *Chem. Mater.* **1996**, *8*, 2499.
- (232) He, P.; Liu, H.; Li, Z.; Liu, Y.; Xu, X.; Li, J. *Langmuir* **2004**, *20*, 10260.
- (233) Prasad, K. R.; Koga, K.; Miura, N. *Chem. Mater.* **2004**, *16*, 1845.
- (234) Ma, C.; Wang, Z. L. *Adv. Mater.* **2005**, *17*, 2635.
- (235) Xu, Q.; Zhang, L.; Zhu, J. *J. Phys. Chem. B* **2003**, *107*, 8294.
- (236) Zhang, X.; Yao, B.; Zhao, L.; Liang, C.; Zhang, L.; Mao, Y. *J. Electrochem. Soc.* **2001**, *148*, G398.
- (237) Hoyer, P. *Langmuir* **1996**, *12*, 1411.
- (238) Wang, D.; Liu, Y.; Wang, C.; Zhou, F.; Liu, W. *ACS Nano* **2009**, *3*, 1249.
- (239) Daothong, S.; Songmee, N.; Thongtem, S.; Singjai, P. *Scr. Mater.* **2007**, *57*, 567.
- (240) Huo, K.; Zhang, X.; Hu, L.; Sun, X.; Fu, J.; Chu, P. K. *Appl. Phys. Lett.* **2008**, *93*, 013105.
- (241) Huo, K.; Zhang, X.; Fu, J.; Qian, G.; Xin, Y.; Zhu, B.; Ni, H.; Chu, P. K. *J. Nanosci. Nanotechnol.* **2009**, *9*, 3341.
- (242) Behr, M.; Behr, O. *CHEMTECH* **1991**, *21*, 210.
- (243) Varghese, O. K.; Gong, D.; Paulose, M.; Ong, K. G.; Grimes, C. A. *Sens. Actuators, B* **2003**, *93*, 338.
- (244) Ruan, C.; Paulose, M.; Varghese, O. K.; Mor, G. K.; Grimes, C. A. *J. Phys. Chem. B* **2005**, *109*, 15754.
- (245) Kuang, D.; Brillet, J.; Chen, P.; Takata, M.; Uchida, S.; Miura, H.; Sumioka, K.; Zakeeruddin, S. M.; Gratzel, M. *ACS Nano* **2008**, *2*, 1113.
- (246) Banerjee, S.; Mohapatra, S. K.; Das, P. P.; Misra, M. *Chem. Mater.* **2008**, *20*, 6784.
- (247) Tao, R.-H.; Wu, J.-M.; Xue, H.-X.; Song, X.-M.; Pan, X.; Fang, X.-Q.; Fang, X.-D.; Dai, S.-Y. *J. Power Sources* **2010**, *195*, 2989.
- (248) Zhang, X.; Zhang, T.; Ng, J.; Sun, D. D. *Adv. Funct. Mater.* **2009**, *19*, 3731.
- (249) Harris, L. A. *J. Electrochem. Soc.* **1976**, *123*, 1010.
- (250) Harris, L. A. *J. Electrochem. Soc.* **1977**, *124*, 839.
- (251) Nakato, Y.; Akanuma, H.; Shimizu, J.-i.; Magari, Y. *J. Electroanal. Chem.* **1995**, *396*, 35.
- (252) Sugiura, T. *Electrochem. Solid-State Lett.* **1999**, *1*, 175.
- (253) Masuda, H.; Kanezawa, K.; Nakao, M.; Yokoo, A.; Tamamura, T.; Sugiura, T.; Minoura, H.; Nishio, K. *Adv. Mater.* **2003**, *15*, 159.
- (254) Sanjines, R.; Tang, H.; Berger, H.; Gozzo, F.; Margaritondo, G.; Levy, F. *J. Appl. Phys.* **1994**, *75*, 2945.
- (255) Gratzel, M. *Nature* **2001**, *414*, 338.
- (256) Hochbaum, A. I.; Yang, P. *Chem. Rev.* **2010**, *110*, 527.
- (257) Zhang, X.; Du, A. J.; Lee, P.; Sun, D. D.; Leckie, J. O. *J. Membr. Sci.* **2008**, *313*, 44.
- (258) Yun, H. J.; Lee, H.; Joo, J. B.; Kim, W.; Yi, J. *J. Phys. Chem. C* **2009**, *113*, 3050.
- (259) Hoffmann, M. R.; Martin, S. T.; Choi, W.; Bahnemann, D. W. *Chem. Rev.* **1995**, *95*, 69.
- (260) Mills, A.; Le Hunte, S. *J. Photochem. Photobiol., A* **1997**, *108*, 1.
- (261) Fujishima, A.; Rao, T. N.; Tryk, D. A. *J. Photochem. Photobiol., C* **2000**, *1*, 1.
- (262) Serpone, N.; Lawless, D.; Khairutdinov, R. *J. Phys. Chem.* **1995**, *99*, 16646.
- (263) Iacomino, A.; Cantele, G.; Trani, F.; Ninno, D. *J. Phys. Chem. C* **2010**, *114*, 12389.
- (264) Peng, H. W.; Li, J. B. *J. Phys. Chem. C* **2008**, *112*, 20241.
- (265) Tafen, D.; Lewis, J. P. *Phys. Rev. B* **2009**, *80*, 014104.
- (266) Xu, M.; Da, P.; Wu, H.; Zhao, D.; Zheng, G. *Nano Lett.* **2012**, *12*, 1503.
- (267) Dong, F.; Zhao, W.; Wu, Z. *Nanotechnology* **2008**, *19*, 365607.
- (268) Yu, J.; Xiang, Q.; Zhou, M. *Appl. Catal., B* **2009**, *90*, 595.
- (269) Hoang, S.; Berglund, S. P.; Hahn, N. T.; Bard, A. J.; Mullins, C. B. *J. Am. Chem. Soc.* **2012**, *134*, 3659.
- (270) Wang, J.; Tafen, D. N.; Lewis, J. P.; Hong, Z. L.; Manivannan, A.; Zhi, M. J.; Li, M.; Wu, N. Q. *J. Am. Chem. Soc.* **2009**, *131*, 12290.
- (271) Sakhthivel, S.; Janczarek, M.; Kisch, H. *J. Phys. Chem. B* **2004**, *108*, 19384.
- (272) Gai, Y. Q.; Li, J. B.; Li, S. S.; Xia, J. B.; Wei, S. H. *Phys. Rev. Lett.* **2009**, *102*, 036402.
- (273) Di Valentin, C.; Pacchioni, G.; Selloni, A. *Chem. Mater.* **2005**, *17*, 6656.
- (274) Umabayashi, T.; Yamaki, T.; Itoh, H.; Asai, K. *Appl. Phys. Lett.* **2002**, *81*, 454.
- (275) Zhu, W.; Qiu, X.; Iancu, V.; Chen, X. Q.; Pan, H.; Wang, W.; Dimitrijevic, N. M.; Rajh, T.; Meyer, H. M., 3rd; Paranthaman, M. P.; Stocks, G. M.; Weitering, H. H.; Gu, B.; Eres, G.; Zhang, Z. *Phys. Rev. Lett.* **2009**, *103*, 226401.
- (276) Umabayashi, T.; Yamaki, T.; Itoh, H.; Asai, K. *J. Phys. Chem. Solids* **2002**, *63*, 1909.
- (277) Liu, B.; Chen, H. M.; Liu, C.; Andrews, S. C.; Hahn, C.; Yang, P. D. *J. Am. Chem. Soc.* **2013**, *135*, 9995.
- (278) Wang, G. M.; Wang, H. Y.; Ling, Y. C.; Tang, Y. C.; Yang, X. Y.; Fitzmorris, R. C.; Wang, C. C.; Zhang, J. Z.; Li, Y. *Nano Lett.* **2011**, *11*, 3026.
- (279) Cheng, C.; Fan, H. J. *Nano Today* **2012**, *7*, 327.
- (280) Takabayashi, S.; Nakamura, R.; Nakato, Y. *J. Photochem. Photobiol., A* **2004**, *166*, 107.
- (281) Nozik, A. J. *Appl. Phys. Lett.* **1976**, *29*, 150.
- (282) Hensel, J.; Wang, G.; Li, Y.; Zhang, J. Z. *Nano Lett.* **2010**, *10*, 478.
- (283) An, W. J.; Wang, W. N.; Ramalingam, B.; Mukherjee, S.; Daubayev, B.; Gangopadhyay, S.; Biswas, P. *Langmuir* **2012**, *28*, 7528.
- (284) Smith, W.; Wolcott, A.; Fitzmorris, R. C.; Zhang, J. Z.; Zhao, Y. *J. Mater. Chem.* **2011**, *21*, 10792.
- (285) Ng, J.; Xu, S.; Zhang, X.; Yang, H. Y.; Sun, D. D. *Adv. Funct. Mater.* **2010**, *20*, 4287.

- (286) Liu, J.; Bai, H.; Wang, Y.; Liu, Z.; Zhang, X.; Sun, D. D. *Adv. Funct. Mater.* **2010**, *20*, 4175.
- (287) Pu, Y. C.; Wang, G.; Chang, K. D.; Ling, Y.; Lin, Y. K.; Fitzmorris, B. C.; Liu, C. M.; Lu, X.; Tong, Y.; Zhang, J. Z.; Hsu, Y. J.; Li, Y. *Nano Lett.* **2013**, *13*, 3817.
- (288) Dinh, C. T.; Nguyen, T. D.; Kleitz, F.; Do, T. O. *ACS Appl. Mater. Interfaces* **2011**, *3*, 2228.
- (289) Yang, D.; Yang, N.; Ge, J. *CrystEngComm* **2013**, *15*, 7230.
- (290) Yang, D.; Liu, H.; Zheng, Z.; Yuan, Y.; Zhao, J. C.; Waclawik, E. R.; Ke, X.; Zhu, H. *J. Am. Chem. Soc.* **2009**, *131*, 17885.
- (291) Liu, H.; Zheng, Z.; Yang, D.; Ke, X.; Jaatinen, E.; Zhao, J.-C.; Zhu, H. Y. *ACS Nano* **2010**, *4*, 6219.
- (292) Liu, B.; Khare, A.; Aydil, E. S. *ACS Appl. Mater. Interfaces* **2011**, *3*, 4444.
- (293) O'Regan, B.; Grätzel, M. *Nature* **1991**, *353*, 737.
- (294) Oekermann, T.; Zhang, D.; Yoshida, T.; Minoura, H. *J. Phys. Chem. B* **2004**, *108*, 2227.
- (295) Villanueva-Cab, J.; Wang, H.; Oskam, G.; Peter, L. M. *J. Phys. Chem. Lett.* **2010**, *1*, 748.
- (296) Fisher, A. C.; Peter, L. M.; Ponomarev, E. A.; Walker, A. B.; Wijayantha, K. G. U. *J. Phys. Chem. B* **2000**, *104*, 949.
- (297) Nelson, J. *Phys. Rev. B* **1999**, *59*, 15374.
- (298) Kang, S. H.; Choi, S. H.; Kang, M. S.; Kim, J. Y.; Kim, H. S.; Hyeon, T.; Sung, Y. E. *Adv. Mater.* **2008**, *20*, 54.
- (299) Lee, B. H.; Song, M. Y.; Jang, S.-Y.; Jo, S. M.; Kwak, S.-Y.; Kim, D. Y. *J. Phys. Chem. C* **2009**, *113*, 21453.
- (300) Zhou, Z. J.; Fan, J. Q.; Wang, X.; Zhou, W. H.; Du, Z. L.; Wu, S. X. *ACS Appl. Mater. Interfaces* **2011**, *3*, 4349.
- (301) Yang, L.; Leung, W. W. *Adv. Mater.* **2011**, *23*, 4559.
- (302) Wang, Z.; Wang, H.; Liu, B.; Qiu, W.; Zhang, J.; Ran, S.; Huang, H.; Xu, J.; Han, H.; Chen, D.; Shen, G. *ACS Nano* **2011**, *5*, 8412.
- (303) Sun, P.; Zhang, X.; Liu, X.; Wang, L.; Wang, C.; Yang, J.; Liu, Y. *J. Mater. Chem.* **2012**, *22*, 6389.
- (304) Feng, X.; Zhu, K.; Frank, A. J.; Grimes, C. A.; Mallouk, T. E. *Angew. Chem., Int. Ed. Engl.* **2012**, *51*, 2727.
- (305) Wang, M.; Bai, J.; Le Formal, F.; Moon, S.-J.; Cevey-Ha, L.; Humphry-Baker, R.; Grätzel, C.; Zakeeruddin, S. M.; Grätzel, M. J. *Phys. Chem. C* **2012**, *116*, 3266.
- (306) Gong, D.; Grimes, C. A.; Varghese, O. K.; Hu, W.; Singh, R. S.; Chen, Z.; Dickey, E. C. *J. Mater. Res.* **2011**, *16*, 3331.
- (307) Lu, Y.; Choi, D.-j.; Nelson, J.; Yang, O. B.; Parkinson, B. A. *J. Electrochem. Soc.* **2006**, *153*, E131.
- (308) Kumar, A.; Madaria, A. R.; Zhou, C. *J. Phys. Chem. C* **2010**, *114*, 7787.
- (309) Kim, H. S.; Lee, J. W.; Yantara, N.; Boix, P. P.; Kulkarni, S. A.; Mhaisalkar, S.; Gratzel, M.; Park, N. G. *Nano Lett.* **2013**, *13*, 2412.
- (310) Lv, M.; Zheng, D.; Ye, M.; Sun, L.; Xiao, J.; Guo, W.; Lin, C. *Nanoscale* **2012**, *4*, 5872.
- (311) Lv, M.; Zheng, D.; Ye, M.; Xiao, J.; Guo, W.; Lai, Y.; Sun, L.; Lin, C.; Zuo, J. *Energy Environ. Sci.* **2013**, *6*, 1615.
- (312) Roh, D. K.; Chi, W. S.; Jeon, H.; Kim, S. J.; Kim, J. H. *Adv. Funct. Mater.* **2014**, *24*, 379.
- (313) Liao, J.-Y.; Lei, B.-X.; Chen, H.-Y.; Kuang, D.-B.; Su, C.-Y. *Energy Environ. Sci.* **2012**, *5*, 5750.
- (314) Kim, D. H.; Seong, W. M.; Park, I. J.; Yoo, E. S.; Shin, S. S.; Kim, J. S.; Jung, H. S.; Lee, S.; Hong, K. S. *Nanoscale* **2013**, *5*, 11725.
- (315) De Marco, L.; Manca, M.; Buonsanti, R.; Giannuzzi, R.; Malara, F.; Pareo, P.; Martiradonna, L.; Giancaspro, N. M.; Cozzoli, P. D.; Gigli, G. *J. Mater. Chem.* **2011**, *21*, 13371.
- (316) Agosta, R.; Giannuzzi, R.; De Marco, L.; Manca, M.; Belviso, M. R.; Cozzoli, P. D.; Gigli, G. *J. Phys. Chem. C* **2013**, *117*, 2574.
- (317) De Marco, L.; Manca, M.; Giannuzzi, R.; Belviso, M. R.; Cozzoli, P. D.; Gigli, G. *Energy Environ. Sci.* **2013**, *6*, 1791.
- (318) Dong, Y.; Pan, K.; Tian, G.; Zhou, W.; Pan, Q.; Xie, T.; Wang, D.; Fu, H. *Dalton Trans.* **2011**, *40*, 3808.
- (319) Pan, K.; Dong, Y.; Tian, C.; Zhou, W.; Tian, G.; Zhao, B.; Fu, H. *Electrochim. Acta* **2009**, *54*, 7350.
- (320) Guo, W.; Xu, C.; Wang, X.; Wang, S.; Pan, C.; Lin, C.; Wang, Z. L. *J. Am. Chem. Soc.* **2012**, *134*, 4437.
- (321) Rochford, C.; Li, Z.-Z.; Baca, J.; Liu, J.; Li, J.; Wu, J. *Appl. Phys. Lett.* **2010**, *97*, 043102.
- (322) Tan, B.; Wu, Y. *J. Phys. Chem. B* **2006**, *110*, 15932.
- (323) Xu, C.; Wu, J.; Desai, U. V.; Gao, D. *Nano Lett.* **2012**, *12*, 2420.
- (324) Xu, C.; Wu, J.; Desai, U. V.; Gao, D. *J. Am. Chem. Soc.* **2011**, *133*, 8122.
- (325) Yang, L.; Leung, W. W. *Adv. Mater.* **2013**, *25*, 1792.
- (326) Kim, J. Y.; Lee, K.; Coates, N. E.; Moses, D.; Nguyen, T. Q.; Dante, M.; Heeger, A. J. *Science* **2007**, *317*, 222.
- (327) Peet, J.; Kim, J. Y.; Coates, N. E.; Ma, W. L.; Moses, D.; Heeger, A. J.; Bazan, G. C. *Nat. Mater.* **2007**, *6*, 497.
- (328) Chen, H.-Y.; Hou, J.; Zhang, S.; Liang, Y.; Yang, G.; Yang, Y.; Yu, L.; Wu, Y.; Li, G. *Nat. Photonics* **2009**, *3*, 649.
- (329) Wu, W.-Q.; Liao, J.-Y.; Chen, H.-Y.; Yu, X.-Y.; Su, C.-Y.; Kuang, D.-B. *J. Mater. Chem.* **2012**, *22*, 18057.
- (330) Li, G.; Zhu, R.; Yang, Y. *Nat. Photonics* **2012**, *6*, 153.
- (331) Weickert, J.; Dunbar, R. B.; Hesse, H. C.; Wiedemann, W.; Schmidt-Mende, L. *Adv. Mater.* **2011**, *23*, 1810.
- (332) Snaith, H. J.; Arias, A. C.; Morteani, A. C.; Silva, C.; Friend, R. H. *Nano Lett.* **2002**, *2*, 1353.
- (333) Huynh, W. U.; Dittmer, J. J.; Teclamarium, N.; Milliron, D. J.; Alivisatos, A. P.; Barnham, K. W. *J. Phys. Rev. B* **2003**, *67*, 115326.
- (334) Lee, K.; Kim, J. Y.; Park, S. H.; Kim, S. H.; Cho, S.; Heeger, A. J. *Adv. Mater.* **2007**, *19*, 2445.
- (335) Zeng, T.-W.; Lin, Y.-Y.; Lo, H.-H.; Chen, C.-W.; Chen, C.-H.; Liou, S.-C.; Huang, H.-Y.; Su, W.-F. *Nanotechnology* **2006**, *17*, 5387.
- (336) Kuo, C. Y.; Tang, W. C.; Gau, C.; Guo, T. F.; Jeng, D. Z. *Appl. Phys. Lett.* **2008**, *93*, 033307.
- (337) Williams, S. S.; Hampton, M. J.; Gowrishankar, V.; Ding, I. K.; Templeton, J. L.; Samulski, E. T.; DeSimone, J. M.; McGehee, M. D. *Chem. Mater.* **2008**, *20*, 5229.
- (338) Lin, Y. Y.; Chu, T. H.; Li, S. S.; Chuang, C. H.; Chang, C. H.; Su, W. F.; Chang, C. P.; Chu, M. W.; Chen, C. W. *J. Am. Chem. Soc.* **2009**, *131*, 3644.
- (339) Lu, Q.; Lu, Z.; Lu, Y.; Lv, L.; Ning, Y.; Yu, H.; Hou, Y.; Yin, Y. *Nano Lett.* **2013**, *13*, 5698.
- (340) Loiudice, A.; Rizzo, A.; De Marco, L.; Belviso, M. R.; Caputo, G.; Cozzoli, P. D.; Gigli, G. *Phys. Chem. Chem. Phys.* **2012**, *14*, 3987.
- (341) Nozik, A. J.; Beard, M. C.; Luther, J. M.; Law, M.; Ellingson, R. J.; Johnson, J. C. *Chem. Rev.* **2010**, *110*, 6873.
- (342) Nozik, A. J. *Phys. E (Amsterdam, Neth.)* **2002**, *14*, 115.
- (343) Bang, J. H.; Kamat, P. V. *Adv. Funct. Mater.* **2010**, *20*, 1970.
- (344) Li, M.; Liu, Y.; Wang, H.; Shen, H.; Zhao, W.; Huang, H.; Liang, C. *J. Appl. Phys.* **2010**, *108*, 094304.
- (345) Wang, H.; Bai, Y.; Zhang, H.; Zhang, Z.; Li, J.; Guo, L. *J. Phys. Chem. C* **2010**, *114*, 16451.
- (346) Medina-Gonzalez, Y.; Xu, W. Z.; Chen, B.; Farhanghi, N.; Charpentier, P. A. *Nanotechnology* **2011**, *22*, 06S603.
- (347) Lee, J.-C.; Sung, Y.-M.; Kim, T. G.; Choi, H.-J. *Appl. Phys. Lett.* **2007**, *91*, 113104.
- (348) Lee, J.-C.; Kim, T. G.; Lee, W.; Han, S.-H.; Sung, Y.-M. *Cryst. Growth Des.* **2009**, *9*, 4519.
- (349) Lan, X.; Bai, J.; Masala, S.; Thon, S. M.; Ren, Y.; Kramer, I. J.; Hoogland, S.; Simchi, A.; Koleilat, G. I.; Paz-Soldan, D.; Ning, Z.; Labelle, A. J.; Kim, J. Y.; Jabbour, G.; Sargent, E. H. *Adv. Mater.* **2013**, *25*, 1769.
- (350) Loiudice, A.; Rizzo, A.; Grancini, G.; Biasiucci, M.; Belviso, M. R.; Corricelli, M.; Curri, M. L.; Striccoli, M.; Agostiano, A.; Cozzoli, P. D.; Petrozza, A.; Lanzani, G.; Gigli, G. *Energy Environ. Sci.* **2013**, *6*, 1565.
- (351) Wang, Y.; Cao, G. *Adv. Mater.* **2008**, *20*, 2251.
- (352) Liu, R.; Duay, J.; Lee, S. B. *Chem. Commun.* **2011**, *47*, 1384.
- (353) Winter, M.; Brodd, R. J. *Chem. Rev.* **2004**, *104*, 4245.
- (354) Nam, K. T.; Kim, D.-W.; Yoo, P. J.; Chiang, C.-Y.; Meethong, N.; Hammond, P. T.; Chiang, Y.-M.; Belcher, A. M. *Science* **2006**, *312*, 885.

- (355) Armstrong, G.; Armstrong, A. R.; Bruce, P. G.; Reale, P.; Scrosati, B. *Adv. Mater.* **2006**, *18*, 2597.
- (356) Wu, F. X.; Wang, Z. X.; Li, X. H.; Guo, H. J. *J. Mater. Chem.* **2011**, *21*, 12675.
- (357) Dalton, A. S.; Belak, A. A.; Van der Ven, A. *Chem. Mater.* **2012**, *24*, 1568.
- (358) Armstrong, A. R.; Armstrong, G.; Canales, J.; Bruce, P. G. *Angew. Chem., Int. Ed. Engl.* **2004**, *43*, 2286.
- (359) Wang, D.; Choi, D.; Li, J.; Yang, Z.; Nie, Z.; Kou, R.; Hu, D.; Wang, C.; Saraf, L. V.; Zhang, J.; Aksay, I. A.; Liu, J. *ACS Nano* **2009**, *3*, 907.
- (360) Wang, W.; Tian, M.; Abdulagatov, A.; George, S. M.; Lee, Y. C.; Yang, R. *Nano Lett.* **2012**, *12*, 655.
- (361) Lu, X.; Yu, M.; Wang, G.; Zhai, T.; Xie, S.; Ling, Y.; Tong, Y.; Li, Y. *Adv. Mater.* **2013**, *25*, 267.
- (362) Fan, Z.; Yan, J.; Wei, T.; Zhi, L.; Ning, G.; Li, T.; Wei, F. *Adv. Funct. Mater.* **2011**, *21*, 2366.
- (363) Wu, Z. S.; Ren, W.; Wang, D. W.; Li, F.; Liu, B.; Cheng, H. M. *ACS Nano* **2010**, *4*, 5835.
- (364) Wang, Q.; Wen, Z. H.; Li, J. H. *Adv. Funct. Mater.* **2006**, *16*, 2141.
- (365) Xia, X.; Luo, J.; Zeng, Z.; Guan, C.; Zhang, Y.; Tu, J.; Zhang, H.; Fan, H. J. *Sci. Rep.* **2012**, *2*, 981.
- (366) Mortimer, R. J. *Annu. Rev. Mater. Res.* **2011**, *41*, 241.
- (367) Xia, X.; Chao, D.; Qi, X.; Xiong, Q.; Zhang, Y.; Tu, J.; Zhang, H.; Fan, H. J. *Nano Lett.* **2013**, *13*, 4562.
- (368) Vuong, N. M.; Kim, D.; Kim, H. J. *Mater. Chem. C* **2013**, *1*, 3399.
- (369) Chen, J. Z.; Ko, W. Y.; Yen, Y. C.; Chen, P. H.; Lin, K. J. *ACS Nano* **2012**, *6*, 6633.
- (370) Kolmakov, A.; Moskovits, M. *Annu. Rev. Mater. Res.* **2004**, *34*, 151.
- (371) Li, Z.; Zhang, H.; Zheng, W.; Wang, W.; Huang, H.; Wang, C.; MacDiarmid, A. G.; Wei, Y. *J. Am. Chem. Soc.* **2008**, *130*, 5036.
- (372) Francioso, L.; Taurino, A.; Forleo, A.; Siciliano, P. *Sens. Actuators, B* **2008**, *130*, 70.
- (373) Gong, J.; Li, Y.; Hu, Z.; Zhou, Z.; Deng, Y. *J. Phys. Chem. C* **2010**, *114*, 9970.
- (374) Kim, I. D.; Rothschild, A.; Lee, B. H.; Kim, D. Y.; Jo, S. M.; Tuller, H. L. *Nano Lett.* **2006**, *6*, 2009.
- (375) Caricato, A. P.; Buonsanti, R.; Catalano, M.; Cesaria, M.; Cozzoli, P. D.; Luches, A.; Manera, M. G.; Martino, M.; Taurino, A.; Rella, R. *Appl. Phys. A: Mater. Sci. Process.* **2011**, *104*, 963.
- (376) Tian, W. C.; Ho, Y. H.; Chen, C. H.; Kuo, C. Y. *Sensors* **2013**, *13*, 865.
- (377) Dai, L.; Sow, C. H.; Lim, C. T.; Cheong, W. C. D.; Tan, V. B. C. *Nano Lett.* **2009**, *9*, 576.